

# Pattern Formation in Membranes with Quenched Disorder

Dissertation  
zur Erlangung des  
mathematisch-naturwissenschaftlichen Doktorgrades  
“Doctor rerum naturalium”  
der Georg-August-Universität Göttingen

im Promotionsprogramm ProPhys  
der Georg-August University School of Science (GAUSS)

vorgelegt von  
**Sina Sadeghi**  
aus Ahwaz, Iran

Göttingen, 2014

## **Betreuungsausschuss**

Dr. Richard L. C. Vink  
Institute of Theoretical Physics,  
Georg-August-Universität Göttingen

Prof. Dr. Annette Zippelius  
Institute of Theoretical Physics,  
Georg-August-Universität Göttingen

## **Mitglieder der Prüfungskommission**

Referent: Dr. Richard L. C. Vink  
Institute of Theoretical Physics,  
Georg-August-Universität Göttingen

Korreferentin: Prof. Dr. Annette Zippelius  
Institute of Theoretical Physics,  
Georg-August-Universität Göttingen

## **Weitere Mitglieder der Prüfungskommission**

Prof. Dr. Marcus Müller  
Institute of Theoretical Physics,  
Georg-August-Universität Göttingen

Prof. Dr. Christian Eggeling  
Weatherall Institute of Molecular Medicine,  
University of Oxford

Prof. Dr. Reiner Kree  
Institute of Theoretical Physics,  
Georg-August-Universität Göttingen

Prof. Dr. Helmut Grubmüller  
Department of Theoretical and Computational Biophysics,  
Max Planck Institute for Biophysical Chemistry

Tag der mündlichen Prüfung:

# Preface

This cumulative dissertation contains the following peer-reviewed articles:

1. Sina Sadeghi and Richard L. C. Vink (2012), Main transition in the Pink membrane model: Finite-size scaling and the influence of surface roughness, *Physical Review E*, 85(6):061912. DOI: 10.1103/PhysRevE.85.061912.
2. Sina Sadeghi, Marcus Müller, and Richard L. C. Vink (2014), Raft Formation in Lipid Bilayers Coupled to Curvature, *Biophysical Journal*, 107(7):1591. DOI: 10.1016/j.bpj.2014.07.072.
3. Alf Honigmann, Sina Sadeghi, Jan Keller, Stefan W. Hell, Christian Eggeling, and Richard L. C. Vink (2014), A lipid bound actin meshwork organizes liquid phase separation in model membranes, *eLife*, 3:e01671. DOI: 10.7554/eLife.01671.
4. Sina Sadeghi and Richard L. C. Vink (2014), Membrane Sorting via the Extracellular Matrix, *Biochimica et Biophysica Acta (BBA) - Biomembranes*, 1848(2):527. DOI: 10.1016/j.bbamem.2014.10.035.

# Contents

<b>Preface</b>	<b>ii</b>
<b>Contents</b>	<b>iii</b>
<b>1 Introduction</b>	<b>1</b>
1.1 Cell Membrane	1
1.2 Lipid Rafts	4
1.3 Phase Separation in Model Lipid Membranes	6
1.4 Membrane-Cytoskeleton Coupling: Quenched Disorder	8
1.5 Curvature-induced Microemulsion	10
1.6 Outline	11
<b>2 Computer Simulations</b>	<b>13</b>
2.1 Models	13
2.1.1 Pink Model	14
2.1.2 Two-dimensional Membrane Model with Height Deformations: The Curvature-Composition Coupling	15
2.2 Monte Carlo Simulations of Phase Transitions	19
2.3 Order Parameter Distribution	19
2.4 Successive Umbrella Sampling	21
2.5 Histogram Reweighting	22
2.6 Finite-size Scaling	24
<b>3 Main transition in the Pink membrane model: Finite-size scaling and the influence of surface roughness</b>	<b>26</b>
3.1 Introduction	27
3.2 The Pink model	29
3.2.1 Coarse-graining parameters	30
3.2.2 Pink model Hamiltonian	33
3.3 Monte Carlo methods	33
3.4 Results	35
3.4.1 The “standard” Pink model revisited	35
3.4.2 Modified Pink model with fewer states	38
3.4.3 Pink model with quenched disorder	39
3.5 Conclusion	43

<b>4</b>	<b>Raft formation in lipid bilayers coupled to curvature</b>	<b>45</b>
4.1	Introduction . . . . .	46
4.2	Theoretical Background . . . . .	48
4.3	Simulation Model . . . . .	51
4.4	Simulation Method . . . . .	53
4.4.1	Monte Carlo moves . . . . .	53
4.4.2	Order parameter distribution . . . . .	54
4.4.3	Model parameters and units . . . . .	55
4.5	Results . . . . .	55
4.5.1	No curvature coupling: $\gamma = 0$ . . . . .	55
4.5.2	Fluid phase with curvature coupling . . . . .	56
4.5.3	Phase transitions . . . . .	59
4.6	Conclusions . . . . .	62
<b>5</b>	<b>A lipid bound actin meshwork organizes liquid phase separation in model membranes</b>	<b>64</b>
5.1	Introduction . . . . .	65
5.2	Experimental results . . . . .	67
5.2.1	Domain formation in membranes without actin . . . . .	67
5.2.2	Domain formation in membranes with actin . . . . .	70
5.2.3	The lateral diffusion of lipids is restricted by actin-organized domains . . . . .	71
5.2.4	Influence of the type of lipid-pinning site on domain structure . . . . .	74
5.3	Simulation results . . . . .	76
5.4	Discussion . . . . .	81
5.5	Materials and methods . . . . .	82
5.5.1	Preparation of Mica supported membranes . . . . .	82
5.5.2	Actin binding to supported membranes . . . . .	83
5.5.3	Simulation model . . . . .	83
5.5.4	Monte Carlo simulation procedure . . . . .	85
5.5.5	Temperature control of the membrane . . . . .	85
5.5.6	Microscopy . . . . .	85
5.5.7	Image analysis . . . . .	87
5.5.8	Scanning FCS and pair-correlation analysis . . . . .	87
5.6	Appendix: Supplementary Figures . . . . .	88
<b>6</b>	<b>Membrane sorting via the extracellular matrix</b>	<b>94</b>
6.1	Introduction . . . . .	95
6.2	Model and method . . . . .	96
6.3	Results . . . . .	97
6.3.1	Membrane “sandwiched” between a solid substrate and an actin network . . . . .	97
6.3.2	Pinning sites that induce local membrane curvature . . . . .	101
6.4	Discussion . . . . .	103
<b>7</b>	<b>Summary</b>	<b>105</b>
	<b>Bibliography</b>	<b>110</b>

# Chapter 1

## Introduction

Living organisms, composed of a large number of components that cooperate together, exhibit collective behaviour. This fascinating self-organized phenomenon, ubiquitous in nature, is emerged as a result of interaction between many individual constituents [see e.g., [Mitchell, 2009](#)]. In an interdisciplinary approach, biophysics has provided an impressive collection of knowledge about biological systems from different aspects based upon the underlying physical principles. Among those biological systems, cells and their structural organization have been intensely investigated, and their physical properties probed both experimentally and theoretically. All cells are surrounded by a membrane that provides a selective permeable barrier around the cell and plays diverse roles in cell behaviour. Most cell functionalities, in fact, take place at or are mediated by the cell membrane [[Alberts et al., 2008](#); [Phillips et al., 2012](#)]. In this case, the chemical composition of the cell membrane and the organization of the membrane constituents are of great importance in cellular processes. This chapter represents a brief overview on the cell membrane and its molecular structure that importantly regulates various functions of the biological cells.

### 1.1 Cell Membrane

All living matter is made of cells; *prokaryotes* (without cell nucleus) including *eubacteria* and *archaeobacteria* like *Escherchia cloi*, *eukaryotes* (with cell nucleus) from unicellular organism like yeast, to even more complicated multicellular organisms like fungi, plants, and animals [[Mouritsen, 2004](#); [Alberts et al., 2008](#); [Phillips et al., 2012](#)]. Cells as building blocks of living organisms, regardless of their varieties in shapes and tasks in different

organisms, share a number of common features. They all include DNA (the information-storing molecules), ribosome (molecular machinery manufacturing proteins), cytoplasm (thick fluidic environment interior of the cell, i.e., *cytosol*, containing organelles), and a membrane encapsulating all mentioned intercellular components [Alberts et al., 2008; Phillips et al., 2012]. The cell membrane (also called plasma membrane) is indeed an important part of the cell that defines the cell boundary and separates it from its surrounding environment. In addition to this primitive function, the plasma membrane is actively involved in many cellular processes such as transport, growth, neural function, immunological response, motility, signaling, and enzymatic activity [Mouritsen, 2004; Alberts et al., 2008; Phillips et al., 2012].

The main ingredients of plasma membranes are lipid molecules, so that about 50% of the membrane mass of most animal cells consists of lipids [Alberts et al., 2008]. Lipids are veritably crucial in construction of the plasma membrane. They are *amphiphilic* molecules, typically composed of a polar head group which is *hydrophilic* (water-loving), and one or two non-polar hydrocarbon chains, the *hydrophobic* (water-fearing) part. The most common lipids in the plasma membrane of *eukaryotic* cells are **phospholipids**, **sphingolipids**, and **cholesterol** (see Fig. 1.1) [Mouritsen, 2004; Alberts et al., 2008]. Phospholipids typically have two hydrocarbon chains that are linked through a *glycerol phosphate* as a backbone to a polar head group. The number of carbon atoms in the hydrocarbon chain determines its length. In the cell membrane, phospholipids are mainly unsaturated lipids in which a hydrocarbon chain has at least one *cis*-double bond. The latter bond induces a kink in the hydrocarbon chain which is fairly stable in a wide range of temperature. Rather than *glycerol*, sphingolipids are derivative of *sphingosine* which already has a long hydrocarbon chain. Sphingolipids are typically saturated lipids with only single carbon-carbon bonds in their hydrocarbon chains. The latter lipids have more conformational degrees of freedom so that lowering the temperature one achieves more order in their hydrocarbon chains, for example, in *all-trans* when the hydrocarbon chain is fully expanded. Cholesterol is remarkably different from other classes of lipids mentioned above. It has a ring steroid structure rather than hydrocarbon chains, and a simple *hydroxyl* head. This characterizes cholesterol as a bulky and stiff lipid with a small head group, which is nevertheless essential for the higher life in *eukaryotes* [Alberts et al., 2008; Phillips et al., 2012].

Plasma membranes spontaneously self-assemble in a form of lipid bilayers in an aqueous solution (Fig. 1.2). They are constructed in such a way that hydrocarbon chains of lipids point inward due to the hydrophobicity of chains, whereas hydrophilic heads are

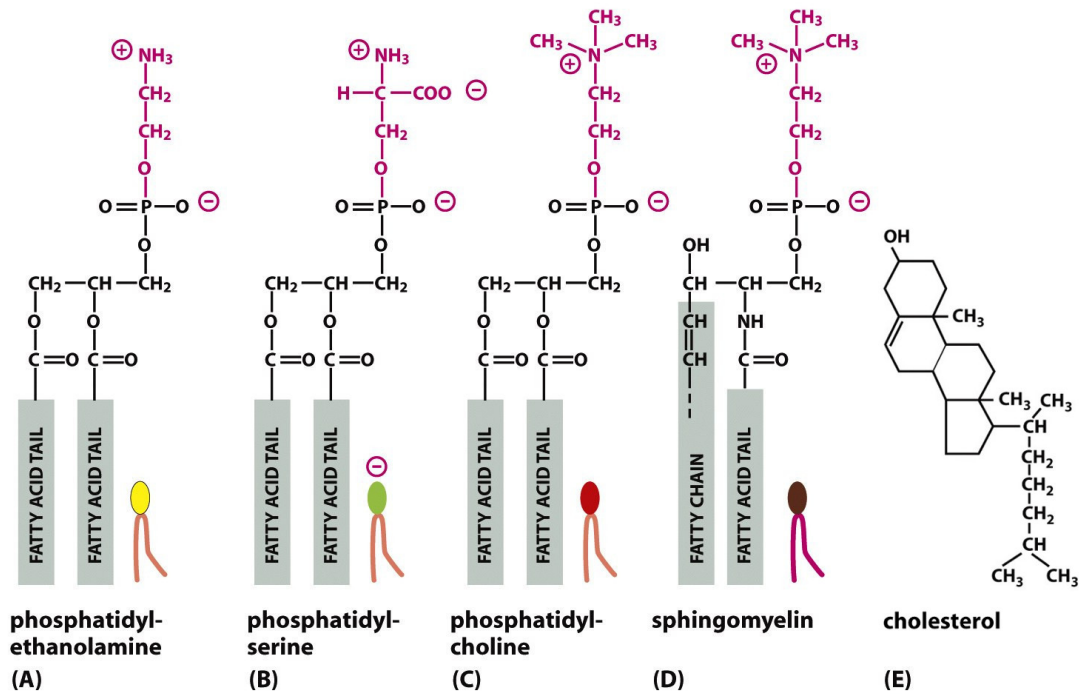


**Figure 1.1:** Molecular structure of different major lipid molecules present in mammalian plasma membranes. (A-C) Glycerophospholipids, typically unsaturated lipids, abundant in the inner leaflet (A-B), and outer leaflet (C) of cell bilayer membranes. (D) Sphingomyelin, a saturated lipid present in the outer leaflet. (E) Steroid ring structure of cholesterol. **Lipid rafts** are small domains rich in sphingolipids and cholesterol representing liquid-ordered phase floating in an ocean of unsaturated lipids, namely glycerophospholipids that exhibit liquid-disordered phase. (Adopted from [Alberts et al., 2008](#).)

exposing to polar molecules of the water. The thickness of the membrane depends on lipids chain length and is typically about 5 nm. Lipids diffuse rapidly in each monolayer with lateral diffusion constant  $D \approx 10^{-8} \text{ cm}^2/\text{s}$ , but the flip-flop between two leaflets is relatively rare due to the hydrophobic repulsion of hydrocarbon chains [[Alberts et al., 2008](#); [Phillips et al., 2012](#)]. The plasma membrane, therefore, is considered as a two-dimensional fluid sheet that encloses the cell volume. The membrane fluidity is crucial for proper functioning of the cell so that, for example, some proteins become inactive when membrane solidifies. Higher concentration of unsaturated lipids in the plasma membrane induces a disordered state in which the fluidity is higher, whereas membrane regions rich in cholesterol represent a ordered state with reduced fluidity. Plasma membranes like most biological materials are soft matter with substantial conformational complexity. The membrane softness implies mechanical flexibility that is manifested by thermal fluctuations and undulations. This property enables the cell to properly respond to



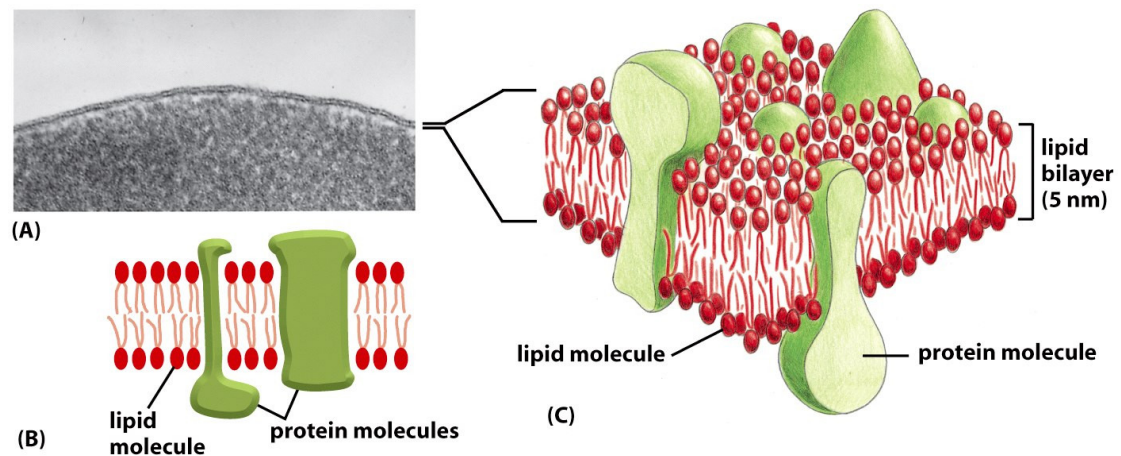


**Figure 1.2:** (A) An electron micrograph of the plasma membrane of human red blood cells [Daniel S. Friend]. (B) Side view depiction of the lipid bilayer membrane; some proteins span within the bilayer. (C) Fluid-mosaic model of the plasma membrane describes a two-dimensional fluid of rapidly diffusing lipids with integral proteins randomly distributed in the membrane. The thickness of the bilayer membrane is about 5 nm. (Courtesy of [Alberts et al., 2008](#).)

external conditions. It also serves to carry out certain functions like cell division, cell adhesion, and cell motility.

Proteins, ubiquitous in cells, are also present in plasma membranes, taking care of considerable varieties of biological activities. Integral proteins are largely involved in some specific functions. For example, transport proteins, spanned within the membrane, provide selective channels for transporting matter and information through the membrane into and out of the cell. In addition, peripheral proteins anchored to the membrane often have structural roles and may function in signaling pathway. Of course, presence of the proteins in the plasma membrane induces more complexity to be considered, yet detailed and systematic inclusion of them is not the aim of this thesis (although we do consider how proteins may affect lipid domains).

## 1.2 Lipid Rafts

The lateral organization of lipids and proteins in the biological membrane is an important feature in cellular functions [[Binder et al., 2003](#)]. In fact, the interaction of the cell and its environment is regulated via proteins and lipids organization in the plasma membrane. A prominent model for the plasma membrane is the **fluid mosaic** proposed by [Singer and Nicolson \[1972\]](#) that mainly retains the bilayer structure of the lipid membrane

from previous models (Fig. 1.2). It, furthermore, proposes that the proteins are floating at random positions in the membrane, and some proteins are even spanned within the bilayer membrane. Although this model modifies our understanding of the membrane structure from early models (for example, lipo-protein sandwich model in which proteins coated in a layer on the exterior part of the membrane [Danielli and Davson, 1935]), still lacks of precise knowledge about the distribution of lipids across the bilayer membrane. The fluidity of the plasma membrane still suggests a random distribution of lipids in the membrane. However, this has been challenged by widely accepted experimental evidence that characterizes a nontrivial lateral heterogeneity in the plasma membrane [Pike, 2009; Lingwood and Simons, 2010]. The latter is argued to be a vital issue for the living being [Brown and London, 1998]. More precisely, in the plasma membrane, lipids are clustered into domains composed of saturated lipids and cholesterol floating like rafts in an ocean of unsaturated lipids. These highly dynamic and small domains rich in sphingolipids and cholesterol are called **lipid rafts** [Edidin, 2003; Hancock, 2006]. Although lipid rafts were conceived to address particular biological problem [Simons and van Meer, 1988; van Meer and Simons, 1988], ever since they became a paramount in cell researches as fascinating entity in the plasma membrane. Lipid rafts are supposed to be thicker and more compact than the surrounding due to the higher order in tightly packed hydrocarbon chains of sphingolipids. They are also more stiff because of abundant of cholesterol in between the hydrocarbon chains.

Lipid rafts have not yet been visually observed *in vivo* and their existence is even under question by some [Munro, 2003; McMullen et al., 2004; Nichols, 2005]. Nevertheless, there exists compelling indirect evidence to support the lipid raft hypothesis, and their size is postulated to be in the range of 10 – 200 nm [Pike, 2009]. Single-particle tracking technique and fluorescence microscopy, for instance, are used to probe lateral diffusion of fluorescently labeled lipids in the membrane. Experimental results show a temporary confinement of diffusive lipids in some small regions that, after some transient time, appear in another confined zone. This is due to the reduced fluidity of cholesterol-rich domains in the membrane, i.e., lipid rafts [Lingwood and Simons, 2010].

Other experimental techniques, extensively applied to investigate the plasma membrane structure and lipid rafts, include atomic force microscopy (AFM) [Frederix et al., 2009], nuclear magnetic resonance (NMR) [Angelis et al., 2005], and stimulated emission depletion (STED) [Eggeling et al., 2009, 2013]. All these experiments have provided more insight into understanding the lateral heterogeneity of plasma membranes, as well as synthetic (model) membranes.

Lipid rafts are believed to support various aspects of biological functions including cell surface signaling, intracellular trafficking, cell surface adhesion, cell motility, endocytosis, cytokinesis, etc. These functions are predominantly carried out via specific proteins that prefer to partition into specific lipid domains, i.e., lipid rafts [Simons and Toomre, 2000]. In addition, some pathogens seem to enter mammalian cells via the ordered fluid state in the membrane, and certain diseases like prion disease, Alzheimer’s disease, and cancer might be associated with lipid rafts as well [Brown and London, 1998; Simons and Ehehalt, 2002].

### 1.3 Phase Separation in Model Lipid Membranes

The extremely complex composition and structure of plasma membranes makes their detailed investigations difficult. Model membranes, on the other hand, with a much reduced number of lipid species, provide an attractive alternative. In these “simplified” membranes, collective phenomena can be systematically studied in great detail [Lipowsky and Sackmann, 1995]. A prime example of collective behaviour are phase transitions, that are frequently observed in model membranes [London and Brown, 2000; Veatch and Keller, 2003]. One of those is the main phase transition, also called melting phase transition [Nagle, 1980]. The main phase transition generally occurs in a single-component membrane containing saturated lipids at a transition temperature  $T_m$ , where a pronounced peak is observed in the specific heat. This is a first-order phase transition between solid-ordered (So) and liquid-disordered (Ld) phases. The solid-ordered phase is characterized by crystallized lipids with highly ordered hydrocarbon chains, while the liquid-disordered state is distinguished by diffusing lipids with less ordered hydrocarbon chains [Mouritsen, 1991]. The presence of cholesterol in the phospholipid membrane brings about a new phase into the system, namely the liquid-ordered (Lo) phase [Ipsen et al., 1987]. In liquid-ordered phase, hydrocarbon chains are fairly ordered due to the presence of cholesterol in between them, yet lipid molecules are positionally disordered in the membrane; they still laterally diffuse. In multi-component model membranes, there exists the possibility of unmixing of the components, and the phase transition occurs in a wider range of thermodynamic variables rather than a single transition temperature [Mouritsen, 1991]. In such cases, the lipid-lipid interaction results in phases separation of lipids in different phases. For instance, a ternary mixture of saturated and unsaturated lipids, as well as cholesterol phase separates macroscopically into liquid-ordered and liquid-disordered phases depending on temperature and composition [Veatch and Keller,

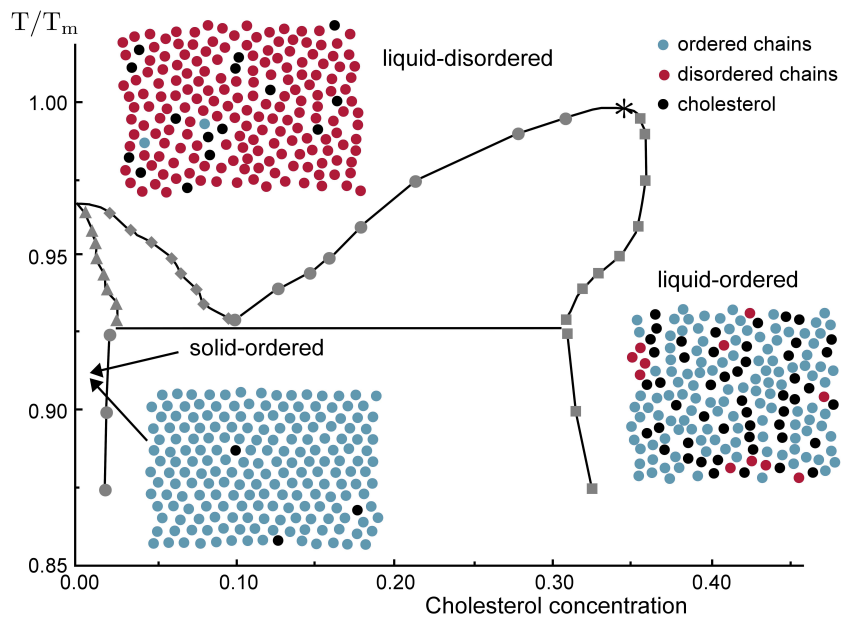


**Figure 1.3:** Schematic phase diagram of a bilayer membrane comprising a binary mixture of saturated phospholipids and cholesterol.  $T_m$  is the transition temperature of the pure bilayer membrane, and the critical point is marked by an asterisk. (Adopted from Mouritsen, 2011.)

2002]. The significance of the presence of cholesterol in phospholipid membranes is to introduce a critical point and hence a continuous phase transition. A schematic phase diagram of a binary mixture of phospholipids and cholesterol is shown in Fig. 1.3, in which the critical point is marked by an asterisk. The snapshots represent the lateral structure of different lipid phases that appear in the phospholipid membrane depending on the temperature and the cholesterol concentration.

It is hypothesized that phase separation, readily observed in model membranes, is also the driving mechanism of lipid raft formation in plasma membranes [Veatch and Keller, 2005; Murtola et al., 2006]. Indeed, it assumes that lipid rafts are small coexisting domains of Lo and Ld phases. We should note that in model membranes, as opposed to plasma membranes, these domains grow (coalesce) in order to reduce the line tension. This minimizes the free energy cost for creation of interfaces between different phases (i.e., lipid rafts and the surrounding host phase).

The major question arises what physical mechanisms prevent the coalescence of phase separating domains in the membrane. To this end, an enormous number of experiments have been applied on plasma and model membranes, and several explanations have

been postulated to rationalize nanoscopic domain formation in plasma membranes. In following sections, we mainly focus on two of those mechanisms, which also set the scope of the thesis chapters that follow.

## 1.4 Membrane-Cytoskeleton Coupling: Quenched Disorder

The cytoplasmic part of the plasma membrane of *eukaryotic* cells extensively interacts with the highly dense polymeric network, namely the cytoskeleton. The cytoskeleton network mainly controls mechanical properties of the cell. It is attached to the plasma membrane via certain anchoring proteins, such as streptavidin. Based on single-molecule tracking techniques, a **picket-fence** model, introduced by Kusumi et al., suggests that actin filaments (fence-like) and anchored proteins to actin filaments (picket-like) would compartmentalize the fluid lipid membrane [Ritchie et al., 2003]. Inside a compartment, lipids diffuse rapidly, but it takes quite some time for lipids to diffuse into another partition (Fig. 1.4).

In a theoretical framework, Yethiraj and Weisshaar [2007] proposed that the cytoskeleton acts as a form of **quenched disorder**. Quenched disorder is introduced by randomly distributed static obstacles in the membrane. It is known that presence of quenched disorder in a system may alter its phase behaviour [Imry and Ma, 1975]. For example, consider a generic model of a two-dimensional (2D) Ising that undergoes continuous phase transition at a critical temperature ( $T_c$ ), belonging to the 2D Ising universality class. Introduction of even small amount of impurities into this system, as randomly distributed frozen spins, will change the universality class to one of the random field Ising model. Crucial is that the impurities have a preferred affinity for one of the lipid species [Fischer and Vink, 2011]. The latter has no critical point and thermodynamically is always in one-phase region. Therefore, presence of quenched disorder in the plasma membrane, due to the cytoskeleton network or anchored proteins, importantly prevents growing of phase separating domains. This can be probed in model membranes as is addressed in chapter 3. In that case, the surface roughness of the solid substrate in a supported model membrane induces quenched disorder in the phospholipid membrane that consequently prevents the main phase transition in a single-component membrane.

Another theoretical attempt to address the existence of the raft-like structure is to regard them as critical fluctuations in the plasma membrane. Indeed, the macroscopic

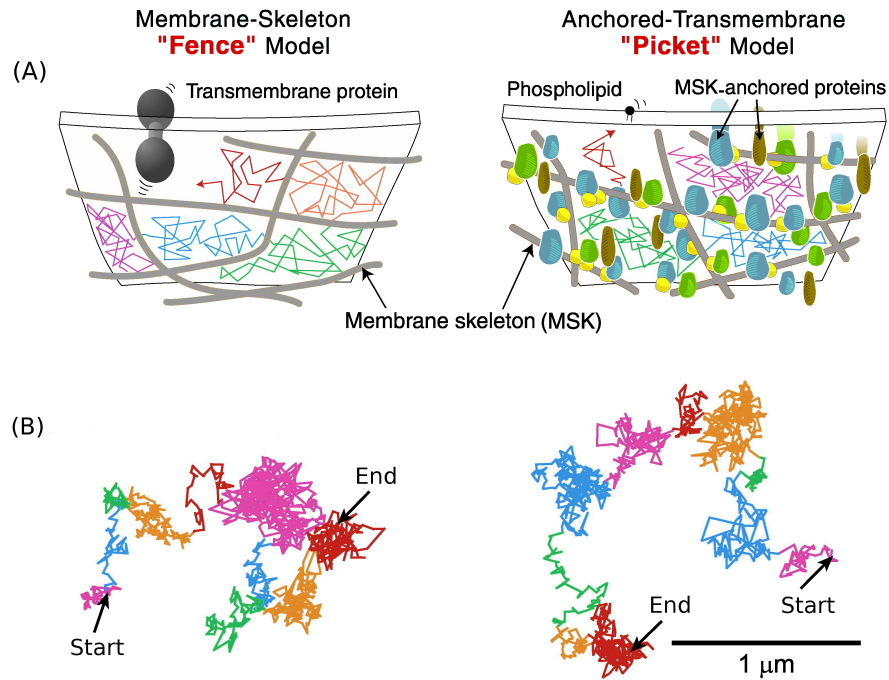


**Figure 1.4:** (A) Schematic drawing showing the membrane-skeleton meshwork, which acts as a fluctuating barrier for the diffusion of membrane proteins (membrane-skeleton fence model), and lipids (anchored-transmembrane picket model). (B) The diffusion paths of fluorescently labeled membrane proteins (or lipids). Different colours indicate diffusion within membrane compartments. (Adopted from Kusumi et al., 2005.)

phase separation is not observed in membranes with a lipid composition resembling the inner leaflet of the plasma membrane [Wang and Silviu, 2001]. In addition, the membrane extracted directly from the living cell demixes at a temperature much lower than the physiological one [Veatch et al., 2008]. Therefore, the macroscopic phase separation of the bilayer membrane is supposed to be eliminated or occur at a very low temperature, meaning the membrane at physiological temperature lies in the one-phase region. The hypothesis of critical fluctuations argues that the plasma membrane composition is tuned in such a way that the system resides in one-phase region, yet in the vicinity of the demixing critical point [Veatch et al., 2007; Honerkamp-Smith et al., 2009]. The size of the critical fluctuating domains is constrained by the influence of the cytoskeleton network. Although the hypothesis of critical fluctuations is supported by recent studies on model membrane, it lacks a detailed description of the small difference (contrast) between composition of the fluctuating domains [Shlomovitz and Schick, 2013]. Moreover, if biologically relevant, an intricate mechanism must have evolved to keep all membranes tuned to criticality.

## 1.5 Curvature-induced Microemulsion

In an alternative view, it is considered that small domains in composition of the plasma membrane are those of a microemulsion. Sam Safran et al. proposed that microemulsion domains are introduced by line-active agents [Brewster et al., 2009]. The presence of line-active agents reduces the interfacial line tension of the domains similarly to what happens for the mixture of oil and water when amphiphilic molecules are introduced. The possible candidates for such surfactant-like agents in the plasma membrane could be the hybrid lipid molecules with one saturated and one unsaturated hydrocarbon chain, in favor of Lo and Ld phases, respectively. However, the domain formation in a ternary mixture of saturated phospholipids like DPPC, DSPC, and cholesterol cannot be fully explained by this hypothesis. It had been already shown by Leibler and Andelman [1987] that a coupling between internal degrees of freedom of the plasma membrane and its shape introduces undulated phases in the membrane. Schick [2012], therefore, extended the idea in a mean-field framework and suggested that the microemulsion domains do not necessarily require to be brought about by line-active molecules. He developed a hypothesis by considering a coupling between local composition difference of the bilayer membrane and its local curvature. Such coupling leads to microemulsion in one-phase region which is still a (thermodynamically) disordered phase but not structureless. In this case, the size of microemulsion domains are determined by elastic properties of the membrane rather than only lipid-lipid interaction. Chapter 4 will cover the effect of the curvature on the phase separating lipid membrane (Fig. 1.5).

The membrane curvature is the deflection in plasma membranes when two-dimensional fluid is embedded into third dimension by bending and stretching. It is an active means in many cellular processes such as growth, division, motility, endocytosis, and exocytosis. Indeed, some cellular activities like cell fusion and cell budding are associated with highly curved regions in the plasma membrane [McMahon and Gallop, 2005]. The membrane curvature, moreover, regulates partitioning in the membrane plane that sort proteins with different architecture and certain functions correspondingly (Fig. 1.5) [Semrau and Schmidt, 2009]. The membrane curvature can be induced by thermal fluctuations and undulations, or spontaneously by intrinsic architecture of membrane constituents, i.e., lipids and proteins. In addition, extracellular components, including adhesion sites [Farago, 2011] and cytoskeletal structure, may constrain the membrane deformation and consequently induce curvature. The latter will be considered in chapters 5 and 6.

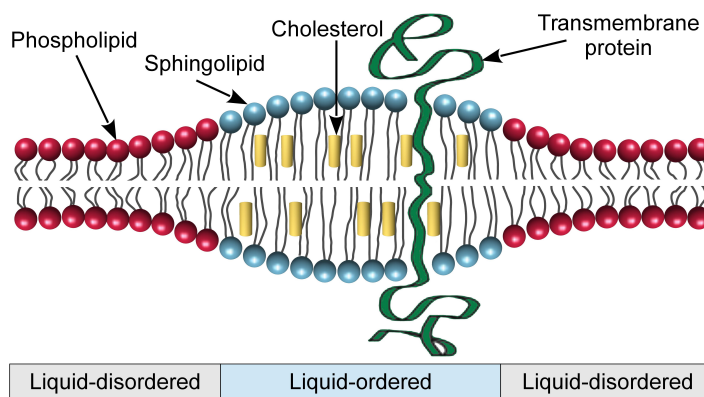


**Figure 1.5:** A schematic drawing showing the side-view of a symmetric lipid bilayer membrane. A coupling between local composition and local curvature can be seen. Lipid rafts are small domains rich in sphingolipids and cholesterol. (Adopted from [Semrau and Schmidt, 2009](#).)

## 1.6 Outline

In this thesis, we mainly focus on two scenarios mentioned above, namely the presence of quenched disorder and curvature, and how these affect lateral lipid domain structure. We should be aware of the fact that all discussed mechanisms, to some extent, may contribute to the organization of components in the lipid membrane. The second chapter introduces simulation membrane models and briefly describes computational methods used in this study. Chapters 3-6 represent the peer-reviewed papers as follows:

Chapter 3, represents computer simulation results of the Pink membrane model for single-component phospholipid membrane. The main phase transition in a phospholipid membrane is studied and the effect of static impurities on the phase separating regime is investigated [[Sadeghi and Vink, 2012](#)].

Chapter 4, describes a phase separating lipid membrane incorporated thermal height fluctuations by considering a composition-curvature coupling. Different resulting phases and the nature of thermotropic phase transitions are discussed [[Sadeghi et al., 2014](#)].

Chapter 5, discusses a series of experiments on solid supported model membranes bound to an actin meshwork. The membrane comprises a ternary mixture of saturated lipids, unsaturated lipids, and cholesterol. An extended simulation model is developed to explain the different pattern formation in the membrane, depending on the type of the membrane-actin cross-linker molecules [[Honigmann et al., 2014](#)].



Chapter 6, extends the simulation model represented in the chapter 5 in order to explain the similar mechanism in cell membranes, in addition to supported membranes [[Sadeghi and Vink, 2014](#)].

Finally, summary and conclusion are given in chapter 7.

## Chapter 2

# Computer Simulations: Models and Methods

Biological systems are often too complex to be understood comprehensively with theoretical approaches and experiments alone. Therefore, simplified model systems are designed and constructed on the basis of phenomenological data and fundamental physical laws. Indeed, models are simplified representations of physical systems that provide systematic description of physical phenomena in great detail. However, in most cases the analytical work and solving mathematical equations is still not feasible. To this end, computer simulations serve as a complementary approach to traditional areas of science, namely theory and experiment. Computer simulations are carried out via two main approaches: Molecular Dynamics that follows deterministic dynamics of constituents, governed by Newtonian equations of motions, and Monte Carlo simulation, considering random nature of complex systems, that is exploited in this study. The aim of this chapter is to describe membrane models and simulation techniques, employed in this thesis, to investigate collective behaviour of biological systems, typically cell membranes.

### 2.1 Models

Biological systems typically contain an enormous number of components that their detailed inclusion in a physical model might not be computationally feasible or even practically useful [Phillips et al., 2012]. However, coarse-grained models, which represent a physical system by a reduced number of degrees of freedom, can provide a substantial insight into understanding the collective behaviour of biological systems [de Pablo, 2011;

[Saunders and Voth, 2013]. A typical problem in connection between experiments and computational models (including exhaustive description), is the distinct resolution in length and time scales [Müller et al., 2003]. Detailed descriptive computational methods usually achieve much finer resolution than what experiments do. In this case, coarse-grained models are considerably beneficial to reach larger length and time scales (depending on the level of coarse-graining, of course). Being favorite example of coarse-grained models, lattice models are extensively applied to biological systems [Lipowsky and Zielinska, 1989; Heberle and Feigenson, 2011; Vink and Speck, 2013]. Due to their simplicity and computational efficiency, lattice models serve as a fruitful tool that can be readily implemented in computers in order to study the phase behaviour of the system under consideration [Mouritsen, 2004]. In what follows, we introduce lattice models of lipid membranes that have been used in this study.

### 2.1.1 Pink Model

An early promising coarse-grained model that considers microscopic interactions between lipid hydrocarbon chains has been introduced by David Pink and co-workers [Pink et al., 1980a,b; Caillé et al., 1980]. The Pink model is a  $q$ -state lattice-based model that has been originally defined to describe the main phase transition in a single-component lipid membrane. It only includes information of hydrocarbon chain conformations and ignores other degrees of freedom such as translation of lipids and head group details. The Pink model is defined on a two-dimensional triangular lattice and in its standard form, it contains  $q = 10$  states per site. The latter are classified into three categories based on conformations of the single acyl chain. Fig. 2.1 displays Pink states as: one ground state with all-*trans* bonds indicating an ordered state (A), eight intermediate excited states including up to three *gauche* bonds (B), and a highly-melted disordered state representing all remaining conformations (C).

The total free energy of the system consists of three terms; internal energy of each acyl chain, van der Waals interaction between adjacent acyl chains, and an effective lateral pressure coupled to the cross-sectional area per any acyl chain. The simplicity and lattice nature of the Pink model allow investigation of large system size as required in probing phase transitions. However, a rigorous description of the main transition in the Pink model requires an appropriate finite-size scaling analysis. The latter needs to be considered in order to deal with finite-size effects present in computer simulations (see Section 2.6). Such analysis was not properly performed for the Pink model to date

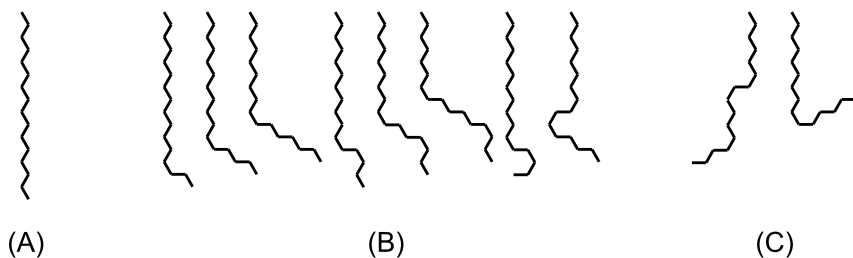


**Figure 2.1:** Chain conformations of the Pink model. **(A)** The ground state with all-*trans* bonds, **(B)** eight intermediate excited states containing up to three *gauche* bonds, and **(C)** highly-melted state.

although it had been introduced long ago. Chapter 3 describes an accurate Monte Carlo simulation of the Pink model and covers finite-size scaling analysis to address the main transition in this model.

As an interesting extension to the Pink model, we introduce immobilized impurities into the system in order to investigate the effect of quenched disorder on the phase transition. In solid-supported model membranes, the surface roughness of the substrate, e.g., glass, may cause presence of such impurities. To implement this effect in the model, we consider impurities as frozen chain conformations that are randomly distributed in the membrane. Our results confirm the experiments that demonstrate no phase transition in solid-supported model membranes in presence of irregular surface roughness [Charrier and Thibaudau, 2005]. In addition, the patterns we observe resemble those of experiments performed at the Max Planck Institute for Biophysical Chemistry with whom we collaborate [Honigmann et al., 2013].

### 2.1.2 Two-dimensional Membrane Model with Height Deformations: The Curvature-Composition Coupling

Demixing into coexisting (liquid-ordered/liquid-disordered) phases in model membranes is shown to support critical behaviour indicating the expected universality class, i.e., 2D Ising model [Veatch et al., 2008; Honerkamp-Smith et al., 2008; Connell et al., 2013]. This motivates to represent the model lipid membrane composed of a binary mixture of liquid-ordered and liquid-disordered phases by a 2D Ising model [Machta et al., 2011]. The latter macroscopically phase separates below a critical temperature  $T_c$  as it is observed in experiments [Veatch and Keller, 2003]. However, membrane models such as

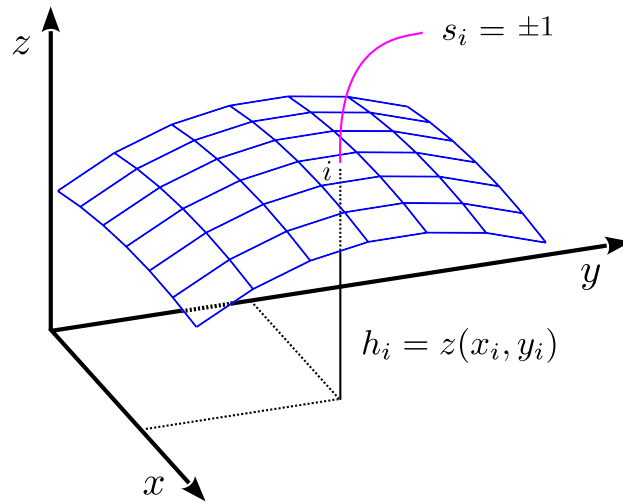


**Figure 2.2:** Out-of-plane deformation of a nearly flat two-dimensional lipid membrane model. The 2D Ising model represents lipid phases as spin up for liquid-ordered and spin down for liquid-disordered phases. The height of lattice site  $i$  is considered as  $h_i$ , according to Monge representation.

Pink model (designed to study main phase transition) and simple 2D Ising (introduced to capture miscibility transition), all assume a two-dimensional in-plane representation for the membrane, while the real membrane is not completely flat. In order to incorporate out-of-plane deformations of the lipid membrane, we developed a 2D Ising-like model that also assigns a real number as height to each lattice site (Monge representation). Fig. 2.2 depicts a two-dimensional (Ising-like) membrane model with height deformations. The main ingredient of this model is that there is a coupling between the local composition and the local curvature of the membrane, inspired by experiments [Parthasarathy et al., 2006; Parthasarathy and Groves, 2007; Hsieh et al., 2012].

The total free energy of the system is thus, sum of three terms; lipid-lipid interaction (given by pairwise additive Ising), elastic energy (given by Helfrich energy), and a curvature-composition coupling energy term as

$$\mathcal{H} = \mathcal{H}_{\text{Ising}} + \mathcal{H}_{\text{Helfrich}} + \mathcal{H}_{\text{coupling}} \quad . \quad (2.1)$$

The curvature-composition coupling sort lipids in the membrane accordingly so that regions with negative (positive) curvature (in upper layer) are energetically favorable for liquid-ordered (liquid-disordered) phase, (Fig. 2.3). The corresponding energy term,  $\mathcal{H}_{\text{coupling}}$  is given by a curvature-composition coupling constant  $\gamma$ . The latter indicates

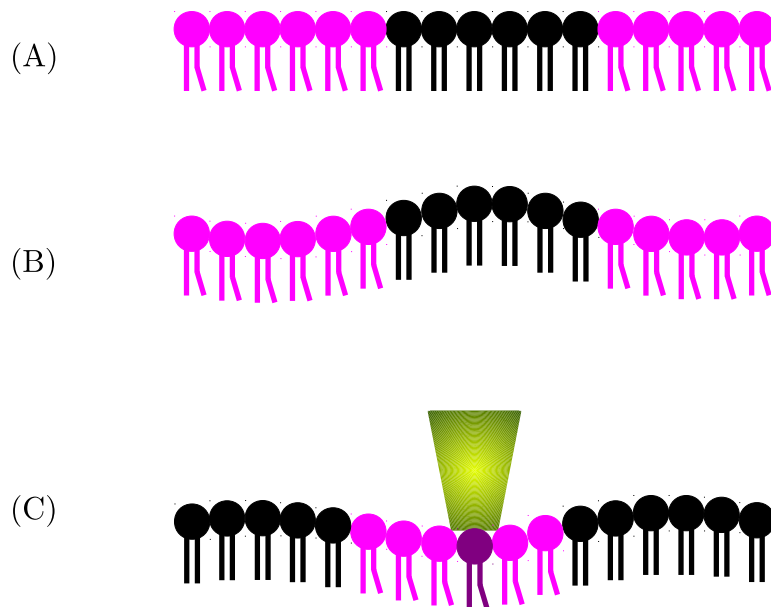


**Figure 2.3:** Side view depiction of the (upper) monolayer of a lipid membrane. The saturated (unsaturated) lipids shown in black (magenta) correspond to liquid-ordered (liquid-disordered) phase. **(A)** A free two-dimensional membrane (Ising-like model) which is completely flat. **(B)** Out-of-plane deformations of a free lipid membrane. A coupling between local composition and local curvature sort lipids in the membrane accordingly. **(C)** A bound lipid membrane to an actin network (not shown). The cross-linker molecule (shown in green) that energetically interact with surrounding lipids, locally induces curvature. The model depicted here forms the central basis of chapters 4-6.

the strength of the coupling so that for  $\gamma = 0$ , no curvature-composition coupling is observed and the critical 2D Ising will be captured. As it is shown in chapter 4, inclusion of such coupling with sufficiently large strength alters the nature of the phase transition in a membrane comprising a binary mixture of liquid-ordered and liquid-disordered phases. We proposed a simulation phase diagram that slightly modifies the one given in the mean-field framework.

In line with recent series of experiments, the model is developed further to include the effect of an actin network [Machta et al., 2011; Ehrig et al., 2011a]. The key feature of the model is schematically demonstrated in Fig. 2.4. The sketch shows a lipid membrane which is bound to an actin network via cross-linker molecules (pinning sites). To mimic the actin network in the model, we consider a Voronoi tessellation, superimposed on the Ising lattice. According to experiments, pinning sites are randomly distributed along

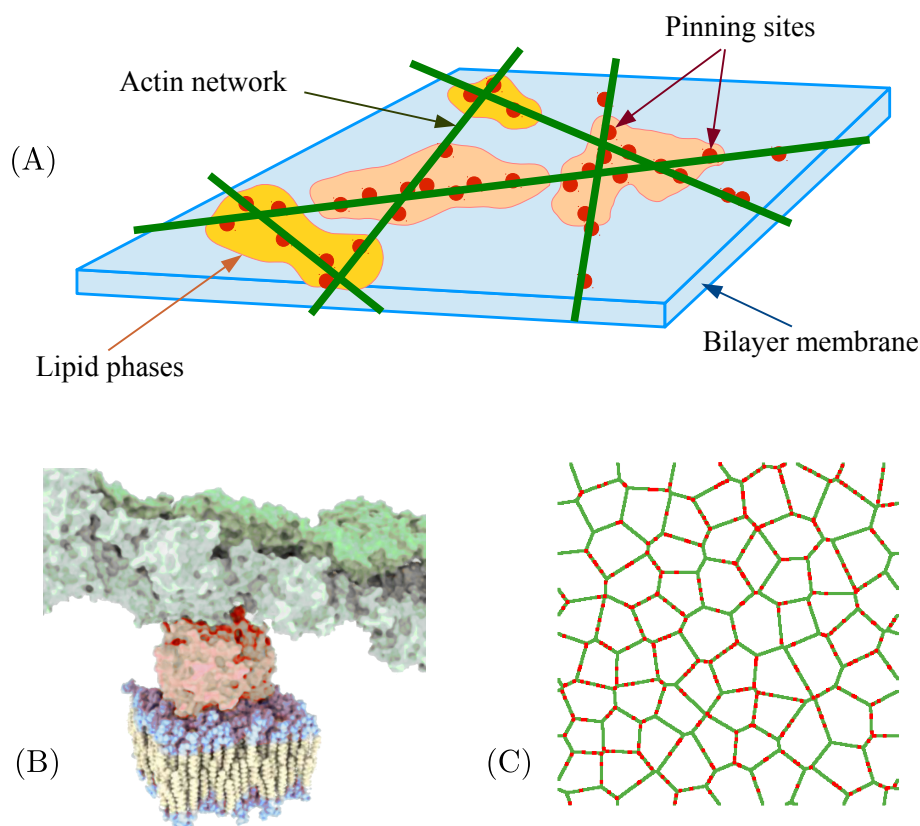


**Figure 2.4:** Schematic representation of a lipid bilayer which is bound to an actin network (A). Actin strands are attached to the membrane via cross-linker molecules (pinning sites) (B). The latter are randomly distributed along actin strands and have different affinity for (liquid-ordered/liquid-disordered) lipid phases. To implement the effect of pinning sites on the phase behaviour of the lipid membrane in simulations, a Voronoi tessellation is employed to represent the actin network (C).

the actin fibers, i.e., Voronoi strands in the model. The strength of energetic interaction between pinning sites and surrounding lipids may be different, (depending on the type of cross-linker molecules). In fact, different pinning sites result in different lipid phases that are correlated with actin fibers. However, we note that this interaction cannot capture all experimental data. For example, in case of (almost) neutral pinning sites, simulations will lead to a diluted 2D Ising model which macroscopically phase separate. This is in contrast to experiments in which apparent microscopic domains are observed (chapter 5). That means, other mechanisms should play a role in domain formation in the lipid membrane bound to an actin network. To this end, we further proposed that pinning sites constrain height deformations of the membrane and induce curvature locally (Fig. 2.3C). Hence, an additional term in free energy should be considered to

address how pinning sites influence the membrane curvature and consequently lipid distribution. The latter results in a mechanism that imprints the actin network pattern on the membrane via combination of energetic interaction of cross-linker molecules with lipids and a curvature-comparison coupling (chapter 5). We emphasize that the latter is required to fully describe the lateral domain formation observed in experiments. Moreover, it induces lateral structure in the membrane independent of any phase transition the lipid membrane may exhibit (chapter 6).

## 2.2 Monte Carlo Simulations of Phase Transitions

Monte Carlo simulations employ the stochastic nature of many-body complex systems. A standard Monte Carlo move considers a given system in a initial state  $\mu$ , and proposes a new state  $\nu$ . Realizations of the Monte Carlo scheme should be proposed in a way that satisfies “ergodicity”. The latter is required in order that all possible states in the phase space be accessible. The new configuration is then accepted with a acceptance probability. For instance, in the often used Metropolis algorithm, this criterion is given by  $P_{\text{acc}}(\mu \rightarrow \nu) = \min\{1, e^{-\Delta\mathcal{H}/k_{\text{B}}T}\}$ , where  $\Delta\mathcal{H}$  is the energy difference between initial and final configurations,  $k_{\text{B}}$  the Boltzmann constant, and  $T$  the temperature. The Monte Carlo move should also fulfill the “detailed balance” condition in order that the ultimate distribution satisfies the known equilibrium one (typically Boltzmann distribution) [Newman and Barkema, 1999; Binder and Heermann, 2010].

In what follows, we explain how Monte Carlo simulations are used to study phase transitions in membrane models. To this end, we introduce the order parameter distribution and note its relation to the free energy of the system. To overcome the free energy barrier (particularly in phase coexisting regime), we employ a rigorous Monte Carlo scheme, namely successive umbrella sampling. Furthermore, we perform extrapolation of simulation data obtained at certain model parameters to nearby values, that enhances the computational efficiency. Finally, an appropriate finite-size scaling is implemented to deal with finite-size effects present in computer simulations.

## 2.3 Order Parameter Distribution

The key parameter in probing the phase behaviour of a system, frequently used in this study, is the distribution of the order parameter,  $P(m)$ . The physical relevance is its



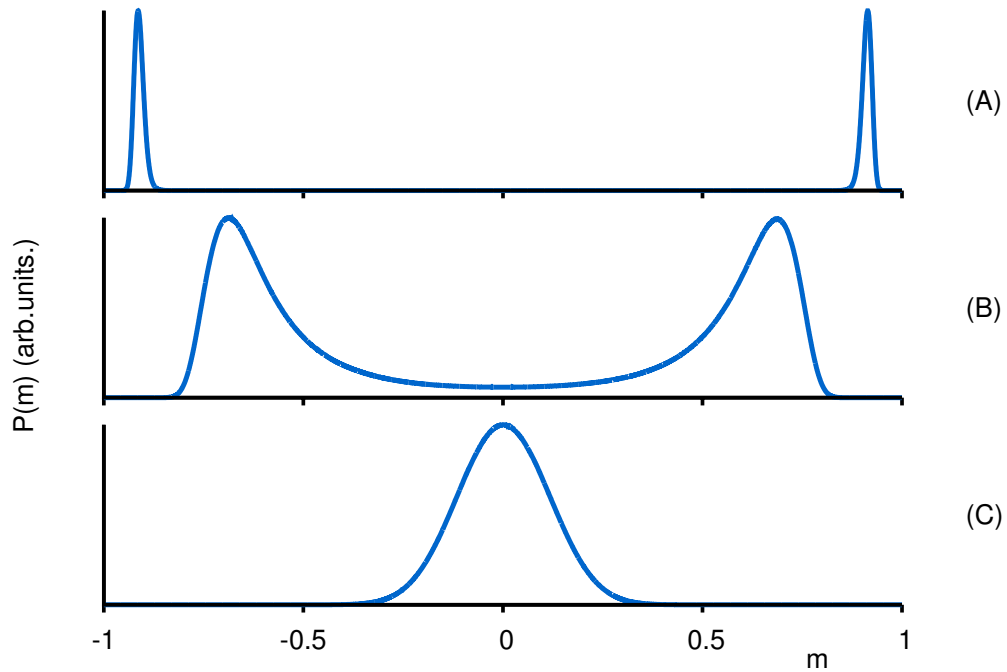


**Figure 2.5:** Probability distribution of order parameter  $P(m)$  of a 2D Ising model at different temperature. (A) At low temperature  $T < T_c$ , a bimodal distribution is observed corresponding to phase coexistence. (B) As the critical temperature is approached  $T \approx T_c$ , two peaks are overlapping. (C) At high temperature  $T > T_c$ , the system appears in one-phase region indicated by a single peak in the order parameter distribution.

relation to the free energy,  $F(m) = -k_B T \ln P(m)$ . Local minima in free energy reflect phases (according to Landau theory) and hence, by measuring  $F$ , the free energy barrier can be studied. The order parameter  $m$ , changes abruptly when the system undergoes a phase transition. In a generic 2D Ising model with spins  $s_i \in \{-1, 1\}$ , the order parameter is magnetization,  $m = L^{-2} \sum_i s_i$ , where  $L$  is the linear extension of the system and the sum is over all lattice sites  $i$ . During the course of simulation,  $m$  fluctuates and thus,  $P(m)$  is the probability that the system is observed with magnetization  $m$ .

The behaviour of the order parameter distribution  $P(m)$  indicates the nature of the phase transition. It is possible to locate the critical temperature  $T_c$ , at which the continuous phase transition in a critical system occurs. This is shown for a 2D Ising model in Fig. 2.5. At low temperature  $T < T_c$ , the system can be in either ferromagnetic states, in which the majority of spins are up or down. This leads to a bimodal distribution of order parameter with peaks distinctly separated from each other. Bimodality indicates phase coexistence that can be achieved under certain conditions [Borgs and Kappler, 1992; Orkoulas et al., 2001]. As the temperature approaches the critical one  $T \approx T_c$ , two peaks

overlap continuously and finally merge into a single peak beyond the critical temperature  $T_c$ . In fact, in a system at high temperature  $T > T_c$ ,  $P(m)$  is basically single-peaked around zero. This manifests a Gaussian distribution as a result of randomly setting up and down spins.

## 2.4 Successive Umbrella Sampling

In principle, it is possible to measure  $P(m)$  directly from Monte Carlo simulation data. However, difficulties may arise especially in cases where systems are at low temperature. For example, a 2D Ising system might become trapped in either of ferromagnetic phases. In such cases, it takes quite some time for the system to overcome the barrier between the two peaks. Therefore, the whole range of the order parameter might not be sampled properly. In order to measure  $P(m)$  accurately, one must employ an alternative Monte Carlo simulation method. An appropriate technique is provided by the successive umbrella sampling method, in which the entire range of  $m$  is sampled in small overlapping windows consecutively [Virnau and Müller, 2004; Müller and de Pablo, 2006]. To this end, the known range of order parameter  $m$ , for example, in simple case of 2D Ising, is divided into windows (sub-intervals)  $[m_{i-1}, m_i]$ , where  $i = 1, \dots, N$  and  $N$  is the total number of windows, (Fig. 2.6). Each window  $i$  is split into two bins denoted by positive and negative signs, corresponding to right and left, respectively. The right (left) bin contains the right (left) boundary value of the sub-interval. The binning is set in a way that two successive windows overlap. The measurement is performed in each window individually for certain number of Monte Carlo moves. This is done such that the magnetization of the system is kept constrained to not exceed the boundaries of the sub-interval. Therefore, moves that results in magnetization outside of the window are rejected. The contribution of each window  $i$  into  $P(m)$  is then  $H_i^+/H_i^-$ ; the ratio of how often the system is visited with magnetization  $m_i$  and  $m_{i-1}$ , in right and left bins, respectively. Thus, the ratio for the first sub-intervals is  $H_1^+/H_1^-$ , the second  $H_2^+/H_2^-$ , and so on. One should note that  $H_1^+$  and  $H_2^-$  are simulated in the same bin but in two consecutive windows, i.e., overlapping states are sampled twice. The simulation is carried out in all individual windows successively and corresponding ratios are recorded. Finally, the probability of the system with magnetization  $m_i$  can be constructed as follows:

$$P(m_i) = P(m_0) \cdot \frac{H_1^+}{H_1^-} \cdot \frac{H_2^+}{H_2^-} \cdots \frac{H_i^+}{H_i^-} \quad , \quad i = 1, \dots, N \quad , \quad (2.2)$$

provided a good estimation for  $P(m_0)$ , which is an initial weight for the first window.

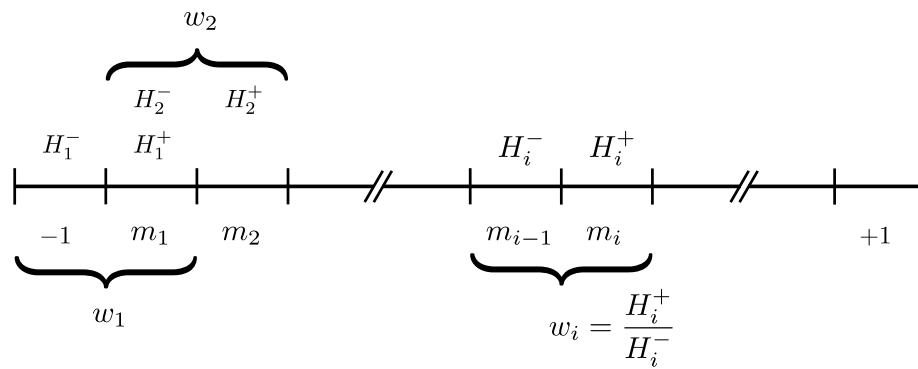


**Figure 2.6:** Successive umbrella sampling: the range of the order parameter  $m$  is divided into  $N$  overlapping windows. Simulations run in windows consecutively and Monte Carlo moves resulting in exceeding window boundaries are rejected. Each window  $i$  is split into two bins and its contribution to  $P(m)$ , i.e.,  $w_i$  is measured as the ratio of how often the system is visited in right and left bins (with magnetization  $m_i$  and  $m_{i-1}$ ), respectively.

A practical advantage of using successive umbrella sampling, in comparison to other methods like Wang-Landau sampling [Wang and Landau, 2001], is that the CPU time can be divided over the various bins easily.

## 2.5 Histogram Reweighting

Another crucial ingredient in this study that facilitate Monte Carlo simulations is the histogram reweighting. The idea of histogram reweighting is to extrapolate information obtained in a single Monte Carlo simulation at a single state point without running extra simulations. In fact, each simulation measures the order parameter distribution  $P(m)$  at a certain state point in a multi-dimensional phase diagram that is characterized by all model parameters. One should note that in most cases, simulations are very demanding in CPU time and memory storage. The situation becomes even more troublesome when one has to perform more simulation runs for different system sizes (in finite-size scaling), and different quenched disorder realizations (in quenched averaging). Therefore, in order to economize simulation time and energy, it is advantageous to use an approximation in measuring physical quantities in a range of control parameters. To this end, histogram reweighting offers a powerful means that is used to extrapolate generated data at certain points to nearby values [Ferrenberg and Swendsen, 1988, 1989].

To implement the histogram reweighting, one performs a single simulation at a state point, characterized by temperature  $T$  and magnetic field  $H$  in Ising model, and measures the probability distribution  $P(m)|_{T,H}$ . The basis of the histogram reweighting is on the fact that properties of the system can be determined by this probability distribution, given in an appropriate ensemble [Landau and Binder, 2005]. In the canonical ensemble, the latter distribution is expressed as  $P(m)|_{T,H} = \frac{1}{Z_{T,H}} \rho(m) e^{-HL^2m/k_B T}$ , where  $Z_{T,H}$  is the canonical partition function,  $\rho(m)$  the density of states with magnetization  $m$ , and exponential term the Boltzmann factor with  $L$  the linear extension of the system. The density of states  $\rho(m)$  can be measured from a single simulation, (this is given by successive umbrella sampling). Thus, an estimates is provided for the order parameter distribution at some (nearby) values of  $H'$  as

$$P(m)|_{T,H'} \propto P(m)|_{T,H} e^{-(H'-H)L^2m/k_B T} \quad . \quad (2.3)$$

Histogram reweighting in temperature requires additional information that is given by a joint two-dimensional probability distribution  $P(m, E)$ , where  $E$  is the energy. The latter distribution is measured by using a multiple histogram reweighting in which, a number of simulations are performed at different state points and generated data are interpolated between simulated points. However, this is computationally expensive due to the remarkably increasing memory usage. Hence, in order to reduce computational efforts, we apply an approximation and still use the single histogram reweighting [Vink, 2014]. To this end, we Taylor expand the order parameter probability distribution at temperature  $T'$  as

$$\begin{aligned} \ln P(m)|_{T',H} = \ln P(m)|_{T,H} + \Delta\beta \left. \frac{d \ln P(m)}{d\beta'} \right|_{\beta'=\beta} + \\ \frac{1}{2} (\Delta\beta)^2 \left. \frac{d^2 \ln P(m)}{d\beta'^2} \right|_{\beta'=\beta} + \dots \quad , \end{aligned} \quad (2.4)$$

where  $\Delta\beta = \beta' - \beta$  with  $\beta = 1/k_B T$ . We note that from canonical partition function one writes  $\partial \ln Z / \partial \beta = \langle -E \rangle$  and  $\partial^2 \ln Z / \partial \beta^2 = \langle E^2 \rangle - \langle E \rangle^2$ . Hence, the Eq. (2.4) can be estimated up to second order by

$$\ln P(m)|_{T',H} = \ln P(m)|_{T,H} + \Delta\beta \langle -E \rangle + \frac{1}{2} (\Delta\beta)^2 (\langle E^2 \rangle - \langle E \rangle^2) \quad , \quad (2.5)$$

where higher order derivatives are dropped because they contribute little. Thus, it is not required to measure a full energy distribution but only the first two moments, namely  $\langle E \rangle$  and  $\langle E^2 \rangle$ . The latter are readily stored during Monte Carlo simulation for each bin.

## 2.6 Finite-size Scaling

Phase transitions are characterized by singularities in the free energy or its derivatives (thermodynamic observables such as susceptibility, specific heat, etc) [Goldenfeld, 1992]. These singularities at phase transitions occur in thermodynamic limit where the number of interacting constituents in the system goes to infinity, (and consequently the system size  $L \rightarrow \infty$ ). Computer simulations, however, are performed on finite-size systems which influence the known behaviour of thermodynamic quantities at phase transition. For instance, in 2D Ising model, the susceptibility  $\chi = \beta L^2 (\langle m^2 \rangle - \langle |m| \rangle^2)$  diverges to infinity as the system approaches the critical point  $T_c$ . Simulations of finite-size systems, however, do not display such divergence. Instead, a rounded maximum is observed at some temperature  $T'_c$ , which is shifted from  $T_c$  [Newman and Barkema, 1999]. As the system size increases, the maximum susceptibility increases and the temperature at which the rounded maximum of susceptibility is observed, approaches  $T_c$ . Hence, a divergence to infinity at  $T_c$  is expected to be observed in thermodynamic limit,  $L \rightarrow \infty$ . That means, simulations of a finite system already contains useful information about phase transition in the infinite one. Employing this fact, finite-size scaling suggests to perform several simulations for different finite system sizes and extrapolate the obtained results to thermodynamic limit. We emphasize that the use of finite-size scaling is an important issue in probing phase transition in computer simulation models, however it is not yet standard in biophysics, at the time of writing. As we will show, the lack of an appropriate finite-size scaling can lead to the erroneous identification of phase transitions [chapter 3].

An advantage of finite-size scaling is to provide a standard tool to investigate the nature of phase transitions in finite systems. In critical systems, the correlation length  $\xi$  diverges to infinity as the critical point is approached. The latter measures the length scale over which fluctuations in order parameter are correlated. The finite-size scaling hypothesis is based on the fact that correlation length  $\xi$  should not exceed the lateral extension  $L$  of a finite system [Fisher and Barber, 1972; Stanley, 1987]. Indeed, the standard finite-size scaling Ansatz assumes that the correlation length is comparable to the system size,  $\xi \approx L$ . In thermodynamic limit, the correlation length  $\xi$  and susceptibility  $\chi$  scale as [Goldenfeld, 1992]

$$\begin{aligned} \xi &\propto |t|^{-\nu} \quad , \\ \chi &\propto |t|^{-\gamma} \quad , \end{aligned} \tag{2.6}$$

where  $t = (T - T_c)/T_c$  is the reduced temperature, and  $\nu$  and  $\gamma$  are critical exponents. By eliminating  $|t|$  from Eq. (2.6) and substitute Ansatz  $\xi \approx L$ , one can readily obtain

$$\chi \propto L^{\gamma/\nu} \quad , \quad (2.7)$$

that immediately follows scaling expressions for the maximum susceptibility  $\chi_m \propto L^{\gamma/\nu}$ , and the shifted temperature  $T = T_c (1 + xL^{-1/\nu})$ , with coefficient  $x$  to be obtained [Newman and Barkema, 1999]. The coefficient of proportionality in Eq. (2.7),  $\bar{\chi}(L^{1/\nu}t)$ , is a universal scaling function that its behaviour around the critical point does not depend on the system size. That means, plotted  $\bar{\chi}(L^{1/\nu}t) = L^{-\gamma/\nu}\chi$  versus  $L^{1/\nu}t$ , for different system sizes, will collapse, (provided proper values for critical exponents) [Newman and Barkema, 1999].

First-order phase transitions, on the other hand, do not include divergence of  $\xi$  as the transition is approached. Instead, they display phase coexistence at phase transition under certain conditions. In this case, finite-size scaling are governed by the volume of the system, i.e.,  $L^2$  for two-dimensional system [Binder, 1987; Lee and Kosterlitz, 1991]. For example, the maximum susceptibility  $\chi_m$  of a 2D Ising system at  $T < T_c$  (first-order phase transition) is scaled as  $\propto L^2$  and its location is shifted  $\propto L^{-2}$  [Billoire et al., 1992].

A crucial element of the analysis in this thesis is thus to perform simulations for different system sizes  $L$ . The way in which the susceptibility  $\chi$  scales with  $L$  allows us to distinguish first-order phase transitions from continuous ones (and measure the ratio  $\gamma/\nu$  in the latter case).

## Chapter 3

# Main transition in the Pink membrane model: Finite-size scaling and the influence of surface roughness

Sina Sadeghi and Richard L. C. Vink (2012),  
Physical Review E, 85(6):061912.

Published 18 June 2012.

DOI: [10.1103/PhysRevE.85.061912](https://doi.org/10.1103/PhysRevE.85.061912)

The manuscript presents a simulation study of the Pink membrane model. The study was designed by Richard Vink. I performed all simulations (including from-scratch code writing), data acquisition, and data analysis. The manuscript was written by me with revisions from Richard Vink.

## Abstract

We consider the main transition in single-component membranes using computer simulations of the Pink model [D.A. Pink *et al.*, [Biochemistry](#) **19**, 349 (1980)]. We first show that the accepted parameters of the Pink model yield a main transition temperature that is systematically below experimental values. This resolves an issue that was first pointed out by Corvera and co-workers [[Phys. Rev. E](#) **47**, 696 (1993)]. In order to yield the correct transition temperature, the strength of the van der Waals coupling in the Pink model must be increased; by using finite-size scaling, a set of optimal values is proposed. We also provide finite-size scaling evidence that the Pink model belongs to the universality class of the two-dimensional Ising model. This finding holds irrespective of the number of conformational states. Finally, we address the main transition in the presence of quenched disorder, which may arise in situations where the membrane is deposited on a rough support. In this case, we observe a stable multi-domain structure of gel and fluid domains, and the absence of a sharp transition in the thermodynamic limit.

## 3.1 Introduction

Lipid membrane bilayers are abundant in nature and to understand their properties is of paramount importance [[Simons and Ikonen, 1997](#); [Engelman, 2005](#); [Jacobson et al., 2007](#)]. One aspect that has received much attention are collective phenomena (phase transitions) taking place in these systems. Among the different phase transitions that can occur [[Mouritsen, 1987](#); [Risbo et al., 1995](#); [Keller et al., 2005](#); [Kranenburg and Smit, 2005](#)], the main phase transition is presumably the most important and well-studied one [[Nagle, 1980](#); [Mouritsen, 1991](#)]. This transition, typically driven by the temperature  $T$ , is between a “gel” and a “fluid” phase. At low  $T$ , the bilayer is in the gel phase (characterized by nematic chain order of the lipid tails), while at high  $T$  the bilayer assumes the fluid phase (characterized by the absence of nematic chain order).

Computer simulations have become a well-established tool to model the main transition. The challenge in simulations is to strike a balance between the level of detail to include, and the time and length scale one wishes to address [[Müller et al., 2006](#)]. Since collective phenomena involve many molecules and entail large length scales it is clear that, in order to describe the main transition, a significantly coarse-grained particle model is crucial. Strictly speaking, one needs to address the thermodynamic limit (infinite



particle number) since only there phase transition properties become properly defined. Indeed, the need for coarse-grained modeling of lipid bilayers is well recognized [Marrink et al., 2005; Orsi et al., 2010; Hömberg and Müller, 2010].

An early and highly successful coarse-grained approach to study the main transition has been the particle model introduced by David Pink and co-workers [Pink et al., 1980a,b; Caillé et al., 1980]. In this model, the so-called Pink model, only the *orientational* degrees of freedom of the hydrophobic lipid tails are included, while the *positional* degrees of freedom of the hydrophilic heads are disregarded. This model, due to its simplicity, allows for the investigation of very large systems, and the nature of the main transition can be probed in great detail. Indeed, key features of the main transition in the Pink model compare well to experiments [Mouritsen et al., 1983], and the model continues to be used to this day [Surovtsev and Dzuba, 2009].

However, despite the great success the Pink model has enjoyed, there remain some open questions. One problem is that, due to its simplicity, the Pink model necessarily ignores a number of features that exist in realistic membranes (for instance, translational ordering of polar heads, the coupling between translational and orientational degrees of freedom, and membrane height fluctuations). Problems such as these are unavoidable in any simplified model description, and this is *not* the issue that we wish to address in the present paper. Instead, the aim of this paper is to highlight the importance of carefully analyzing finite-size effects in simulation data. The motivation for doing so is provided by Corvera et al. [1993], where it was noted that the Pink model at the experimentally determined main transition temperature does *not* undergo any phase transition. While in systems of finite size there were indications of a transition, these vanished in larger systems.

This raises the question as to why no transition could be detected. The aim of this paper is to resolve this issue. As it turns out, to properly model the main transition, a finite-size scaling study is essential. Computer simulations inevitably deal with only a finite number of particles, and their output will depend on the number of particles used, especially near phase transitions. Finite-size scaling provides the framework to systematically extrapolate simulation data to the thermodynamic limit. To date, finite-size scaling studies of the Pink model are scarce, with work of Corvera et al. [1993] being a notable exception. The present paper aims to fill this gap. Our main finding is that, in order to observe the main transition in the Pink model at experimentally relevant temperatures, one of the model parameters needs to be adjusted. This follows quite naturally when one realizes that the universality class of the Pink model is just the

one of the two-dimensional (2D) Ising model [Pink et al., 1980a]. As we will show for three lipid species, the “standard” Pink model parameters yield a critical temperature distinctly below the experimental main transition temperature. In other words, at the experimental main transition temperature, the “standard” Pink model is inside its one-phase region where no phase transition can occur. Consequently, a “re-tuning” of the standard Pink parameters is urgently needed.

As an application, we also address the fate of the main transition in the presence of quenched (immobilized) impurities using the Pink model. The experimental motivation to do so is that this situation may resemble that of a membrane supported on a rough substrate. In binary lipid mixtures, the effect of such impurities on lateral phase separation has recently attracted much attention [Yethiraj and Weisshaar, 2007; Gómez et al., 2010; Fischer and Vink, 2011; Machta et al., 2011; Ehrig et al., 2011a; Fischer et al., 2012]. In this paper, we present simulation results for the corresponding scenario in a single-component bilayer undergoing the main transition. Within the framework of the Pink model, we find that quenched impurities prevent the main transition from taking place, already at low impurity concentrations. Instead of the formation of macroscopic gel and fluid domains, we now obtain a stable multi-domain structure, which strikingly resembles experimental results. The theoretical justification is that the impurities induce a change in universality toward the 2D *random-field* Ising class. As is well known, the latter does not support an order-disorder phase transition in the thermodynamic limit [Imry and Ma, 1975; Imbrie, 1984; Bricmont and Kupiainen, 1987; Aizenman and Wehr, 1989].

## 3.2 The Pink model

In the Pink model, the lipid bilayer is assumed to consist of two independent monolayers. Each monolayer is represented by a triangular 2D lattice consisting of  $N$  sites, and each lattice site contains a single lipid chain. Each lipid molecule comprises two independent hydrophobic acyl chains and a hydrophilic polar head. The polar heads are translationally frozen to the lattice, and no particular structure for the polar head groups is assumed. The only degrees of freedom included in the Pink model are the acyl chain conformations. These are not simulated directly (i.e., one does not explicitly model the carbon atoms) but are captured in a coarse-grained fashion whereby the chain conformations are grouped into  $\alpha = 1, \dots, q$  discrete states. The original Pink model uses  $q = 10$ , but we will consider different values also. These states include the ground state ( $\alpha = 1$ ),

State	$\alpha$	$E_\alpha$	$l_\alpha$	$D_\alpha$
Ground state	1	0	$M - 1$	1
Kink	2	$\Gamma$	$M - 2$	4
	3	$\Gamma$	$M - 3$	4
	4	$\Gamma$	$M - 4$	4
	5	$2\Gamma$	$M - 2$	$2(M - 6)$
	6	$2\Gamma$	$M - 3$	$2(M - 8)$
	7	$2\Gamma$	$M - 4$	$2(M - 10)$
	8	$3\Gamma$	$M - 3$	$8(M - 8)$
Disordered	9	$3\Gamma$	$M - 4$	$16(M - 10)$
	10	$E_{10}$	$l_1 A_1 / A_{10}$	$6 \times 3^{M-6}$

**Table 3.1:** The coarse-graining parameters used to describe the acyl chain conformations in the  $q = 10$  Pink model [Pink et al., 1980a,b; Caillé et al., 1980; Mouritsen et al., 1983]. For each state conformation  $\alpha$ , we list the internal energy  $E_\alpha$ , the projected length  $l_\alpha$ , and the degeneracy  $D_\alpha$ . The energy of a single *gauche* bond equals  $\Gamma = 0.45 \times 10^{-13}$  erg, while  $M$  denotes the number of carbon atoms in the chain.

eight low-energy excitations ( $\alpha = 2, \dots, q - 1$ ), while all remaining conformations are grouped into a single disordered state ( $\alpha = q$ ). Each state  $\alpha$  is characterized by three coarse-graining parameters, namely an internal energy  $E_\alpha$ , a cross-sectional area  $A_\alpha$ , and a degeneracy  $D_\alpha$  counting the number of chain conformations with energy  $E_\alpha$  and area  $A_\alpha$ .

### 3.2.1 Coarse-graining parameters

To determine the coarse-graining parameters, we assume that a single acyl chain consists of  $i = 1, \dots, M$  carbon atoms, thereby containing  $M - 1$  carbon-carbon bonds, and that bonds are either in a *trans* or *gauche* configuration. The *trans* configuration yields the lowest energy, while the *gauche* configuration has a slightly higher energy. The energy difference between the *trans* and *gauche* configuration is denoted  $\Gamma$  (Table 3.1). To understand the difference in geometry between *trans* and *gauche* bonds consider a chain segment of four consecutive carbon atoms. The positions of the first three atoms define a two-dimensional plane. In the *trans* configuration, the fourth atom remains in the plane, while in the *gauche* configuration, it leaves the plane, and it can do so inward or outward. Thus, each *gauche* bond is twofold degenerate. In the Pink model, it is assumed that each  $2n$ th *gauche* bond takes the chain back to the original plane, and so

the *gauche* degeneracy is given by

$$G = 2^{\text{ceil}(n/2)} \quad , \quad (3.1)$$

where  $n$  denotes the total number of *gauche* bonds in the chain, and where the function *ceil* means “rounding up” to the nearest integer.

It is convenient to *mathematically* represent the chain conformations on a hexagonal lattice with next-nearest neighbor distance  $2a$ . We emphasize that this lattice is merely an aid to identify the low-energy chain conformations which are needed to set the coarse-graining parameters: It should not be confused with the triangular simulation lattice on which the Pink Hamiltonian will eventually be defined. The carbon atoms are placed on the nodes of the hexagonal lattice following certain rules, and nearest-neighbor connections between atoms represent carbon-carbon bonds. The ground state  $\alpha = 1$  corresponds to the chain conformation that is maximally stretched (Fig. 3.1A). Note that, in the ground state, the atoms are alternately placed on the left and right lattice node, yielding a characteristic “zig-zag” pattern. The ground state by definition contains only *trans* bonds, its internal energy is set to zero as a reference  $E_1 = 0$ , and it is obviously nondegenerate  $D_1 = 1$ . The cross-sectional area of the ground state has experimentally been determined as  $A_1 = 20.4 \text{ \AA}^2$  [Pink et al., 1980b]. We also introduce the projected length  $l$  of the conformation, defined as the difference in the  $z$  coordinate between the carbon atom closest to the head group ( $i = 1$ ) and the one furthest away ( $i = M$ ), with the  $z$  direction as indicated in the figure. For the ground state, it follows that  $l_1 = (M - 1)a$ .

The eight low-energy excitations ( $\alpha = 2, \dots, 9$ ) are obtained by systematically incorporating *gauche* bonds. The effect of such a bond is to disrupt the “zig-zag” pattern of the ground state; that is, one no longer places the atoms alternately on left and right nodes, but also allows for “excursions” whereby for two consecutive atoms the same direction is chosen. Each such excursion corresponds to a *gauche* bond, and has energy cost  $\Gamma$ . The *gauche* bonds are introduced according to the following rules: (1) The two bonds in the chain closest to the head group must always be in the *trans* configuration. In Fig. 3.1, these correspond to the bonds between atoms 1 and 2, and 2 and 3. (2) At most three *gauche* bonds are allowed, and each time such a bond is included there is an energy cost  $\Gamma$ . (3) The projected chain length  $l$  must obey  $l_1 - l \leq 3a$ . (4) The acyl chain cannot fold back onto itself. In the coordinate system of Fig. 3.1, this means that the  $z$  coordinates of the atoms must obey  $z_{i+1} \geq z_i$ .

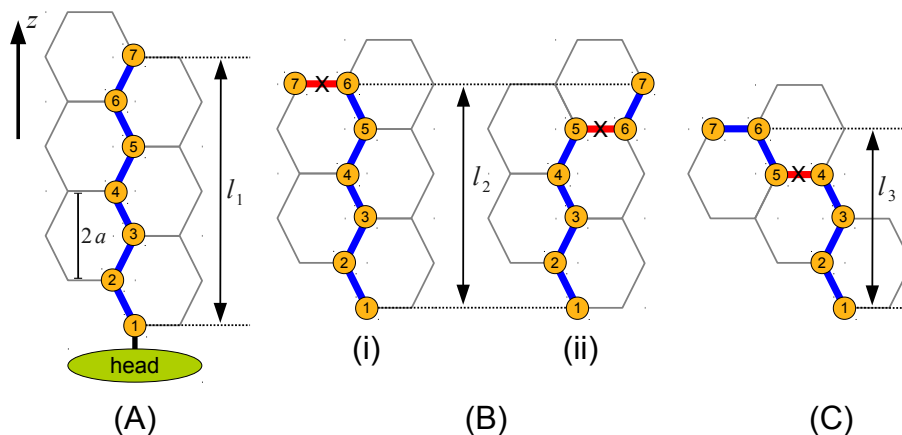


**Figure 3.1:** Typical chain conformations of the Pink model with  $M = 7$ , showing (numbered) carbon atoms placed on the nodes of a hexagonal lattice. The atom connected to the head group is labeled  $i = 1$  but for clarity the head group is only drawn for the ground state. The  $z$  direction indicates the bilayer normal, while the vertical double arrows indicate the projected length. **(A)** The ground state  $\alpha = 1$ , consisting of only *trans* bonds. **(B)** The two conformations that constitute the first excited state  $\alpha = 2$  containing one *gauche* bond (marked with a cross). **(C)** Conformation belonging to the second excited state  $\alpha = 3$ . The internal energy is the same as in (B) but the projected length is shorter (the other  $\alpha = 3$  conformation has the *gauche* bond between atoms 3 and 4).

Following these rules, we show in Fig. 3.1B the chain conformations (i) and (ii) that form the first excited state  $\alpha = 2$ . In (i), a single *gauche* bond is placed at the very chain end, while in (ii) it is placed at the second-last position. One immediately sees that both conformations have the same energy  $E_2 = \Gamma$ , and the same projected length  $l_2 = (M - 2)a$ . To compute the cross-sectional area, one assumes volume conservation for the lipid chains:  $A_\alpha l_\alpha = A_1 l_1$ . Hence, from the (known) ground state values, the cross-sectional area of the excited state follows. Note that, by placing the *gauche* bond at the third-last position (Fig. 3.1C), a shorter projected length is obtained, and so conformation (C) does not belong to the first excited state (even though it has the same energy). The total degeneracy of the first excited state  $D_2 = 4$ , which is the total number of conformations, multiplied by the *gauche* degeneracy of Eq. (3.1). The coarse-graining parameters of the remaining excited states can be found analogously, and are listed for completeness in Table 3.1. Finally, for the completely disordered state  $\alpha = q = 10$ , one assumes  $E_{10} = (0.42M - 3.94) \times 10^{-13}$  erg,  $A_{10} = 34 \text{ \AA}^2$ , and degeneracy  $D_{10} = 6 \times 3^{M-6}$ , which have their origins in experimental considerations [Caillé et al., 1980].

### 3.2.2 Pink model Hamiltonian

Having specified the coarse-graining parameters, the Hamiltonian of the Pink model can be written as [Mouritsen, 1984]

$$\mathcal{H}_{\text{Pink}} = \mathcal{H}_0 + \mathcal{H}_{\text{VDW}} + \mathcal{H}_{\text{P}} \quad . \quad (3.2)$$

The first term is the total internal energy of the acyl chains  $\mathcal{H}_0 = \sum_{i=1}^N E_{s(i)}$ , with the sum over all  $N$  sites of the triangular lattice, and  $s(i) \in \{1, \dots, q\}$  the conformational state at the  $i$ th lattice site. The second term represents the anisotropic van der Waals interaction between adjacent acyl chains  $\mathcal{H}_{\text{VDW}} = -J_0 \sum_{\langle i,j \rangle} I_{s(i)} I_{s(j)}$ , with  $J_0$  the van der Waals coupling constant, and  $\langle i,j \rangle$  a sum over all  $3N$  nearest-neighboring sites on the triangular lattice. The precise value of  $J_0$  depends on the chain length, and explicit expressions are provided elsewhere [Pink et al., 1980a,b; Ipsen et al., 1990]. However, it has been noted that these parameters do not always yield a main transition at the expected temperature [Corvera et al., 1993], and so we will also propose our own values later on. The (dimensionless) variables  $I_\alpha$  measure nematic chain order, and can be expressed in terms of the cross-sectional areas [Caillé et al., 1980; Corvera et al., 1993]:

$$I_\alpha = \omega_\alpha \left( \frac{9}{5} \frac{A_1}{A_\alpha} - \frac{4}{5} \right) \left( \frac{A_1}{A_\alpha} \right)^{5/4} \quad , \quad (3.3)$$

where  $\omega_{10} = 0.4$  for the disordered state  $\alpha = 10$ , and  $\omega_\alpha = 1$  otherwise.

The last term in the Hamiltonian accounts for the interaction between the hydrophilic polar head groups and between them and water and also steric interactions from both head groups and the lipid chains. Although it is possible to consider a more realistic pairwise interaction between the head groups [Mouritsen, 1984], this interaction can be approximated with a simple pressure term  $\mathcal{H}_{\text{P}} = \Pi A$ , where  $\Pi$  is an effective lateral pressure acting on the lipid chains in the bilayer membrane, and  $A$  the total cross-sectional area occupied by the lipids chains,

$$A = \sum_{i=1}^N A_{s(i)} \quad . \quad (3.4)$$

## 3.3 Monte Carlo methods

To study the phase behavior of the Pink model, we use the Monte Carlo (MC) simulation method. We mostly use triangular lattices of size  $N = L \times L$  with periodic boundary

conditions. The principal MC move consists of randomly picking one of the lattice sites, reading out the conformational state  $\alpha$  of that site, and proposing a new state  $\beta$  drawn randomly from the set of  $q$  possible states. The new configuration is accepted with the Metropolis criterion:

$$P_{\text{acc}}(\alpha \rightarrow \beta) = \min \left[ 1, \frac{D_\beta}{D_\alpha} \exp \left( -\frac{\Delta\mathcal{H}}{k_{\text{B}}T} \right) \right] , \quad (3.5)$$

where  $D$  denotes the state degeneracy,  $\Delta\mathcal{H}$  the energy difference between initial and final configuration as given by Eq. (3.2),  $k_{\text{B}}$  the Boltzmann constant, and  $T$  the temperature. The degeneracy compensates for the fact that some of the states have a much larger entropy, and should therefore appear more often in the ensemble average.

By virtue of the MC move, the total projected area  $A$  given by Eq. (3.4) fluctuates during the course of the simulation. In fact,  $A$  plays the role of order parameter since it changes abruptly at the main phase transition. Hence, it is instructive to measure the distribution  $P(A|T, \Pi)$ , defined as the probability of observing a configuration with projected area  $A$ . The distribution depends on the imposed temperature and pressure, as well as on the linear extension  $L$  of the triangular simulation lattice. At the main transition,  $P(A|T, \Pi)$  assumes a characteristic bimodal shape, from which a number of important phase properties are obtained (explicit examples are provided in the next section). We note that even with very long simulation runs, distributions  $P(A|T, \Pi)$  of high statistical quality are difficult to obtain, especially in the vicinity of the main transition. The reason is related to free energy barriers that arise from the formation of interfaces [Binder, 1982; Neuhaus and Hager, 2003; Fischer and Vink, 2010]. To overcome this problem, we combine our MC simulations with a biased sampling scheme called successive umbrella sampling [Virnau and Müller, 2004]; the latter ensures that  $P(A|T, \Pi)$  is sampled accurately over the entire (specified) range in  $A$  of interest. A final ingredient to economize simulation time is the use of histogram reweighting [Ferrenberg and Swendsen, 1989]. A single simulation run yields  $P(A|T, \Pi)$  at a given temperature  $T$  and effective pressure  $\Pi$ ; histogram reweighting enables us to extrapolate the measured distribution to different values  $T', \Pi'$ . For example, extrapolations in the pressure are performed using  $P(A|T, \Pi') \propto P(A|T, \Pi) e^{-(\Pi' - \Pi)A/k_{\text{B}}T}$ . Extrapolations in the temperature can be performed analogously, but also require storage of the energy histograms; for implementation details see Fischer and Vink [2009].

## 3.4 Results

### 3.4.1 The “standard” Pink model revisited

We first consider the main transition in a membrane consisting of DPPC lipids to settle a controversy when this system is being simulated using the Pink model. The acyl chains in DPPC consist of  $M = 16$  carbon atoms, and the experimentally obtained main transition temperature  $T_{\text{DPPC}} = 314.0$  K [Ipsen et al., 1990]. However, simulations based on the Pink model could not detect a transition at this temperature [Corvera et al., 1993]. The latter simulations used the “standard” Pink parameters as listed in Table 3.1, van der Waals coupling constant  $J_0 = 0.710 \times 10^{-13}$  erg, and pressure  $\Pi = 30$  dyn/cm. Hence the question arises as to why no transition could be detected. To answer this question we perform additional DPPC simulations using the Pink model, with the same parameters as in Corvera et al. [1993], but over a wider range in temperature and pressure. The picture that emerges is the following: At high temperature the distribution  $P(A|T, \Pi)$  is always single-peaked (corresponding to one-phase) for all value of the lateral pressure  $\Pi$ . At low temperature,  $P(A|T, \Pi)$  is double-peaked for a special value of the lateral pressure,  $\Pi = \Pi_{\text{COEX}}$ , corresponding to two-phase coexistence (Fig. 3.2A). Here, the left peak reflects the *gel* phase, the right peak the *fluid* phase. The numerical criterion to locate  $\Pi_{\text{COEX}}$  is to vary  $\Pi$  until the fluctuation  $\langle A^2 \rangle - \langle A \rangle^2$  reaches a maximum [Orkoulas et al., 2001], with the thermal averages computed as  $\langle A^m \rangle = \int A^m P(A|T, \Pi) dA$ .

At the temperature  $T = T_c$  where the transition from a single- to double-peaked distribution occurs, the system becomes critical. To locate the critical temperature a finite-size scaling analysis is performed, whereby we plot the Binder cumulant  $U_1 = \langle \Delta^2 \rangle / \langle |\Delta| \rangle^2$ ,  $\Delta \equiv A - \langle A \rangle$ , versus temperature  $T$  for different system sizes  $L$ . In the thermodynamic limit,

$$\lim_{L \rightarrow \infty} U_1 = \begin{cases} 1 & T < T_c, \\ U_1^* & T = T_c, \\ \pi/2 & T > T_c, \end{cases} \quad (3.6)$$

while in systems of finite size, curves for different  $L$  intersect at  $T = T_c$  [Binder, 1981a,b]. In Fig. 3.2B, we show the result for DPPC obtained using the “standard” Pink model parameters: The data scale is as expected, and from the intersection the critical temperature  $T_c$  can be accurately “read off”.



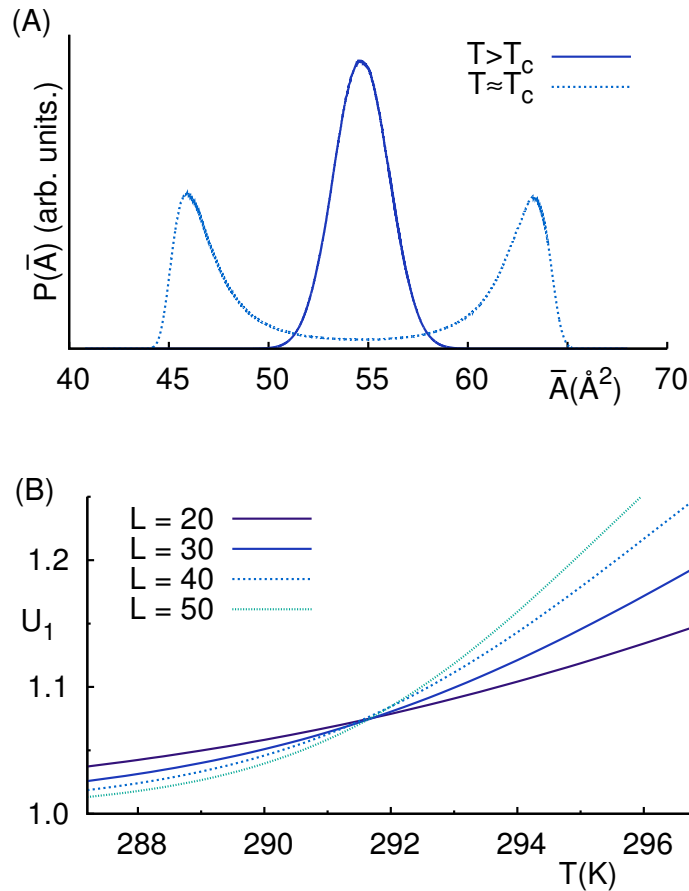


**Figure 3.2:** Simulation results for DPPC obtained using the Pink model with “standard” parameters. **(A)** Probability distribution  $P(\bar{A})$  of the cross-sectional area per molecule. Note that we have adopted the convention to plot the average area per lipid,  $\bar{A} = 2A/N$ , with  $A$  given by Eq. (3.4). At high temperature, irrespective of the value of  $\Pi$ ,  $P(\bar{A})$  is single-peaked corresponding to one-phase (solid line). At low temperature,  $P(\bar{A})$  becomes double-peaked provided  $\Pi = \Pi_{\text{COEX}}$ , indicative of two-phase coexistence (dotted line). **(B)** Finite-size scaling analysis to locate the critical temperature  $T_c$ . Plotted is the Binder cumulant  $U_1$  as a function of temperature  $T$  for different system sizes  $L$ . The intersection of the curves for different  $L$  yields  $T_c$ .

	$M$	$J_0$	$T_c$	$\Pi_{\text{COEX}}$	$T_m$	$J_0^*$	$\Pi_{\text{COEX}}^*$
DMPC	14	0.618	270.3	4.3	296.9	0.690	15.6
DPPC	16	0.710	291.7	4.6	314.0	0.772	18.1
DSPC	18	0.815	321.5	21.6	327.9	0.833	26.7

**Table 3.2:** Critical point parameters for three lipid species, with  $M$  the number of carbon atoms in a single chain. We list the critical temperature  $T_c$  and coexisting pressure  $\Pi_{\text{COEX}}$  obtained in simulations of the Pink model using the “standard” value of the van der Waals coupling constant  $J_0$ . The resulting estimates of  $T_c$  are to be compared to the experimental melting temperatures  $T_m$ :  $T_c$  clearly underestimates  $T_m$  in all cases. Instead, by using the Pink model with the re-tuned values  $J_0^*$  proposed in this work,  $T_c$  coincides with  $T_m$ , with corresponding critical pressure  $\Pi_{\text{COEX}}^*$  (coupling constants in units of  $10^{-13}$  erg, temperatures in K, and pressures in dyn/cm).

The corresponding estimates of  $T_c$  as well as the coexistence pressures  $\Pi_{\text{COEX}}$  for three lipid species are collected in Table 3.2. For all lipid species considered, the computed critical temperature  $T_c$  is distinctly below the experimental melting temperature  $T_m$ . In other words, if one simulates the Pink model at the experimental melting temperature  $T_m$ , one is always inside the one-phase region, where  $P(A|T, \Pi)$  is single-peaked! This, apparently, is the reason why no phase transition could be seen in previous studies [Corvera et al., 1993]. One possibility to get the proper value for the transition temperature (i.e., such that  $T_c$  coincides with  $T_m$ ) is to re-tune the value of  $J_0$ . This has been done for the three lipid species by systematically changing the coupling constant  $J_0$  using histogram reweighting and finite-size scaling. Our proposed values  $J_0^*$  and corresponding pressures  $\Pi_{\text{COEX}}^*$  for the three lipid species are summarized in Table 3.2.

For completeness, we still confirm the universality class of the critical point, which for the Pink model is expected to be the one of the 2D Ising model [Pink et al., 1980a]. To this end, we consider the susceptibility  $\chi = (\langle \Delta^2 \rangle - \langle |\Delta| \rangle^2) / (k_B T L^2)$  [Orkoulas et al., 2000], which diverges at the critical point  $\chi \propto |t|^{-\gamma}$ ,  $t = T/T_c - 1$ , with critical exponent  $\gamma$ . In systems of finite size, the divergence is rounded, but  $\gamma$  can still be obtained using the standard finite-size scaling procedure of plotting  $\chi L^{-\gamma/\nu}$  versus  $t L^{1/\nu}$  [Newman and Barkema, 1999], where  $\nu$  is the correlation length critical exponent. Provided suitable values  $\gamma, \nu, T_c$  are used, data for different  $L$  collapse. The result for DPPC is shown in Fig. 3.3, where the “standard” parameters of the Pink model were used. Indeed, by using the 2D Ising values  $\{\gamma = 7/4, \nu = 1\}$ , and  $T_c = 291.7$  K of Table 3.2, an excellent data collapse is observed (similar good collapses are obtained for DMPC and DSPC

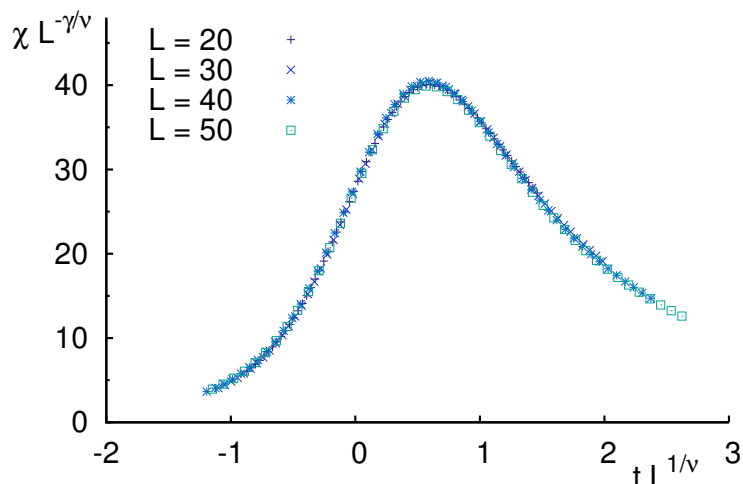


**Figure 3.3:** Susceptibility scaling function  $\chi L^{-\gamma/\nu}$  versus  $t L^{1/\nu}$  for DPPC obtained using the “standard” Pink model. The data for different system sizes strikingly collapse using 2D Ising values for the critical exponents.

also). The order parameter critical exponent has also been measured, and the 2D Ising value  $\beta = 1/8$  was confirmed (scaling plot not shown). Therefore, even though the Pink model is a 10-state model, its critical behavior remains in the universality class of the 2D Ising model. This further motivates the idea of reducing the  $q = 10$  states in the Pink model to an effectively two-state description as is frequently done [Doniach, 1978; Pink et al., 1980a; Mouritsen et al., 1983; Michonova-Alexova and Sugár, 2002; Ehrig et al., 2011b].

### 3.4.2 Modified Pink model with fewer states

We now consider the effect of lowering the number of states in the Pink model. For this purpose, an appropriate number of intermediate states was removed, based on the maximum number of *gauche* bonds. In the “standard” 10-state Pink model at most three *gauche* bonds are allowed. We now consider the case where at most two *gauche* bonds are permitted, by removing states  $\alpha = 8, 9$  from Table 3.1, yielding an 8-state model (to keep the total number of states constant the degeneracy of the removed states was added to the disordered state, but we emphasize that this correction is small). We apply our previous finite-size scaling analysis to the resulting 8-state model for DPPC, using the “standard” value  $J_0 = 0.710 \times 10^{-13}$  erg. As expected, the critical point remains in the universality class of the 2D Ising model, but it is “shifted” to  $T_c = 309.4$  K and  $\Pi_{\text{COEX}} = 26.0$  dyn/cm. Similarly, by allowing at most one *gauche* bond, a 5-state

model is obtained. In this case, the DPPC critical point is located at  $T_c = 351.5$  K and  $\Pi_{\text{COEX}} = 87.7$  dyn/cm.

Therefore, lowering the number of states in the Pink model while leaving the other parameters untouched, one finds that both the critical temperature and pressure increase. This trend is consistent with the Pink model simulations of Mouritsen [1983] for DPPC performed at the experimental melting temperature  $T_m$  but with a lower number of states. In these simulations, hysteresis loops indicating a first-order transition are clearly visible around  $T_m$  for  $q < 6$ . Indeed, as our scaling analysis shows, by lowering the number of states  $q$ ,  $T_c$  eventually exceeds  $T_m$ , resulting in a genuine phase transition at  $T_m$ .

To conclude, lowering the number of states  $q$  does not affect the universality class of the Pink model, which remains 2D Ising (provided  $q \geq 2$ , of course). Hence, the topology of the phase diagram remains the same; merely the critical point gets shifted. Depending on the parameters used, the main transition in the Pink model is either first-order ( $T < T_c$ ), or it is 2D Ising critical ( $T = T_c$ ). We do not claim that the main transition as observed in experiments necessarily conforms to this scenario (we return to this point in Section 3.5).

### 3.4.3 Pink model with quenched disorder

As a final illustration, we consider the main transition in a solid-supported membrane, which has received considerable attention in experiments [Yang and Appleyard, 2000; Xie et al., 2002; Tokumasu et al., 2003; Charrier and Thibaudau, 2005; Keller et al., 2005; Seeger et al., 2010]. A striking feature observed in one of these studies is the formation of coexisting gel and fluid domains that do not coalesce with time, but instead form a multi-domain structure that is stable over hours [Charrier and Thibaudau, 2005]. To understand the stability of this structure is not trivial, due to the large amount of line interface it contains. Here we attempt to reproduce such a multi-domain structure within the framework of the Pink model. Our hypothesis is that the solid support onto which the membrane is deposited has a certain roughness. Since surface roughness is random and time independent, it constitutes a form of quenched disorder. We assume that this gives rise to regions on the surface where certain lipid tail conformations are preferred over others. We capture this effect in the Pink model by randomly labeling a fraction  $p$  of the lattice sites as “pinning sites”. At the pinning sites, the corresponding lipid chain is fixed into the ground state conformation. This extension is trivially incorporated

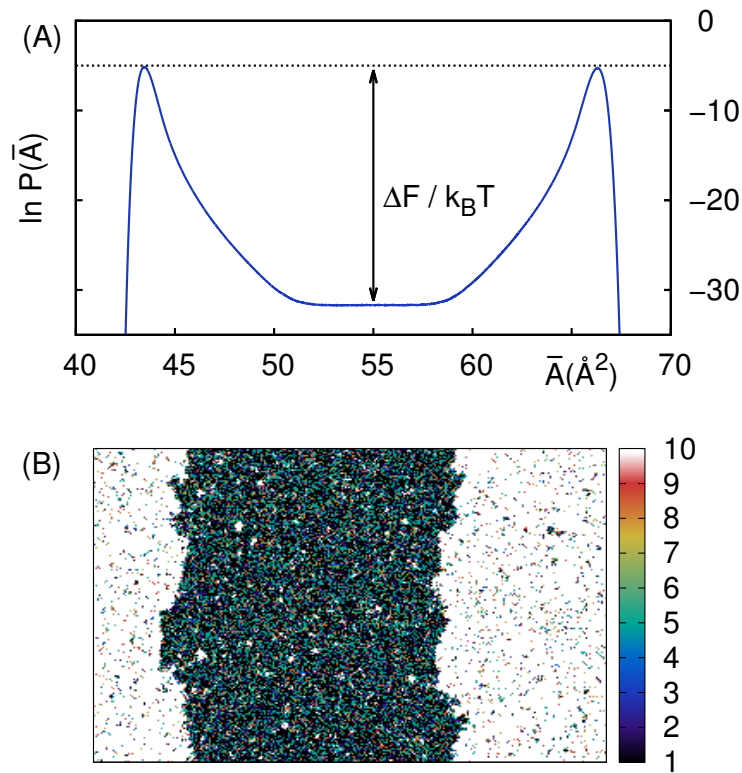


**Figure 3.4:** DSPC simulation results for  $T = 291$  K in the absence of quenched disorder. **(A)** The natural logarithm of  $P(\bar{A})$  at  $\Pi_{\text{COEX}}$  and system size  $L = 50$ . The barrier  $\Delta F$  is related to the line tension via Eq. (3.7). **(B)** Typical snapshot of the bilayer with the lipids color coded according to their conformational state for a  $200 \times 300$  lattice. The snapshot was taken at cross-sectional area  $\bar{A} = 54.4 \text{\AA}^2$  chosen “between the peaks” of  $P(\bar{A})$ . A pronounced coexistence between a single gel and fluid domain is observed.

into our MC simulations: We simply do not apply the MC move to pinning sites. We specialize to DSPC, using the “standard” Pink parameters of Tables 3.1 and 3.2.

In Fig. 3.4A, we show  $\ln P(A|T, \Pi)$  at  $T = 291$  K and  $\Pi_{\text{COEX}} = -18.9$  dyn/cm in the absence of quenched disorder ( $p = 0$ ). At this temperature, which is well below  $T_c$ , the main transition is strongly first-order. Consequently, there is a significant line tension  $\sigma$  between gel and fluid domains; the latter is related to the free energy barrier [Binder, 1982; Billoire et al., 1994]:

$$\Delta F \equiv k_B T \ln(P_{\text{max}}/P_{\text{min}}) = 2\sigma L \quad , \quad (3.7)$$

indicated by the vertical double arrow in Fig. 3.4A. Here,  $P_{\text{min}}$  is the value of  $P(A|T, \Pi)$  at the minimum “between the peaks”, while  $P_{\text{max}}$  denotes the average peak value. The

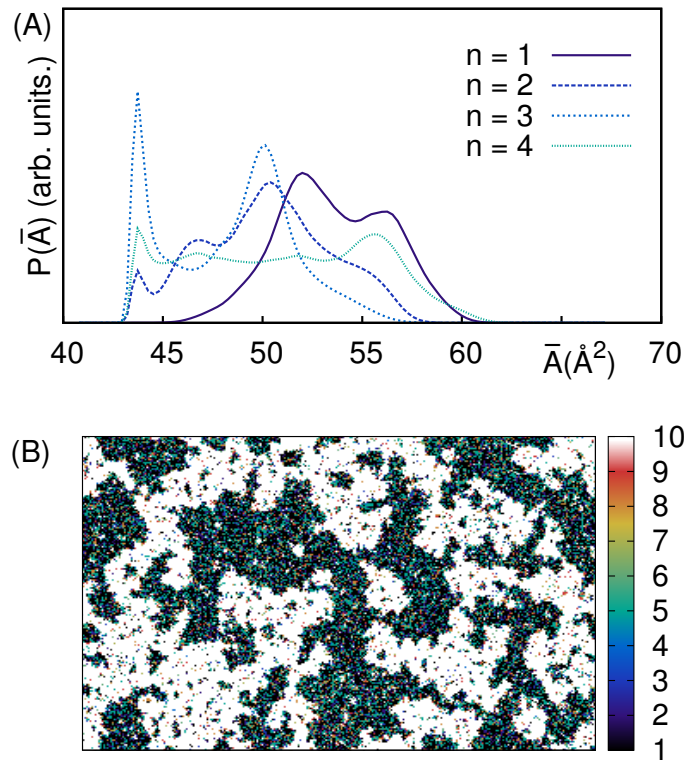


**Figure 3.5:** DSPC simulation results for  $T = 291$  K in the presence quenched disorder, with a fraction of pinning sites  $p = 0.03$ . **(A)** Typical distributions  $P(\bar{A})$  for four different samples of pinning sites, and system size  $L = 50$ . In contrast to Fig. 3.4A, a first-order transition can no longer be identified. **(B)** Typical bilayer snapshot obtained at  $\bar{A} = 54.4 \text{ \AA}^2$  for a  $200 \times 300$  lattice. A stable structure of multi-domains is observed.

physical motivation for Eq. (3.7) is that, for cross-sectional areas “between the peaks”, the bilayer reveals a coexistence between two slab domains where the total interface length equals  $2L$  (Fig. 3.4B). For DSPC, and assuming the lattice constant to be 1 nm, we obtain  $\sigma \sim 1.1$  pN, which is compatible with experimental values [Karatekin et al., 2003].

Next, we consider a DSPC bilayer with a fraction  $p = 0.03$  of the lattice sites marked as “pinning sites”. In Fig. 3.5A, we show distributions  $P(A|T, \Pi)$  for  $T = 291$  K obtained for four different random positions (samples) of pinning sites. Even though the temperature is the same as in Fig. 3.4A, a unique double-peaked distribution can no longer be identified. In contrast,  $P(A|T, \Pi)$  is strongly sample dependent, and a multitude of rather exotic shapes is revealed. This behavior is characteristic of systems that belong to the universality class of the 2D random-field Ising model (2D-RFIM) [Fischer and Vink,

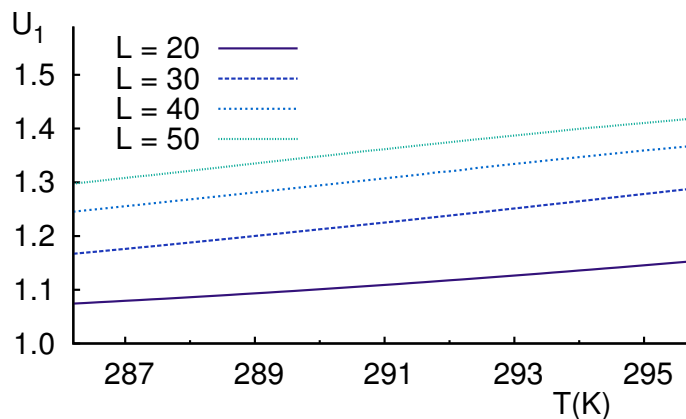


**Figure 3.6:** The (disorder-averaged) Binder cumulant  $U_1$  as a function of temperature  $T$  for DSPC with a fraction  $p = 0.03$  of pinning sites. In contrast to Fig. 3.2B, an intersection of the curves for different  $L$  can no longer be identified. Instead, as the system size  $L$  increases,  $U_1 \rightarrow \pi/2$ , indicative of the one-phase region. For each system size, the disorder average comprised 200 samples of pinning sites.

2011]. Hence, by introducing the pinning sites, we have changed the universality class of the Pink model from ordinary 2D Ising toward 2D-RFIM (the pinning sites essentially correspond to a field of infinite strength acting at random locations).

There are two features of the 2D-RFIM universality class that are remarkably consistent with experimental results for the main transition in supported membranes. First of all, 2D-RFIM universality implies the absence of macroscopic coexistence between gel and fluid domains [Imry and Ma, 1975; Imbrie, 1984; Bricmont and Kupiainen, 1987; Aizenman and Wehr, 1989]. Indeed, inspection of simulation snapshots (Fig. 3.5B) reveals an equilibrium multi-domain structure, that is highly anisotropic, strongly resembling experimental AFM images [Charrier and Thibaudau, 2005]. A second (related) feature is that the 2D-RFIM has no true phase transition in the thermodynamic limit. In finite systems, there may be signs of a transition [or even several transitions; note that some of the distributions in Fig. 3.5A are triple-peaked], but they will be “smeared” over a wide temperature range, and do not persist in the thermodynamic limit. Precisely this behavior has also been reported in experiments [Tokumasu et al., 2003; Charrier and Thibaudau, 2005]. Simulation evidence that the pinning sites prevent a sharp transition in the thermodynamic limit follows from the (disorder-averaged) Binder cumulant  $U_1 = [\langle \Delta^2 \rangle] / [\langle |\Delta| \rangle^2]$ , where  $[\cdot]$  denotes an average over different samples of pinning

sites. As shown in Fig. 3.6,  $U_1 \rightarrow \pi/2$  as  $L$  increases, consistent with only a single phase.

### 3.5 Conclusion

In this paper, the main phase transition in single-component phospholipid membranes was investigated using the Pink model. Our simulations of the pure membrane (i.e., without quenched disorder) confirm the formation of macroscopic gel and fluid domains below a critical temperature  $T_c$ , and at the coexistence pressure  $\Pi_{\text{COEX}}$ . We also demonstrated that, using the accepted values of the Pink model parameters,  $T_c$  falls below experimentally measured transition temperatures. This explains why no phase transition was detected at the experimental transition temperature in the simulations of [Corvera et al. \[1993\]](#). To resolve this issue, we propose that the strength of the van der Waals coupling in the Pink model be increased. By using the values proposed in this work,  $T_c$  of the Pink model *in the thermodynamic limit* coincides with the experimental main transition temperature. In addition, finite-size scaling was applied to confirm the universality class of the critical point in the Pink model, which was shown to be 2D Ising. This result holds irrespective of the number of conformational states  $q$  (as long as  $q \geq 2$ , of course). Hence, to capture the generic features of membrane phase behavior, a highly detailed model is not always needed (which is consistent with the findings of [Fischer et al. \[2012\]](#)).

We have also used the Pink model to describe the main transition in the presence of quenched disorder, which may arise in case the membrane is deposited on a rough support. Assuming that this induces regions in the membrane where certain tail conformations become preferred, the universality class changes toward that of the 2D *random-field* Ising model. In the presence of quenched disorder, the Pink model reveals a stable multi-domain structure, and the absence of a sharp transition; these findings are indeed consistent with some of the experimental observations.

Although the Pink model (both the pure version and the one containing quenched disorder) seems well suited to describe the main transition, we wish to end with a warning. By using the Pink model, one inevitably casts the main transition into the Ising universality class. This may not be entirely appropriate, as the main transition is essentially a melting transition leading to the formation of nematic chain order. A liquid-crystal model may therefore be more suitable, such as the Maier-Saupe approach followed in [Marčelja \[1973\]](#). If, indeed, the main transition occurs close to a critical point [[Marčelja,](#)



1974; Doniach, 1978] it may well be necessary to replace the discrete set of states of the Pink model by a continuous one [Scoville-Simonds and Schick, 2003]. In that case, one enters the regime of Heisenberg-type models (which, provided certain conditions are met, do support 2D phase transitions [van Enter and Shlosman, 2002; Blöte et al., 2002; Fish and Vink, 2009]). The investigation of the main transition in terms of such a continuous model could be an interesting topic for future work.

## Acknowledgments

This work was supported by the *Deutsche Forschungsgemeinschaft* (Emmy Noether VI 483 and the SFB-937).

## Chapter 4

# Raft formation in lipid bilayers coupled to curvature

Sina Sadeghi, Marcus Müller, and Richard L. C. Vink (2014)

Biophysical Journal, 107(7):1591

Published 7 October 2014

DOI: [10.1016/j.bpj.2014.07.072](https://doi.org/10.1016/j.bpj.2014.07.072)

The manuscript describes a study of phase transition in lipid membranes coupled to height deformations. The study was designed by Richard Vink and me. We set up the model and the simulation method. I performed all simulations (including from-scratch code writing), and data acquisition. I performed data analysis and interpretation together with Richard Vink and Marcus Müller. The manuscript was written by me with revisions from Richard Vink.

## Abstract

We present computer simulations of a membrane in which the local composition is coupled to the local membrane curvature. At high temperatures (i.e., above the temperature of macroscopic phase separation), finite-sized transient domains are observed, reminiscent of lipid rafts. The domain size is in the range of hundred nanometers, and set by the membrane elastic properties. These findings are in line with the notion of the membrane as a curvature-induced microemulsion. At low temperature, the membrane phase separates. The transition to the phase-separated regime is continuous and belongs to the two-dimensional Ising universality class when the coupling to curvature is weak, but becomes first-order for strong curvature-composition coupling.

## 4.1 Introduction

Ever since the postulation of the lipid raft hypothesis [Simons and Ikonen, 1997], understanding the lateral structure and heterogeneity of lipid bilayers has been an extremely active area of research. One line of thought is that lipid rafts (i.e., tiny domains rich in saturated lipids and cholesterol floating in an ocean of unsaturated lipids) are the result of two-phase fluid-fluid coexistence. The challenge is to explain why raft domains remain small, as opposed to growing and coalescing in order to minimize line tension [Lenne and Nicolas, 2009; Komura and Andelman, 2014]. One hypothesis is that membranes are close to (but distinctly above, i.e., in the one-phase region of the phase diagram) the critical point of the fluid-fluid coexistence region. Hence, the correlation length is still large (i.e., significantly exceeding the size of single molecules) but macroscopic domain formation does not occur. Experiments performed on model membranes indeed reveal that such systems support critical behavior [Veatch et al., 2007, 2008; Connell et al., 2013], with indications that the corresponding universality class is the expected one [Honerkamp-Smith et al., 2008] (i.e., the one of the two-dimensional (2D) Ising model).

Although the existence of critical behavior in free-standing membranes has thus been demonstrated quite convincingly (not only in model membranes, but also in cell-derived vesicles [Veatch et al., 2008; Levental et al., 2009]), the relevance of this for real cell membranes is not entirely obvious, because the latter are typically not free, but intricately connected to their environment (for instance to the cytoskeleton). Relatively recent simulations have shown that, in the presence of a cytoskeleton network, macroscopic

domain formation will always be suppressed [Fischer and Vink, 2011; Machta et al., 2011; Ehrig et al., 2011a; Fischer et al., 2012]. The idea is that, assuming the cytoskeleton network to be spatially random on large scales and with a preferred affinity to one of the lipid species, a new universality class is induced, namely the one of the two-dimensional random-field Ising model. As is well known [Imry and Ma, 1975], the latter model does not support macroscopic domain formation at any temperature nor does it support critical behavior, and so it is not a priori obvious how the critical behavior observed in free-standing vesicles would manifest itself in the presence of a cytoskeleton network. The suppression of macroscopic lipid phase separation was recently confirmed experimentally in a model membrane coupled to an actin network [Honigsmann et al., 2014]. In yeast cells, the situation is less clear [Spira et al., 2012].

In yet another view [Yamamoto and Safran, 2011; Palmieri and Safran, 2013], applicable to both free-standing and non-free membranes, the working hypothesis is that the line tension is effectively lowered by hybrid lipids; the latter collect at the raft interface, thereby lowering the line tension in much the same way a surfactant molecule would. In the presence of hybrid lipids, the tendency of the membrane to phase separate would thus be greatly diminished, offering an alternative explanation for the stability of lipid rafts.

Finally, the last hypothesis that we mention here is that rafts may be stabilized via a coupling between the local membrane composition and the local shape (e.g., curvature, thickness) of the membrane leaflet [Schick, 2012; Meinhardt et al., 2013; Shlomovitz and Schick, 2013]. For instance, it may be that regions of certain curvature sign prefer certain lipid species (the feasibility of such a coupling has been demonstrated experimentally [Parthasarathy et al., 2006; Parthasarathy and Groves, 2007]). This hypothesis differs from the others discussed above, because it departs from the view that the membrane is strictly flat and two-dimensional. Instead, the membrane height deviations into the third dimension now play a crucial role.

The existence of the various hypotheses (i.e., critical behavior, cytoskeleton arrested phase separation, hybrid lipids, coupling to membrane leaflet shape) precludes a comprehensive picture of exactly what goes on in membrane raft formation. Presumably, all proposed mechanisms contribute to some extent. With this idea in mind, the purpose of this article is to investigate by computer simulation how membrane fluid-fluid demixing is affected by a coupling to the membrane leaflet shape. We thus focus on the combined effect of the first and last discussed hypothesis (leaving aside therefore the role of hybrid lipids and the cytoskeleton). Our foremost aim is to test the recent hypothesis of Schick

in which the membrane is envisioned as a curvature-induced microemulsion [Schick, 2012]. This hypothesis is interesting for biological applications because it accounts for transient domains of finite size (i.e., rafts) at physiological temperatures, without requiring the vicinity of a critical point. Our second aim is to consider the fate of phase separation transitions in membranes that are coupled to curvature.

The outline of this article is as follows: We first recapitulate the essentials of Schick's hypothesis. Next, we introduce our membrane model, and describe how this model is simulated using Monte Carlo updates in Fourier space. Our results, including a careful analysis of finite-size effects, are presented, and then we give our conclusions.

## 4.2 Theoretical Background

We consider a lipid bilayer that undergoes lateral phase separation into a liquid-ordered (Lo) and liquid-disordered (Ld) phase. The Lo phase is characterized by a high density of saturated lipids and cholesterol, whereas the Ld phase has a high density of unsaturated lipids [Veatch and Keller, 2003; Veatch et al., 2008]. We assume the membrane to be planar, such that the local membrane height  $h$ , and the local composition  $\phi$ , may be expressed as functions of the lateral coordinates  $x, y$  (Monge representation). The scalar field  $\phi \equiv \phi(x, y)$  describes the local composition of, say, the upper leaflet, with the sign encoding whether the position at  $(x, y)$  is predominantly Lo or Ld. The free energy cost of the membrane height fluctuations is given by the Helfrich form [Helfrich, 1973], which regards the membrane as an elastic sheet with bending rigidity  $\kappa$ , and surface tension  $\sigma$ , as

$$\mathcal{H}_{\text{Helfrich}} = \int \left[ \frac{\kappa}{2} (\nabla^2 h)^2 + \frac{\sigma}{2} (\nabla h)^2 \right] dx dy \quad . \quad (4.1)$$

The free energy cost of the composition fluctuations is described by a fourth-order Landau expansion

$$\mathcal{H}_{\text{Composition}} = \int \left[ \frac{A}{2} \phi^2 + \frac{B}{2} (\nabla \phi)^2 + C \phi^4 \right] dx dy \quad . \quad (4.2)$$

The molecular asymmetry between the Lo and Ld phases gives rise to a curvature-composition coupling term [Parthasarathy et al., 2006; Parthasarathy and Groves, 2007]

$$\mathcal{H}_x = \gamma \int \phi (\nabla^2 h) dx dy \quad , \quad (4.3)$$

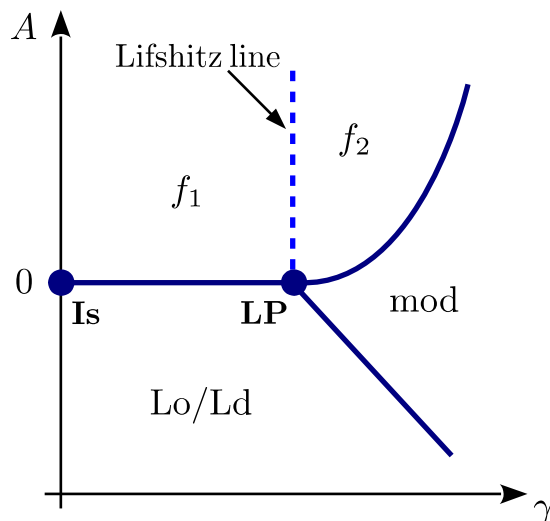


**Figure 4.1:** Topology of the mean-field phase diagram of Eq. (4.4). The horizontal axis is the strength  $\gamma$  of the curvature-composition coupling, the vertical axis is the prefactor  $A$  of the quadratic term in Eq. (4.2). There are four distinct thermodynamic phases: a disordered fluid phase spanning the regions  $f_1$  and  $f_2$ ; the Lo phase and the Ld phase; and a modulated phase (mod). (*Solid lines*) Genuine phase transitions; (*dashed line*) Lifshitz line. In mean-field theory, all lines meet in the Lifshitz point (LP). The point Is marks the critical point of the system without curvature-composition coupling.

with coupling strength  $\gamma$ . This coupling implies that the composition of the lower leaflet will be anti-correlated. More refined descriptions allowing for a positive correlation are presented elsewhere [Shlomovitz and Schick, 2013; Meinhardt et al., 2013], but here we focus on the most simple case. The full model is the sum of the above three Hamiltonian terms

$$\mathcal{H}^{\text{Theory}} = \mathcal{H}_{\text{Helfrich}} + \mathcal{H}_{\text{Composition}} + \mathcal{H}_x \quad . \quad (4.4)$$

Models such as Eq. (4.4) have been intensely studied [Leibler and Andelman, 1987; Andelman et al., 1992; Hansen et al., 1998; Kumar et al., 1999; Gozdz and Gompper, 2001; Harden et al., 2005], and the corresponding mean-field phase diagram, depicted in Fig. 4.1, is well known [MacKintosh, 1994; Shlomovitz and Schick, 2013]. A two-dimensional representation is used, in which the horizontal axis denotes the strength  $\gamma$  of the curvature-composition coupling, and the vertical axis denotes the coefficient  $A$  of the quadratic term in the Landau expansion, Eq. (4.2). There are four distinct thermodynamic phases: The first one is a fluid phase, indicated by regions  $f_1$  and  $f_2$ , which is a disordered phase characterized by exponentially decaying correlations. This phase occurs for  $A > 0$  and small values of  $\gamma$ . The difference between regions  $f_1$  and  $f_2$  is that the structure factor  $S(q)$  assumes its maximum at wave vector  $q = 0$  in  $f_1$ , and

at  $q = q^* > 0$  in  $f_2$ . We emphasize that no phase transition is associated by crossing the Lifshitz line that separates regions  $f_1$  and  $f_2$ . Thermodynamically, the entire region,  $f_1$  and  $f_2$ , is a single phase. For  $A < 0$  and small  $\gamma$ , the membrane macroscopically phase separates into two coexisting phases, i.e., the Lo and Ld phases.  $A$  may thus be regarded as the temperature difference from the critical temperature of phase separation. At large  $\gamma$ , the fourth phase is observed. This is a modulated phase characterized by alternating stripes in the composition, of some characteristic wavelength.

In mean-field theory, all lines meet at the Lifshitz point (LP), located at  $A = 0$  and  $\gamma = \gamma_{\text{Lif}}$ . In the absence of curvature-composition coupling,  $\gamma = 0$ , one recovers conventional fluid phase separation (the experimental analysis of phase separation in vesicles is typically performed this way [Honerkamp-Smith et al., 2008]). In this case, there is a critical point (Is) below which the homogeneous fluid membrane macroscopically phase separates into coexisting Lo and Ld phases. In a real membrane (accounting for fluctuations), this critical point is expected to belong to the 2D Ising universality class. In the presence of curvature-composition coupling,  $\gamma > 0$ , the point Is marks the beginning of a line of critical points, which extends to the Lifshitz point. In mean-field theory, phase transitions between  $f_1 \leftrightarrow \text{Lo/Ld}$  and  $f_2 \leftrightarrow \text{mod}$  are continuous, whereas transitions  $\text{Lo/Ld} \leftrightarrow \text{mod}$  are first-order.

To account for lipid rafts, i.e., composition fluctuations on a length scale that is large compared to single particles yet not macroscopic, Fig. 4.1 offers two possible candidates. The first is to tune the membrane close to the critical point of phase separation, i.e., just above the line “Is-LP”. Provided  $A > 0$ , the membrane remains mixed, but with large composition fluctuations characteristic of a critical point [Veatch et al., 2007; Connell et al., 2013]. The second possibility, proposed by Schick [Schick, 2012], is the fluid region  $f_2$ . Because the latter is above the Lifshitz line, composition fluctuations on a non-trivial scale corresponding to wave vector  $q^*$  are expected. To quantify this scale, one can ignore the quartic term in the Landau expansion ( $C = 0$ ), because in region  $f_2$  the coefficient  $A > 0$ . In terms of the Fourier components of the composition field  $\tilde{\phi}(\vec{q})$ , and after integrating out the height fluctuations, the free energy becomes [Schick, 2012]

$$\mathcal{F} = \frac{1}{2} \int \frac{|\tilde{\phi}(\vec{q})|^2}{S(q)} d\vec{q}, \quad q = |\vec{q}| \quad , \quad (4.5)$$

with the integration over all two-dimensional wave vectors,  $\vec{q}$ . Here  $S(q)$  denotes the static structure factor of composition fluctuations

$$\frac{1}{S(q)} = A + Bq^2 - \frac{\gamma^2}{\kappa + \sigma/q^2} \quad . \quad (4.6)$$

For  $\gamma \rightarrow 0$ ,  $S(q)$  approaches the Ornstein-Zernike form, which reaches its maximum at wave vector  $q = 0$ , indicating macroscopic composition fluctuations. For  $\gamma > \gamma_{\text{Lif}} = \sqrt{\sigma B}$ , the structure factor,  $S(q)$ , assumes its maximum at a finite wave vector

$$q^* = \sqrt{(\sigma/\kappa)(\gamma/\gamma_{\text{Lif}} - 1)} \quad , \quad (4.7)$$

and so  $\gamma_{\text{Lif}}$  marks the Lifshitz line (*vertical dashed line* in Fig. 4.1). The corresponding (inverse) value of the structure factor reads as

$$\frac{1}{S(q^*)} = A \left( 1 - \frac{(\gamma - \gamma_{\text{Lif}})^2}{A\kappa} \right) \quad , \quad (4.8)$$

which becomes zero at  $\gamma_{\text{m}} = \gamma_{\text{Lif}} + \sqrt{A\kappa}$  (the phase boundary  $f_2 \leftrightarrow \text{mod}$  is thus parabolic).

For  $\gamma_{\text{Lif}} < \gamma < \gamma_{\text{m}}$  (region  $f_2$ ), i.e., between the Lifshitz line and the modulated phase, the system resembles a microemulsion. That is, the membrane is overall disordered, but with composition fluctuations on a non-trivial length scale set by the wave vector  $q^*$ . As noted by Schick [2012], this is promising in view of rafts, which are postulated to be transient domains of finite size. To obtain the actual length, one Fourier transforms  $S(q)$ , which in two dimensions corresponds to a Hankel transform. The result from Schick [2012] is a characteristic size of the composition fluctuations  $\sim (\kappa/\sigma)^{1/2}$ . For typical values of the bending rigidity and tension, this size is  $\sim 100$  nm, which is compatible with the raft scale.

### 4.3 Simulation Model

Our simulation model is a discretized version of Eq. (4.4). It is defined on a  $L \times L$  periodic square lattice, each lattice site having a spatial coordinate  $(i, j)$ . To describe the membrane composition, we assign a spin variable  $s_{i,j} = \pm 1$  to each cell, where the sign indicates whether the cell  $(i, j)$  is predominantly Lo or Ld. To incorporate the membrane height fluctuations, we also assign to each cell a real number  $h_{i,j} \in \mathbb{R}$  describing the membrane height at cell  $(i, j)$  measured with respect to a flat reference



plane. Without loss of generality, the reference height is placed at zero in what follows. The total free energy of our simulation model is given analogously to Eq. (4.4) as

$$\mathcal{H}^{\text{Sim}} = \mathcal{H}_{\text{Helfrich}}^{\text{Sim}} + \mathcal{H}_{\text{Composition}}^{\text{Sim}} + \mathcal{H}_{\text{x}}^{\text{Sim}} \quad . \quad (4.9)$$

The first term describes the elastic energy of the membrane height fluctuations, for which we again use the Helfrich expansion [Helfrich, 1973]

$$\mathcal{H}_{\text{Helfrich}}^{\text{Sim}} = \sum_{(i,j)} \frac{a^2}{2} \left[ \kappa (\nabla^2 h_{i,j})^2 + \sigma |\nabla h_{i,j}|^2 \right] \quad , \quad (4.10)$$

where  $a$  is the lattice spacing, and the sum is over all lattice sites:  $\sum_{(i,j)} \equiv \sum_{i=0}^{L-1} \sum_{j=0}^{L-1}$ . The first term in Eq. (4.10) is the bending energy, and its strength is set by the bending modulus,  $\kappa$ . The latter term describes the free energy of membrane area deformations, and its scale is dictated by the membrane tension,  $\sigma$ . Note that Eq. (4.10) is given in discrete form, as is appropriate for a lattice model. To compute the gradient and Laplacian terms, we use the finite-difference expressions

$$\begin{aligned} \nabla h_{i,j} &\equiv \frac{1}{2a} \begin{pmatrix} h_{i+1,j} - h_{i-1,j} \\ h_{i,j+1} - h_{i,j-1} \end{pmatrix} \quad , \\ \nabla^2 h_{i,j} &\equiv \frac{1}{a^2} (h_{i+1,j} + h_{i-1,j} + h_{i,j+1} + h_{i,j-1} - 4h_{i,j}) \quad , \end{aligned} \quad (4.11)$$

as is commonly done in simulations [Weigl et al., 2002]. In the limit  $a \rightarrow 0$ , these finite-difference expressions exactly converge to their continuous counterparts; for finite  $a$ , however, some lattice artifacts may be present (e.g., square anisotropy). The second term models the lipid interactions, which we assume to be pairwise-additive, and are given by a simple Ising term

$$\mathcal{H}_{\text{Composition}}^{\text{Sim}} = -J \sum_{(i,j)} s_{i,j} (s_{i+1,j} + s_{i,j+1}) \quad , \quad (4.12)$$

where  $J > 0$  is the Ising interaction constant. This is following the approach of Honerkamp-Smith et al. [2008], which also use the Ising model to describe phase-separating vesicles, but without curvature coupling. The last term in the free energy describes the coupling of the local composition to the local membrane curvature, given in discrete form as

$$\mathcal{H}_{\text{x}}^{\text{Sim}} = \gamma \sum_{(i,j)} a^2 s_{i,j} (\nabla^2 h_{i,j}) \quad , \quad (4.13)$$

where  $\gamma$  is the strength of curvature-composition coupling.

## 4.4 Simulation Method

### 4.4.1 Monte Carlo moves

To study the statistical mechanics of the model defined by Eq. (4.9), we use Monte Carlo (MC) simulation. To update the spin variables  $s_{i,j}$ , we employ single-spin-flip dynamics, whereby one of the lattice sites  $(i, j)$  is randomly chosen, and its spin variable inverted as  $s_{i,j} \rightarrow -s_{i,j}$ . The proposed flip is accepted with the Metropolis probability,  $P_{\text{acc,flip}} = \min[1, e^{-\Delta\mathcal{H}/k_B T}]$ , where  $\Delta\mathcal{H}$  is the free energy difference computed according to Eq. (4.9),  $k_B$  is the Boltzmann constant, and  $T$  is the temperature. To update the height variables,  $h_{i,j}$ , we use a MC move formulated in Fourier space [Lin and Brown, 2004; Tröster, 2007]. A change in the height variables only affects the Helfrich part and the coupling term of Eq. (4.9). This part of the free energy is conveniently expressed in Fourier space as

$$\mathcal{H}_{\text{Helfrich}}^{\text{Sim}} + \mathcal{H}_x^{\text{Sim}} = \frac{1}{L^2} \sum_{(u,v)} \left[ \left( \frac{\kappa c_1^2}{2a^2} + \frac{\sigma c_2}{2} \right) \tilde{h}_{u,v}^* \tilde{h}_{u,v} - \gamma c_1 \tilde{s}_{u,v}^* \tilde{h}_{u,v} \right], \quad (4.14)$$

where (\*) denotes complex conjugation, and the coefficients are given by

$$\begin{aligned} c_1(u, v) &\equiv 2 [2 - \cos(2\pi u/L) - \cos(2\pi v/L)] \\ c_2(u, v) &\equiv \frac{1}{2} [2 - \cos(4\pi u/L) - \cos(4\pi v/L)] \quad . \end{aligned} \quad (4.15)$$

We emphasize that Eq. (4.14) is the exact result obtained by Fourier transforming the corresponding real space terms using the finite-difference expression of Eq. (4.11), i.e., the energy computed in real space is identical to that in reciprocal space. The Fourier amplitudes,  $\tilde{X}$ , of the spin and height variables are obtained by the two-dimensional Fourier transforms

$$\begin{aligned} \tilde{X}_{u,v} &= \sum_{(i,j)} X_{i,j} e^{-2\pi i(ui+vj)/L} \quad , \\ X_{i,j} &= \frac{1}{L^2} \sum_{(u,v)} \tilde{X}_{u,v} e^{2\pi i(ui+vj)/L} \quad , \end{aligned} \quad (4.16)$$

where  $i = \sqrt{-1}$ , and  $X \in \{h, s\}$ . Note that the amplitudes are not all independent, but related via complex conjugation,  $\tilde{h}_{u,v}^* = \tilde{h}_{L-u, L-v}$ , because Eq. (4.14) must be real.

In general, the mode amplitudes are complex numbers,  $\tilde{h}_{u,v} = (hR)_{u,v} + i(hI)_{u,v}$ , where  $hR$  and  $hI$  denote the real and imaginary parts, respectively (to improve readability, we omit the dependence on  $u, v$  in the subsequent notation). The key point to note is that Eq. (4.14) is quadratic in  $hR$  and  $hI$ . Hence, in thermal equilibrium, these variables are Gaussian distributed according to  $P(x) \propto \exp[-(x - \mu_x)^2/\Gamma_x^2]$ , where  $x \in \{hR, hI\}$ . The average is given by the minimum of Eq. (4.14) as

$$\begin{aligned}\mu_{hR} &= \gamma c_1 \text{Re}[\tilde{s}_{u,v}] / (\kappa c_1^2/a^2 + \sigma c_2) \quad , \\ \mu_{hI} &= \gamma c_1 \text{Im}[\tilde{s}_{u,v}] / (\kappa c_1^2/a^2 + \sigma c_2) \quad ,\end{aligned}\tag{4.17}$$

while the variance follows from equipartition

$$\Gamma_{hR}^2 = \Gamma_{hI}^2 = \frac{1}{2} k_B T L^2 / (\kappa c_1^2/a^2 + \sigma c_2) \quad .\tag{4.18}$$

The exception is for purely real modes, for which  $hI = 0$ . In this case,  $P(hR)$  remains Gaussian with average  $\mu_{hR}$  but increased variance,  $\Gamma_{hR}^2 \rightarrow 2\Gamma_{hR}^2$ .

To update the height variables, a fast Fourier routine is used to compute the spin amplitudes,  $\tilde{s}_{u,v}$ . We then generate a new set of height amplitudes,  $\tilde{h}_{u,v}$ , each one drawn from its corresponding Gaussian distribution, and back-transform to obtain the real space height variables,  $h_{i,j}$ . In this procedure, there is no accept/reject decision. The advantage of this MC move is that it yields a completely decorrelated set of height variables, at the expense of two (fast) Fourier transforms. In our simulations, spin flips and Fourier height moves are typically attempted in a ratio ( $10L^2 : 1$ ), respectively.

#### 4.4.2 Order parameter distribution

In the analysis to be presented, a key role is played by the order parameter distribution,  $P(m)$ , defined as the probability to observe the membrane with composition,  $m = L^{-2} \sum_{(i,j)} s_{i,j}$ . During the simulations, as spins are flipped,  $m$  fluctuates;  $P(m)$  is the histogram of observed  $m$  values. The distribution depends on all the model parameters, including the system size  $L$ . For a system of size  $L$ , there are  $L^2$  possible values of the composition. To accurately obtain  $P(m)$ , it is required that the simulation visits all of them. We used successive umbrella sampling for this purpose [Virnau and Müller, 2004], where the range,  $L^2 m = -L^2, -L^2 + 2, \dots, L^2$ , is sampled on successive steps. As the number of steps grows  $\propto L^2$ , this analysis is restricted to relatively small systems,  $L \approx 40$ . In cases where only a single snapshot is required, for instance to measure

the structure factor, much larger lattices  $L = 200$  can be used. To enhance efficiency, we used histogram reweighting [Ferrenberg and Swendsen, 1989] to extrapolate data obtained for given model parameters (here:  $J$  and  $\gamma$ ) to different (nearby) values.

### 4.4.3 Model parameters and units

In what follows, we use reduced coupling constants  $J, \kappa, \sigma$ , and  $\gamma$ , which have a factor  $1/k_B T$  absorbed into them. All lengths are measured in units of the lattice spacing,  $a$ . We set  $\kappa = 20$  and  $\sigma = 1$ . With this choice, we expect  $\gamma_{\text{Lif}} = \sqrt{\sigma B}$  to be of order unity. The characteristic length of the composition fluctuations is then  $l \sim (\kappa/\sigma)^{1/2} \approx 4.5$ . Because this physically relevant length scale is significantly larger than our spatial discretization,  $l \gg a \equiv 1$ , our choice mitigates lattice artifacts of the discretized curvature Hamiltonian. Yet,  $l$  is small enough such that we can investigate systems that comprise many domains,  $L \gg l$ . If we take typical values for the membrane tension  $\sigma \sim 10^{-5} - 10^{-6}$  N/m [Schick, 2012], ambient temperature  $T = 300$  K, and bending rigidity  $\kappa = 20 k_B T$ , then  $(\kappa/\sigma)^{1/2} \approx 90 - 300$  nm.

## 4.5 Results

### 4.5.1 No curvature coupling: $\gamma = 0$

For  $\gamma = 0$ , the model defined by Eq. (4.9) reduces to the 2D Ising model [Honerkamp-Smith et al., 2008]. In situations where the composition  $m$  can fluctuate freely, the corresponding phase behavior is as follows: For  $J > J_{\text{crit}} = \ln(1 + \sqrt{2})/2 \approx 0.44$ , the Ising model phase separates into two coexisting phases – one where the majority of spins are positive (composition  $m > 0$ ), and one where they are negative (composition  $m < 0$ ). These phases are identified as the Lo phase and the Ld phase. When  $J < J_{\text{crit}}$ , the Ising model is in the disordered fluid phase, characterized by  $m = 0$ . The transition, at  $J = J_{\text{crit}}$ , is continuous, and belongs to the 2D Ising universality class. This corresponds to the point Is in Fig. 4.1. In cases where the composition is fixed, which is typical for experiments, the same scenario applies provided that  $m = 0$ . For  $m \neq 0$ , the transition occurs at a larger value of  $J$  and is first-order.

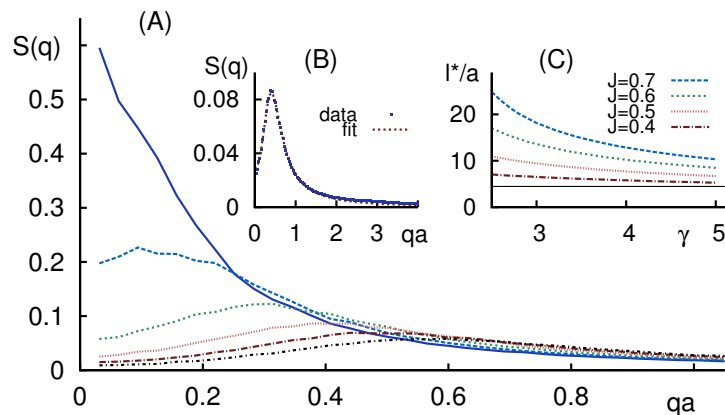


**Figure 4.2:** Membrane structure in the disordered fluid phase, i.e., regions  $f_1$  and  $f_2$  of the phase diagram (data for  $J = 0.4$ ,  $L = 200$ , with the lattice constant  $a$  as the unit of length). **(A)** Static structure factor,  $S(q)$ , for curvature-composition coupling,  $\gamma = 0, 1, 2, 3, 4, 5$  (from *top* to *bottom*). When  $\gamma = 0$ ,  $S(q)$  assumes its maximum at  $q = 0$ , characteristic of region  $f_1$ . When  $\gamma > \gamma_{\text{Lif}}$ , the maximum occurs at a finite value,  $q^* > 0$  (region  $f_2$ ), and shifts to larger  $q$  as  $\gamma$  increases. In region  $f_2$ , the membrane resembles a raft phase, with composition fluctuations of typical size  $l^*$ . **(B)** Comparison between the simulated  $S(q)$  (data) and the mean-field form Eq. (4.6) for  $\gamma = 3$  (fit). **(C)**  $l^*$ , as computed via Eq. (4.20), as a function of  $\gamma$ , for several values of  $J$ . As  $\gamma$  increases, the curves approach the theoretical estimate  $\sim (\kappa/\sigma)^{1/2}$  [Schick, 2012] (indicated by the *horizontal line*).

#### 4.5.2 Fluid phase with curvature coupling

We now consider the fluid phase in the presence of curvature-composition coupling  $\gamma > 0$ , corresponding to regions  $f_1$  and  $f_2$  in Fig. 4.1. Because this is the one-phase region, the Ising interaction constant  $J$  is below its critical value  $J_{\text{crit}}$ . Here, we choose  $J = 0.4$ . In Fig. 4.2A, we show the static structure factor,  $S(q)$ , for several  $\gamma$ , where

$$S(\vec{q}) = \left\langle \frac{1}{L^2} \left| \sum_{(i,j)} s_{i,j} \exp(i\vec{q} \cdot \vec{r}) \right|^2 \right\rangle, \quad (4.19)$$

with  $\vec{r} = (i, j)$ , wave vectors  $\vec{q} = 2\pi(u, v)/L$ , and  $\langle \cdot \rangle$  denoting the thermal average. Note that Fig. 4.2 shows the angular averaged  $S(q)$ , where  $q = |\vec{q}|$ . For  $\gamma = 0$ ,  $S(q)$  reaches its maximum at  $q = 0$ . When  $\gamma$  exceeds a threshold value  $\gamma_{\text{Lif}}$ ,  $S(q)$  reaches its maximum at a finite wave vector,  $q^* > 0$ . In Fig. 4.2B, we compare the simulated structure factor to the mean-field prediction of Eq. (4.6) using  $\gamma = 3$ . We observe that the simulated  $S(q)$  can be well fitted with the mean-field form (in fitting to Eq. (4.6), the ratio  $\sigma/\kappa$  was set to the value used in the simulation;  $A, B, \gamma$  were the fit parameters). The threshold

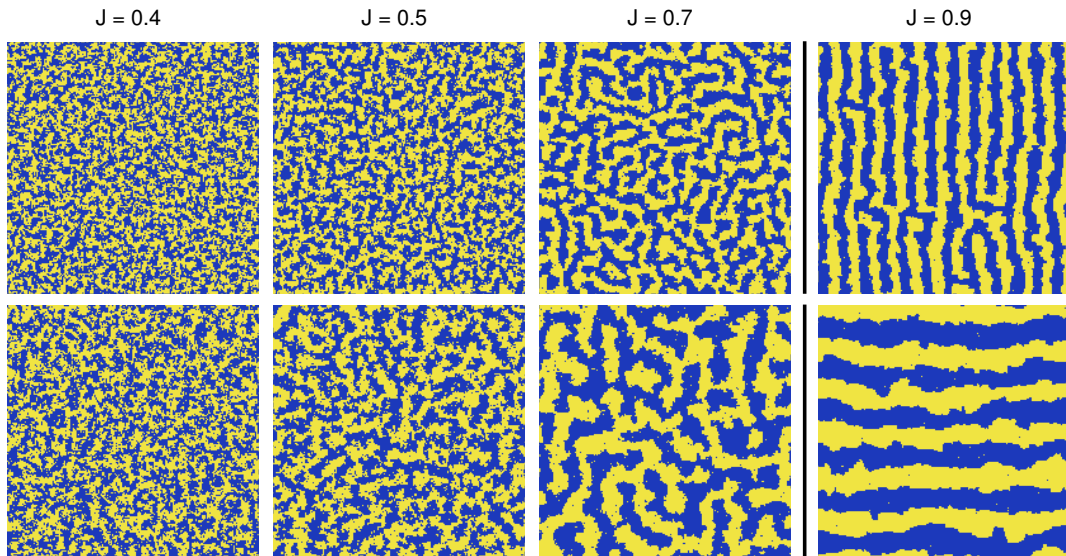


**Figure 4.3:** Typical membrane configurations, for several values of  $J$ , and for two values of the curvature-composition coupling, namely  $\gamma = 5$  (*top row*) and  $\gamma = 3$  (*lower row*). The lattice size is  $L = 200$ . (*Blue*) Lo domains; (*yellow*) Ld domains. The snapshots left of the vertical line ( $J \leq 0.7$ ) correspond to the raft region  $f_2$  of the phase diagram of Fig. 4.1. In this case, the membrane is characterized by composition fluctuations of typical size  $\sim (\kappa/\sigma)^{1/2}$  [Schick, 2012], but there is no long-range order. The snapshots at  $J = 0.9$  show modulated phases (region mod of Fig. 4.1), where the domains have crystallized into lamellae (in two dimensions, we do not expect the orientational order to be long-ranged, but rather to decay algebraically with system size [Toner and Nelson, 1981]).

value of  $\gamma$  where  $q^*$  first becomes nonzero marks the crossing of the Lifshitz line, where the membrane goes from region  $f_1 \rightarrow f_2$ . The biological significance is that, once this line has been crossed, the membrane is characterized by composition fluctuations of a characteristic size  $l^* = 2\pi/q^*$ . In simulations, it is convenient to measure  $l^*$  numerically using the formula [Newman and Barkema, 1999]

$$l^* = 2\pi \frac{\int S(q) dq}{\int q S(q) dq} . \quad (4.20)$$

Fig. 4.2C shows  $l^*$  versus  $\gamma$  for various  $J$ . As  $\gamma$  increases, the curves approach to a common value. Schick [2012] predicts this length to be of  $\sim (\kappa/\sigma)^{1/2}$ , marked with the horizontal line. The presence of a characteristic length scale  $l^*$  may also be inferred from simulation snapshots that are presented in Fig. 4.3. Shown are typical membrane configurations, for two values of  $\gamma$ , and several values of  $J$ .

Next, we ask whether the raft domains are functional, i.e., be able to serve as platforms

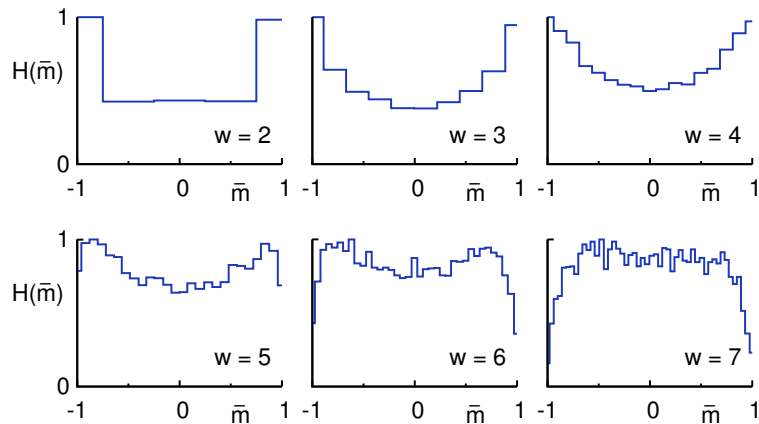


**Figure 4.4:** Results of a grid analysis at  $J = 0.43$  and  $\gamma = 1$  showing the histogram  $H(\bar{m})$  of the normalized composition  $\bar{m}$  measured in  $w \times w$  cells. For  $w$  in the range of the raft size  $\sim (\kappa/\sigma)^{1/2} = 4.5$ , the histograms remain distinctly bimodal, implying a clear contrast between raft domains ( $\bar{m} \sim +1$ ) and the surrounding host phase ( $\bar{m} \sim -1$ ).

for biologically relevant tasks. To this end, there should be a composition contrast between the raft domains, and the surrounding host phase. To show the contrast, we performed a grid analysis at  $J = 0.43$  and  $\gamma = 1$ . For  $\gamma = 1$ , macroscopic Lo/Ld phase separation occurs when  $J \gtrsim 0.51$  (evidence is presented in the next section). Hence,  $J = 0.43$  is deep inside the fluid region  $f_2$  of the phase diagram, well away from the Lo/Ld coexistence region ( $J = 0.43$  is even below  $J_{\text{crit}}$  of the 2D Ising model). In the grid analysis, a  $w \times w$  cell is selected randomly from the snapshot, and the (normalized) composition  $\bar{m} = (1/w^2) \sum_{i \in \text{cell}} s_i$  in that cell is recorded. One then repeats this procedure for different random locations in a snapshot and different snapshots along the simulation trajectory, and constructs a histogram  $H(\bar{m})$  of the observed composition values on the length scale,  $w$ . In Fig. 4.4, we show how  $H(\bar{m})$  depends on the grid size,  $w$ . For small  $w$ , the histograms are distinctly bimodal, whereas for large  $w$  a single peak is observed. For  $w$  corresponding to the raft size, which for our parameters is  $\sim 4.5$ ,  $H(\bar{m})$  is still bimodal, showing that raft domains ( $\bar{m} \sim +1$ ) are clearly resolved from the surrounding phase ( $\bar{m} \sim -1$ ). The results of Fig. 4.2 and Fig. 4.4 provide a numerical confirmation of Schick’s hypothesis [Schick, 2012]. If composition is coupled to curvature, there indeed exists a fluid phase,  $f_2$ , with composition fluctuations compatible with the raft scale. This fluid phase persists well away from the Lo/Ld coexistence region, i.e., it does not require the membrane to be tuned close to a critical point.

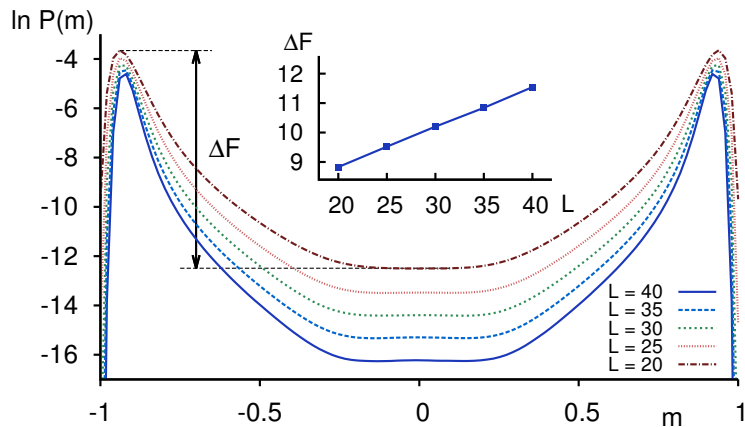


**Figure 4.5:** Simulation evidence showing that, for  $J = 0.53$  and  $\gamma = 1$ , the membrane is in the two-phase Lo/Ld coexistence region. (*Main panel*) Probability distribution,  $\ln P(m)$ , for several system sizes,  $L$ . The distributions are distinctly bimodal. (*Vertical double-arrow*) For  $L = 20$ , defining the barrier  $\Delta F$ . (*Inset*)  $\Delta F$  versus  $L$ ; a linear increase is observed, consistent with the expected scaling for coexistence in  $D = 2$  dimensions [Lee and Kosterlitz, 1991].

### 4.5.3 Phase transitions

As stated above, for  $\gamma = 1$  and  $J \gtrsim 0.51$ , the membrane is in the Lo/Ld coexistence region. This conclusion is based on the order parameter distribution,  $P(m)$ , introduced in Section 4.4.2. In Fig. 4.5 (*main panel*), we show  $\ln P(m)$  for  $\gamma = 1$  and  $J = 0.53$ . We observe a pronounced bimodal distribution, featuring two sharp peaks symmetrically distributed around  $\sim m = 0$ . This bimodal shape is the hallmark of two-phase coexistence [Vollmayr et al., 1993], each peak representing one phase – in this case, the Lo and Ld phases. To ensure that the observed bimodal shape is not a finite-size artifact, Fig. 4.5 (*inset*) shows how the free energy barrier  $\Delta F$  (*double arrow*) scales with the lattice size. As  $L$  increases,  $\Delta F$  linearly increases, providing further confirmation of genuine Lo/Ld coexistence [Lee and Kosterlitz, 1991]. The slope,  $\Delta F/2L > 0$ , quantifies the line tension between the two laterally coexisting phases [Binder, 1982].

In mean-field theory, the transition between the fluid and the Lo/Ld coexistence region is continuous. Our simulations, in contrast, reveal that the latter transition becomes first-order, provided  $\gamma$  is large enough. To quantify this, we study the composition fluctuation  $\chi = L^2(\langle m^2 \rangle - \langle |m| \rangle^2)$  [Orkoulas et al., 2000], with averages defined as  $\langle f(m) \rangle = \int f(m)P(m) dm$ . In Fig. 4.6A, we plot  $\chi$  versus  $J$  for various lattice sizes  $L$  at  $\gamma = 1$ . For each curve, there is a value  $J = J_L$ , where  $\chi$  reaches its maximum  $\chi_L$ . The observation of a maximum in the composition fluctuation is the hallmark of a phase transition. However, phase transitions are defined only in the thermodynamic limit



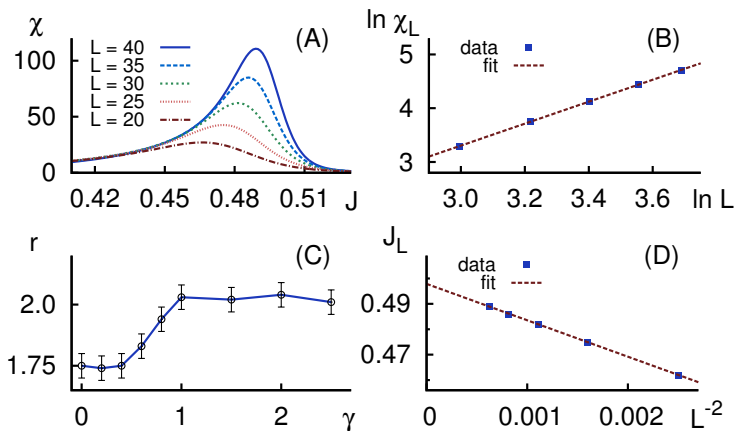


**Figure 4.6:** Finite-size scaling analysis of the phase transition between the Lo/Ld coexistence region and the fluid phase. (A) The composition fluctuation  $\chi$  versus  $J$  for various system sizes  $L$  and  $\gamma = 1$ . The pronounced peak, at  $J = J_L$ , and the increase of the peak height  $\chi_L$  with  $L$ , indicates that a phase transition occurs. (B) The scaling of the maximum composition fluctuation  $\ln \chi_L$  with  $\ln L$  for  $\gamma = 1$ . The linear increase indicates a power-law  $\chi_L \propto L^r$ , with  $r \sim 2.0$  obtained by fitting. This shows that the transition for  $\gamma = 1$  is first-order. (C) The exponent  $r$  versus  $\gamma$ . For large  $\gamma$ , the transition is first-order ( $r = 2$ ), whereas lower values of  $\gamma$  reveal a continuous transition approaching  $r = 7/4$  of the 2D Ising model. (D)  $J_L$  versus  $L^{-2}$  for  $\gamma = 1$ . (Dashed line) Linear fit, whose intercept yields  $J_\infty$  of the thermodynamic limit.

$L \rightarrow \infty$ , and so we must carefully check how our data scale with  $L$ . Finite-size scaling theory [Binder and Landau, 1984; Vollmayr et al., 1993; Binder, 1997; Newman and Barkema, 1999] predicts that  $\chi_L \propto L^r$ , with  $r = 7/4$  if the transition is critical and of the 2D Ising universality class, and  $r = D = 2$  if the transition is first-order with  $D$  being the spatial dimension. In Fig. 4.6B, we plot  $\chi_L$  versus  $L$  on double logarithmic scales. The expected power-law scaling is strikingly confirmed, with an exponent,  $r \approx 2.0$ , obtained by fitting. Hence, our scaling analysis indicates that for  $\gamma = 1$  the transition is first-order. In Fig. 4.6C, we plot  $r$  versus  $\gamma$ . For small  $\gamma$ , the exponent,  $r$ , approaches the 2D Ising value. This is to be expected because, for  $\gamma = 0$ , Eq. (4.9) is the Ising model.

From this simulation evidence, we propose the following scenario for the transition between the fluid phase and the Lo/Ld coexistence region: In the absence of curvature-composition coupling,  $\gamma = 0$ , the transition is continuous and of the 2D Ising class. For large  $\gamma$ , the transition is first-order. Hence, there is a special intermediate value,  $\gamma = \gamma_{\text{tri}}$ , where the type of the transition changes from continuous to first-order – in the language of phase transitions, this is called a tricritical point [Müller and Binder, 2001]. In the thermodynamic limit, we thus expect that  $r = 7/4$  for  $\gamma < \gamma_{\text{tri}}$ , and  $r = 2$  for  $\gamma > \gamma_{\text{tri}}$ .

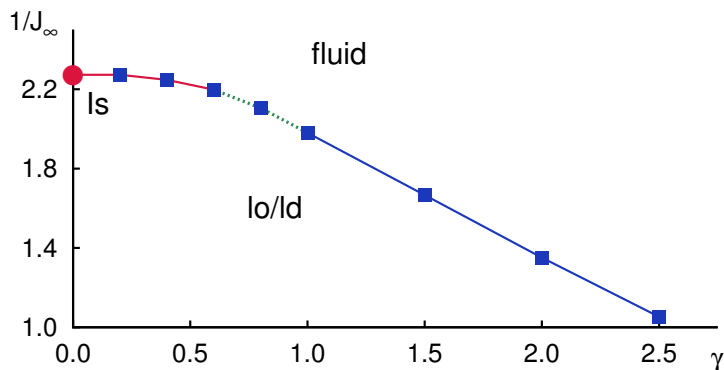


**Figure 4.7:** The simulated phase diagram of Eq. (4.9) in the regime of small  $\gamma$ . Plotted is  $1/J_\infty$  versus  $\gamma$ , which separates the fluid phase from the Lo/Ld coexistence region (*squares* indicate the results of our finite-size scaling analysis, the *dot* marks the exact location of the 2D Ising critical point). For  $\gamma < \gamma_{\text{tri}}$  ( $\gamma > \gamma_{\text{tri}}$ ), the transition between the fluid and the Lo/Ld region is 2D Ising-critical (first-order). Based on the scaling analysis of Fig. 4.6C, we estimate the tricritical point to be  $\gamma_{\text{tri}} \sim 0.6 - 1.0$ .

The smooth variation of  $r$  depicted in Fig. 4.6C indicates that the systems considered by us are too small to see the asymptotic scaling behavior. In these situations, one observes crossover scaling [Anisimov et al., 2005], which is characterized by effective exponents in-between the Ising and first-order values. Hence, a precise determination of  $\gamma_{\text{tri}}$  is not possible, but we estimate  $\gamma_{\text{tri}} \approx 0.6 - 1.0$  because the slope of  $r$  versus  $\gamma$  changes most rapidly in this interval. The reason that prevents us from locating the tricritical point more precisely is the requirement that  $L$  must be large compared to the physical length scale  $(\kappa/\sigma)^{1/2} \sim 4.5$  of the noncritical composition fluctuations. In terms of the latter length, our simulated systems are clearly very small, and so we cannot reach the accuracy that is typical for studies of tricritical behavior using simpler models [Wilding and Nielaba, 1996].

Finally, we present the simulated phase diagram, in the regime of small  $\gamma$ . For each  $\gamma$ , the inverse transition temperature,  $J_\infty$ , in the thermodynamic limit was obtained using the finite-size scaling formula  $J_\infty - J_L \propto 1/L^s$ . For the 2D Ising model,  $s = 1$ , whereas for a first-order transition,  $s = D = 2$ . In Fig. 4.6D, we show the result of the corresponding linear fit for  $\gamma = 1$  using  $s = 2$ ; the intercept yields  $J_\infty$ . Because  $\gamma_{\text{tri}}$  is not precisely known, it is not clear which value of  $s$  to use in the extrapolation. However, the resulting estimates do not sensitively depend on  $s$ . We therefore performed the fit for both values, and report for  $J_\infty$  the average value. The resulting phase diagram is presented in Fig. 4.7, which shows  $1/J_\infty$  versus  $\gamma$ . This curve separates the fluid phase from the Lo/Ld coexistence region, and it is the simulation analog of the mean-field

phase diagram of Fig. 4.1 for small values of  $\gamma$ . Note that Fig. 4.7 does not show the transitions towards the modulated phase, which one expects for large  $J$  and large  $\gamma$  (see the snapshots for  $J = 0.9$  in Fig. 4.3 or, alternatively, experiments by [Toulmay and Prinz \[2013\]](#)). The analysis of the  $f_2 \leftrightarrow \text{mod}$  transition is very demanding numerically and not attempted here (due to the large value of  $J$ , the accept rate of the spin-flips will be low). We merely remark that, if fluctuations are taken into account, the transition  $f_2 \leftrightarrow \text{mod}$  will shift to larger values of  $J$  and  $\gamma$ , i.e., the region  $f_2$  is expected to be larger than the mean-field estimate of Fig. 4.1 because thermal fluctuations extend the stability of the disordered phase at the expense of the spatially modulated phase.

## 4.6 Conclusions

In this article, we have presented computer simulations of a phase-separating membrane, in which the local composition was coupled to the local membrane curvature. There are two central conclusions to be drawn from this work, as follows.

The first conclusion is the numerical confirmation of the theoretical hypothesis [[Schick, 2012](#)] that curvature-composition coupling can induce a disordered fluid phase with a structure factor, whose maximum occurs at a finite wave vector  $q^* > 0$ . The associated length scale is set by the elastic properties of the membrane, in this case, the bending rigidity  $\kappa$  and the surface tension  $\sigma$ . For typical values of  $\kappa$  and  $\sigma$ , the characteristic scale  $(\kappa/\sigma)^{1/2} \approx 100$  nm, which is compatible with the size of lipid rafts. For biological applications, it is interesting that these curvature-stabilized rafts survive at high temperature, i.e., well above the temperature of Lo/Ld phase separation. Hence, it is not necessary for the membrane to be tuned close to any phase transition. Admittedly, the 100-nm raft scale of this model is on the high end [[Lingwood and Simons, 2010](#)]. However, alternative models are easily formulated, for instance by coupling the composition to the bilayer thickness [[Meinhardt et al., 2013](#)]. This leads to a mathematically similar model, sharing the same generic phase diagram [[MacKintosh, 1994](#)], but with a numerically smaller raft size. The purpose of this article, however, was not to precisely reproduce the raft size, but rather to demonstrate how the generics of membrane phase separation are affected by a coupling to membrane shape.

Our second main result concerns the nature of the transition from the fluid phase to the Lo/Ld coexistence region. Provided the curvature-composition coupling,  $\gamma$ , is large enough, this transition becomes first-order, whereas for small  $\gamma$ , the transition is 2D

Ising-critical. The observation of a first-order transition at large  $\gamma$  is consistent with results obtained for microemulsions [Gompper and Schick, 1990], as well as recent simulations of a Landau-type model [Shlomovitz et al., 2014]. This result is important because membrane phase separation is typically assumed to be a continuous transition belonging to the universality class of the 2D Ising model. As our data show, this assumption may not be justified in situations where membrane composition and curvature are coupled.

Finally, we wish to emphasize the importance of finite-size scaling in the analysis of phase transitions. The systematic investigation of how results depend on system size is not yet standard in biophysics. This can have several consequences, an extreme example being the false identification of phase transitions, as has occurred for the Pink membrane model [Corvera et al., 1993; Sadeghi and Vink, 2012]. Furthermore, in biophysical applications, it could even be that experiments are affected by finite sizes. For instance, a typical fluorescence image spans  $\sim 1 \mu\text{m}$ , which is not that much larger than the 100-nm raft scale of this model.

## Acknowledgments

This work was supported by the *Deutsche Forschungsgemeinschaft* within the collaborative research center SFB-937 *Collective Behavior of Soft and Biological Matter* (projects A6 and A7), and the Emmy Noether program (VI 483).

## Chapter 5

# A lipid bound actin meshwork organizes liquid phase separation in model membranes

Alf Honigmann, Sina Sadeghi, Jan Keller, Stefan W. Hell, Christian Eggeling, and Richard L. C. Vink (2014),  
eLife, 3:e01671.

Published 18 March 2014.

DOI: [10.7554/eLife.01671](https://doi.org/10.7554/eLife.01671)

The manuscript describes a study of phase separation in the model membrane bound to an actin network. Richard Vink and I contributed to the theoretical part. We designed and developed the theoretical membrane model. I performed all simulations (including from-scratch code writing), data acquisition, and data analysis. The figure 4. was created by me. The manuscript was written by Richard Vink together with Alf Honigmann.

## Abstract

The eukaryotic cell membrane is connected to a dense actin rich cortex. We present FCS and STED experiments showing that dense membrane bound actin networks have severe influence on lipid phase separation. A minimal actin cortex was bound to a supported lipid bilayer via biotinylated lipid streptavidin complexes (pinning sites). In general, actin binding to ternary membranes prevented macroscopic liquid-ordered and liquid-disordered domain formation, even at low temperature. Instead, depending on the type of pinning lipid, an actin correlated multi-domain pattern was observed. FCS measurements revealed hindered diffusion of lipids in the presence of an actin network. To explain our experimental findings, a new simulation model is proposed, in which the membrane composition, the membrane curvature, and the actin pinning sites are all coupled. Our results reveal a mechanism how cells may prevent macroscopic demixing of their membrane components, while at the same time regulate the local membrane composition.

## 5.1 Introduction

The lateral heterogeneity of lipids and proteins in the plasma membrane of eukaryotic cells is an important feature for regulating biological function. The most prominent concept for membrane organization, the lipid raft theory, relates lipid phase separation (driven by interactions between cholesterol, sphingolipids, and saturated phospholipids) to membrane protein partitioning and regulation [Simons and Ikonen, 1997; Simons and Sampaio, 2011]. Consequently, understanding lipid phase separation in membranes is a topic of extreme interest. A convenient starting point is to envision the membrane as a two-dimensional (2D) fluid environment through which the various membrane components freely diffuse. This simple picture successfully captures ternary model membranes containing two phospholipid species and cholesterol. At low temperature, these systems macroscopically phase separate into liquid-ordered (Lo) and liquid-disordered (Ld) domains [Veatch and Keller, 2003] and the nature of the transition is consistent with that of a 2D fluid [Honerkamp-Smith et al., 2008, 2009]. Similar behavior was observed in plasma membrane-derived vesicles [Baumgart et al., 2007; Sezgin et al., 2012].

Despite these successes for model membranes, there is growing consensus that this simple picture needs to be refined for the plasma membrane. For example, a remaining puzzle is that the Lo/Ld domains observed in model membranes grow macroscopic in size

(micrometers), whereas lipid domains in plasma membrane are postulated to be tiny (nanometers) [Lenne and Nicolas, 2009]. Additionally, the temperature  $T_c$  below which Lo/Ld domains start to form in plasma membrane derived vesicles is distinctly below  $T = 37^\circ\text{C}$  [Sezgin et al., 2012], and so its relevance at physiological temperature requires further justification. In the case of a free-standing membrane (i.e., in the absence of an actin cortex), experiments have shown that lipid domains at temperatures above  $T_c$  can be induced by crosslinking low abundant membrane constituents [Hammond et al., 2005; Lingwood et al., 2008]. Furthermore, there are numerous theoretical proposals of how a finite domain size above  $T_c$  might be accounted for: vicinity of a critical point [Honerkamp-Smith et al., 2009], hybrid lipids [Palmieri and Safran, 2013], coupling between composition and membrane curvature [Schick, 2012], electrostatic forces [Liu et al., 2005].

In addition to this, the cortical cytoskeleton has also been identified as a key player affecting membrane domain formation [Kusumi et al., 2005]. The latter is a dense fiber network of actin and spectrin on the cytoplasmic side of the eukaryotic plasma membrane. This network is connected to the membrane via pinning sites, such as lipid-binding proteins, transmembrane proteins, or membrane-attached proteins [Janmey, 1998; Mangeat et al., 1999; Janmey and Lindberg, 2004; Saarikangas et al., 2010]. This has led to the hypothesis of the membrane being laterally compartmentalized: the pinning sites structure the membrane into small compartments whose perimeters are defined by the underlying actin network (the so-called ‘picket-fence’ model). This picket-fence network then acts as a barrier to diffusion, which elegantly accounts for confined diffusion of lipids and proteins observed in a single molecule tracking experiments [Kusumi et al., 2005]. In a recent series of simulations, it was subsequently shown that a picket-fence network also acts as a barrier to macroscopic phase separation of lipids [Fischer and Vink, 2011; Machta et al., 2011; Ehrig et al., 2011a]. Instead, a stable mosaic of Lo and Ld domains is predicted, with a domain structure that strongly correlates to the actin fibers. Moreover, this mosaic structure already appears at physiological temperatures. These simulation findings are promising in view of the lipid raft hypothesis, since rafts are postulated to be small, as opposed to macroscopic.

In this paper, we present the first experimental confirmation of these simulation results. To this end, we use an *in vitro* model system consisting of a supported lipid bilayer bound to an actin network. Complementing previous studies [Liu and Fletcher, 2006; Subramaniam et al., 2013; Heinemann et al., 2013; Vogel et al., 2013], our system enables direct observation of Lo/Ld domain formation in the presence of a lipid bound actin

network using superresolution STED microscopy [Hell and Wichmann, 1994; Hell, 2007] and fluorescence correlation spectroscopy (FCS) [Magde et al., 1972; Kim et al., 2007]. Based on our results, we propose an extension of the picket-fence model by including a coupling of the local membrane curvature to the membrane composition. Computer simulations of this extended model show that the pinning effect of the actin network is dramatically enhanced by such a coupling. These results imply that even a low density of pinning sites can induce significant structuring of lipids and proteins in the plasma membrane.

## 5.2 Experimental results

### 5.2.1 Domain formation in membranes without actin

Our model system is a lipid mixture of unsaturated DOPC, saturated DPPC, and cholesterol. Such ternary mixtures are routinely used to approximate the complex lipid composition of the eukaryotic plasma membrane [Dimova et al., 2006]. The phase diagram for this system in the absence of actin is well known [Veatch and Keller, 2003]. For a large range of compositions this system reveals macroscopic Lo/Ld phase coexistence below the transition temperature  $T_c$ , while above  $T_c$  they are homogeneously mixed. The size, shape, and the exact phase transition temperature of Lo/Ld domains depend on the specific model membrane system used. Domains grow largest in unsupported membranes [Honigmann et al., 2010], they are smaller in Mica supported membranes [Jensen et al., 2007] and are below the diffraction limit on glass supported membranes [Honigmann et al., 2013]. Depending on the composition, the transition to the coexistence region can be first-order, or continuous passing through a critical point. In the present work, we choose a composition ratio of (DOPC:DPPC:cholesterol) = (35:35:30) mol%, including 1 mol% of a biotinylated lipid (DOPE-biotin) to eventually connect the membrane to an actin network. To facilitate high resolution microscopy flat, single membranes of that mixture were prepared on a Mica support. After membrane preparation the sample was heated to  $T = 37^\circ\text{C}$  for 15 min to equilibrate the bilayer in the mixed phase. At this stage, the connector protein streptavidin was bound to the biotinylated lipid (but not yet to actin). After this preparation the membrane was slowly cooled and the distribution of the red fluorescent Ld-marker (DPPE-KK114) was determined by superresolution STED imaging. Visual inspection of images revealed that, upon cooling, there is a well-defined temperature at which Lo/Ld domains became visible (Fig. 5.1A). This temperature is



around  $T_c \approx 28^\circ\text{C}$  and thus marks the transition between the mixed one-phase state at high temperature, and the low-temperature two-phase coexistence state. This phase transition temperature is close but slightly decreased compared to the reported value for lipid vesicles made of the same mixture ( $T_c \approx 28^\circ\text{C}$  [Veatch et al., 2004]). At  $T_c$ , domains were constantly forming and re-forming, implying that the line tension is small, and so the transition is close to critical. The transition from a one-phase to a Lo/Ld separated two-phase membrane can be analyzed more quantitatively via the cumulant  $U_1$  of the images (see ‘Materials and methods’ for definition). In the one-phase region,  $U_1 = \pi/2$ , whereas for a two-phase system  $U_1 = \pi/2$  ([Binder, 1981b; Fischer and Vink, 2011]). As shown in Fig. 5.1C,  $U_1$  markedly dropped toward unity below  $T_c$ . Once the membrane enters the two-phase region, domains were seen to coarsen within a couple of minutes. The typical domain size  $R$  was obtained from the radial distribution function  $g(r)$  of the images. As shown in Fig. 5.1D,  $R$  increased rapidly at  $T_c$ , from  $< 75$  nm to 200 nm, and continued to grow into the near micrometer range as the temperature was lowered further. These findings are consistent with atomic force microscopy experiments [Connell et al., 2013], where the transition was shown to be continuous as well. The observation that the domains do not fully coalesce at low temperature (as opposed to free-standing membranes) can be attributed to the interaction of the membrane with the mica support [Jensen et al., 2007]. Our data do not allow the nature of the transition to be unambiguously identified. We emphasize, however, that this does not affect the overall conclusions of our work. All that we require is that the system without actin reveals two-phase coexistence at low temperatures.

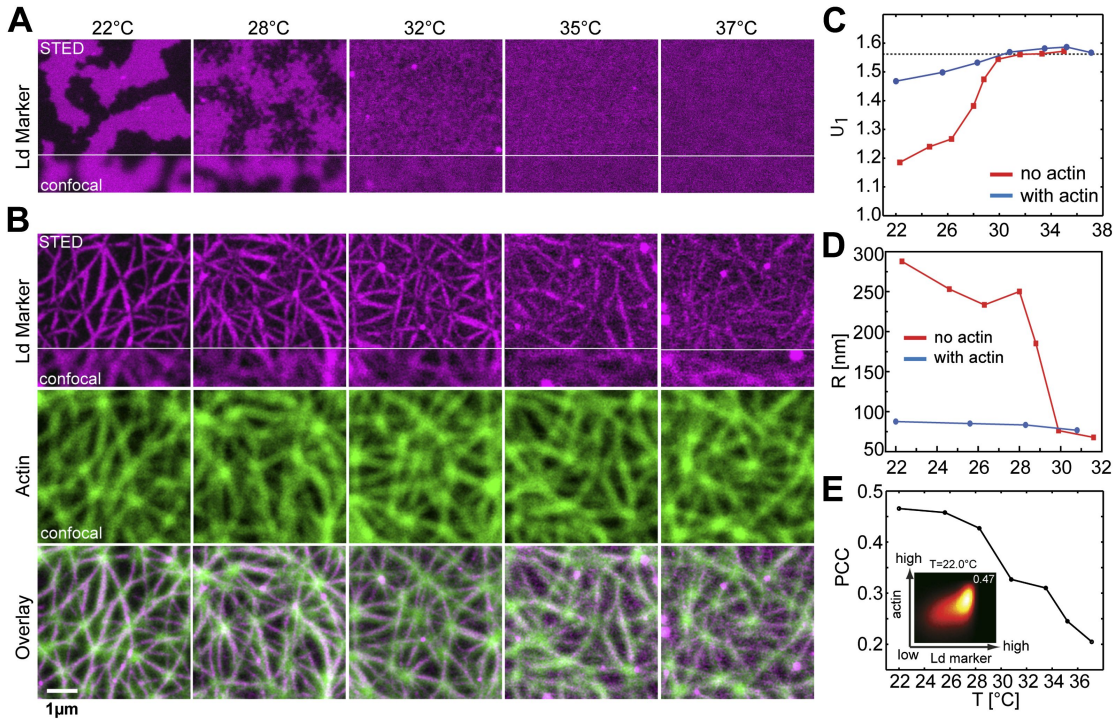


**Figure 5.1:** Binding of an actin network to ternary membranes dramatically affects lipid domain structure. **(A)** In the absence of actin, our Mica supported model membrane revealed a phase transition at  $T_c \approx 28^\circ\text{C}$ , below which macroscopic Lo/Ld phase separation was observed. The membrane was stained with the Ld-marker DPPE-KK114 (magenta), and imaged by STED-microscopy with a lateral resolution of 70 nm. **(B)** The same membrane as in **(A)** but now in the presence of an actin network (green) bound to the membrane via a streptavidin linker. The Ld domains were strongly correlated to the actin network, as can be seen in the overlay, resulting in a meshwork like structure of Ld channels. This structure was stable even at temperatures above  $T_c$ . **(C)** Variation of the cumulant  $U_1$  of the images with temperature  $T$  in the absence of actin (red) and presence (blue). In the absence of actin, there is a transition toward a two-phase coexistence region at low temperature, as manifested by a pronounced drop of  $U_1$  toward unity. The transition occurs at  $T_c \approx 28^\circ\text{C}$ . In the presence of actin, no such transition is detected. **(D)** Typical domain size  $R$  as a function of  $T$ . In the absence of actin, there was pronounced domain coarsening below  $T_c$ . In the presence of actin,  $R$  was essentially temperature independent, and restricted to at most 90 nm. Note that  $R$  could not be measured for temperatures above  $T = 32^\circ\text{C}$  as the contrast of the domains became too low. **(E)** Pearson correlation coefficient (PCC) between Ld domains and actin vs temperature. This coefficient measures the degree of correlation between Ld domains and the actin fibers. The correlation is largest at low temperature, but it persists at high temperature also, including the physiological temperature  $T = 37^\circ\text{C}$ . Inset shows the graphical representation of the correlation between high intensities in the actin channel with high intensities in the lipid channel (Ld phase). For another example of phase reorganization by actin binding see Fig. 5.1-supplement 1. For actin meshwork binding to single component DOPC membranes see Fig. 5.1-supplement 2.

### 5.2.2 Domain formation in membranes with actin

Having characterized the phase behavior of the membrane without actin, we heated the same membrane back to the mixed state at  $T = 37^\circ\text{C}$  to bind actin fibers via phalloidin–biotin to the streptavidin–biotin–lipid complexes (a molecular sketch is provided in Fig. 5.1-supplement 3). The resulting binding sites strongly attract the Ld phase with a partitioning value of  $\text{Lo}\% = 10$  for DOPE-biotin (Fig. 5.1-supplement 1). The actin fibers were stained with a green fluorescent phalloidin. After the actin meshwork was bound to the membrane, the temperature was again decreased, and the distributions of the Ld-marker DPPE-KK114 and the actin were imaged simultaneously using (super-resolution) STED and (diffraction limited) confocal microscopy, respectively. Visual inspection of images (Fig. 5.1B) revealed that, with actin, domains already appeared at  $T = 37^\circ\text{C}$ . The spatial domain structure, however, was very different compared to the actin-free case. We observed a partitioning of the membrane into compartments of Lo-enriched domains, separated by ‘channels’ of Ld-enriched domains. These channels were clearly correlated to the actin fibers (middle row), as shown in the overlay (lower row). This correlation was analyzed quantitatively via the Pearson measure (PCC), which is an estimate of the colocalization between the Ld domains and the actin fibers (see ‘Materials and methods’ for definition). In general, a large value  $\text{PCC} > 0$  indicates a pronounced overlay of structures,  $\text{PCC} = 0$  indicates randomly distributed objects, whereas  $\text{PCC} < 0$  represents inverted features (i.e., anti-correlations). We observed that PCC is largest at low temperature, implying that the correlation between Ld domains and actin is strongest there (Fig. 5.1E). However, PCC remains finite at high temperatures also, with a significant correlation up to our highest accessible temperatures of  $T = 37^\circ\text{C}$ , which is a stunning  $9^\circ\text{C}$  above  $T_c$  of the actin-free membrane. For  $T > 28^\circ\text{C}$ , the decrease of PCC is approximately linear. This decrease was caused by an increasingly even partitioning of the Ld-marker, and not by a redistribution of Ld domains away from the actin fibers (as follows from Fig. 5.1B, where correlated domains remain clearly visible at  $T = 37^\circ\text{C}$ ). In contrast to the actin-free case, our data suggest that there is no phase transition associated with the formation of the domain structure: Neither the cumulant nor the domain size revealed any pronounced temperature dependence (Fig. 5.1C,D). Also the variation of PCC with temperature is entirely smooth, and does not indicate a transition either. Furthermore, in the presence of actin, the average domain size was significantly smaller,  $R \approx 90$  nm at most, and no coarsening was observed. Our conclusion is that the phase transition of the actin-free membrane is

effectively eliminated by the actin network, in line with theoretical expectations [Fischer and Vink, 2011; Machta et al., 2011].

As control experiment, we also considered a single component bilayer (DOPC) bound to actin. In this case, no domains were induced by the actin (Fig. 5.1-supplement 2). Additionally, we excluded the possibility that the actin-correlated phases were induced by the green fluorescent phalloidin. To this end, we stained the membrane with the Ld-marker (red) and the Lo-marker (green) but not the actin itself. The result was a comparable structure as observed in Fig. 5.1B, see Fig. 5.1-supplement 1.

### 5.2.3 The lateral diffusion of lipids is restricted by actin-organized domains

To determine the lateral movement of lipids in the membrane in relation to the actin fibers, we applied scanning FCS [Digman et al., 2005; Ries and Schwille, 2006; Digman and Gratton, 2009]. We used the same system as described above, but now with a lower density of actin such that single fibers could be resolved by confocal microscopy. The temperature was set to  $T = 32^\circ\text{C}$ , that is slightly above  $T_c$  of the actin-free membrane. As a control, we started with actin fibers on a single component DOPC membrane including 1 mol% DOPE-biotin (compare Fig. 5.1-supplement 2B). A small circle (diameter  $d = 500$  nm) was scanned over a single actin fiber, as depicted in Fig. 5.2E. For each position on the circle, the diffusion of the Ld-marker was determined by standard FCS analysis [Kim et al., 2007]. The upper panel in Fig. 5.2A shows the intensity of the Ld-marker (red) and of the actin-marker (green) along the scan circle for the single component membrane (A). The intensity maximum of the green channel indicates the position of the actin fiber (corresponding to 0 and  $180^\circ$ ), the intensity of the red channel shows the corresponding distribution of the Ld-marker. In the single component membrane, the Ld-marker was homogeneously distributed. The lower panels of Fig. 5.2A shows the decay of the autocorrelation function of the Ld-marker measured along the scan circle, with the color representing the amplitude of the correlation. For the single component membrane, the autocorrelation analysis revealed no significant differences in mobility between areas with actin and without. Next, we used the same data to determine the diffusion of lipids across the scanning circle by calculating the pair-correlation function of ‘opposing’ pixels on the scanning circle, that is pixel pairs that are separated by a rotation of  $180^\circ$  [Cardarelli et al., 2012]. This correlation measures how long the

probe on average needs to diffuse across the circle and is therefore more sensitive to detect diffusion barriers than the autocorrelation analysis of a single excitation spot. The resulting pair-correlation is shown in Fig. 5.2B. For the single component membrane, the amplitude and correlation time revealed no clear directional dependence. The average correlation time across the circle was  $\tau \approx 30$  ms, indicating that the pinning of the actin filament imposed no significant diffusion barrier for lipids. These results are in agreement with point FCS measurements on single component membranes in the presence of increasing actin densities, which are reported in Fig. 5.1-supplement 2E. Also here, the lateral diffusion was remarkably insensitive to the presence of actin.

In contrast to the single component membrane, a pronounced directional dependence of lipid diffusion was observed in the ternary system. The intensity distribution of the Ld-marker showed a slight increase at the position of the actin fiber (upper panel Fig. 5.2C), indicating a stabilized Ld phase along the actin fiber. While the autocorrelation analysis along the scan trajectory indicated no clear heterogeneities (lower panel Fig. 5.2C), the pair-correlation function revealed strong peaks at 0 and 180° (i.e., along the actin filament) at delay times  $\tau \approx 30 - 50$  ms (Fig. 5.2D). In the direction perpendicular to the actin fiber, a much weaker amplitude was observed, with the peak shifted to longer times  $\tau > 50$  ms. This indicates that the actin stabilized Ld domains favored the diffusion of the Ld-marker within the domain (and thus along the actin fiber), while restricting diffusion across domain boundaries. These findings strikingly confirm the simulation prediction of Machta et al. [2011], where lipid domains stabilized by actin pinning were also found to ‘compartmentalize’ lipid diffusion.

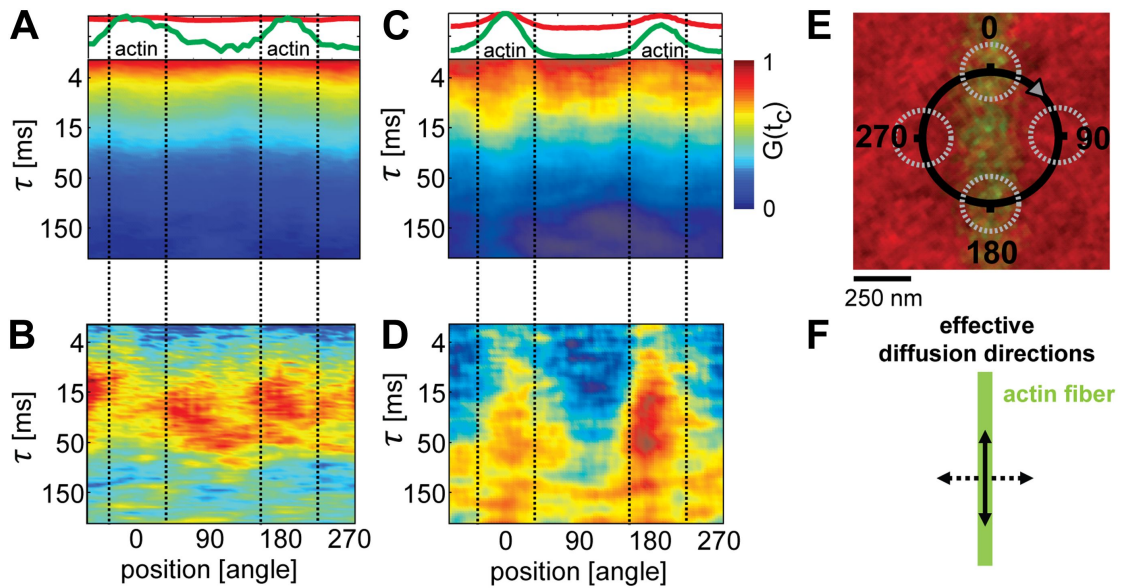


**Figure 5.2:** Lipid diffusion was restricted by actin-organized domains. (A) Scanning-FCS (mobility) analysis of the Ld-marker DPPE-KK114 in a single component DOPC membrane in the presence of a low density actin meshwork. The upper panel shows the intensity of the green channel (actin) and red channel (Ld-marker), indicating the position of the actin fiber on the scan orbit (perpendicular lines). The lower panel depicts the autocorrelation decay for each pixel along the circular scan orbit with a diameter of  $d = 500$  nm. The normalized autocorrelation amplitude is represented by the color. The mean transit time through the excitation spot (mobility) can be estimated by the transition from yellow to green. As expected the mobility along the scan orbit was homogenous. (B) Pair-correlation analysis of the same data as in (A) for opposing pixels on the scan orbit. The maxima in the pair-correlation represent the average time the probes need to move across the scan orbit. No significant directional dependence of the mobility was observed in case of simple one component membranes. (C) Same as in (A) but for ternary membranes (same composition as in Fig. 5.1). (D) While the autocorrelation analysis seemed to be homogenous a distinct directional dependence of diffusion was revealed by the pair-correlation. In the direction along the actin fiber, a distinct correlation peak is visible with a maximum at  $\tau \approx 40$  ms. In the perpendicular direction, the correlation amplitude is reduced, which indicates a diffusion barrier along this axis. (E) Representation of the scanning orbit over a single actin fiber bound to the membrane. The numbers represent the angles of the orbit (F). Qualitative representation summarizing the results of the pair-correlation analysis with pronounced diffusion along (drawn arrow) and restricted diffusion perpendicular to the actin fiber (dashed arrow).

#### 5.2.4 Influence of the type of lipid-pinning site on domain structure

We next consider how domain formation is affected when different pinning sites are used to bind the membrane to the actin network. To this end, we compared three biotinylated lipids with different partitioning values: DOPE-biotin (i.e., the same as used in the experiment of Fig. 5.1) that partitions strongly into the Ld phase ( $\text{Lo}\% = 11 \pm 2$ ), DSPE-PEG-biotin that partitions predominantly in the Lo phase ( $\text{Lo}\% = 78 \pm 7$ ), and DPPE-biotin that partitions almost equally in both phases (but with a small preference toward the Lo phase,  $\text{Lo}\% = 59 \pm 5$ ). The experimental procedure to determine the  $\text{Lo}\%$  is outlined in Fig. 5.3-supplement 1. In Fig. 5.3A, we show confocal images of the domain structure for the Ld-preferring pinning lipid DOPE-biotin. The figure confirms the previous experiment of Fig. 5.1B: We again observe the formation of Ld domains along the actin fibers, as expressed by a positive Pearson coefficient  $\text{PCC} = 0.55 \pm 0.02$ . Pinning of the Lo-preferring lipid DSPE-PEG-biotin induced an ‘inverted’ domain structure, yielding a negative  $\text{PCC} = -0.37 \pm 0.04$  (Fig. 5.3C). The binding of actin to DPPE-biotin did not result in a strong localization of lipid domains along the fibers, as manifested by a small ‘but positive’  $\text{PCC} = 0.07 \pm 0.03$  (Fig. 5.3B). The result of Fig. 5.3B is surprising, since DPPE-biotin slightly prefers the Lo phase, and so a ‘negative’  $\text{PCC}$  was expected. Notwithstanding that several mechanisms could be responsible for this (e.g., streptavidin binding to biotinylated lipids may induce lipid disorder by steric or electrostatic interactions with the membrane), it is interesting that a coupling between membrane composition and curvature also brings about this effect. To illustrate this point, we resort to computer simulations, where important parameters such as pinning density and phase partitioning of pinning sites can be systematically varied.

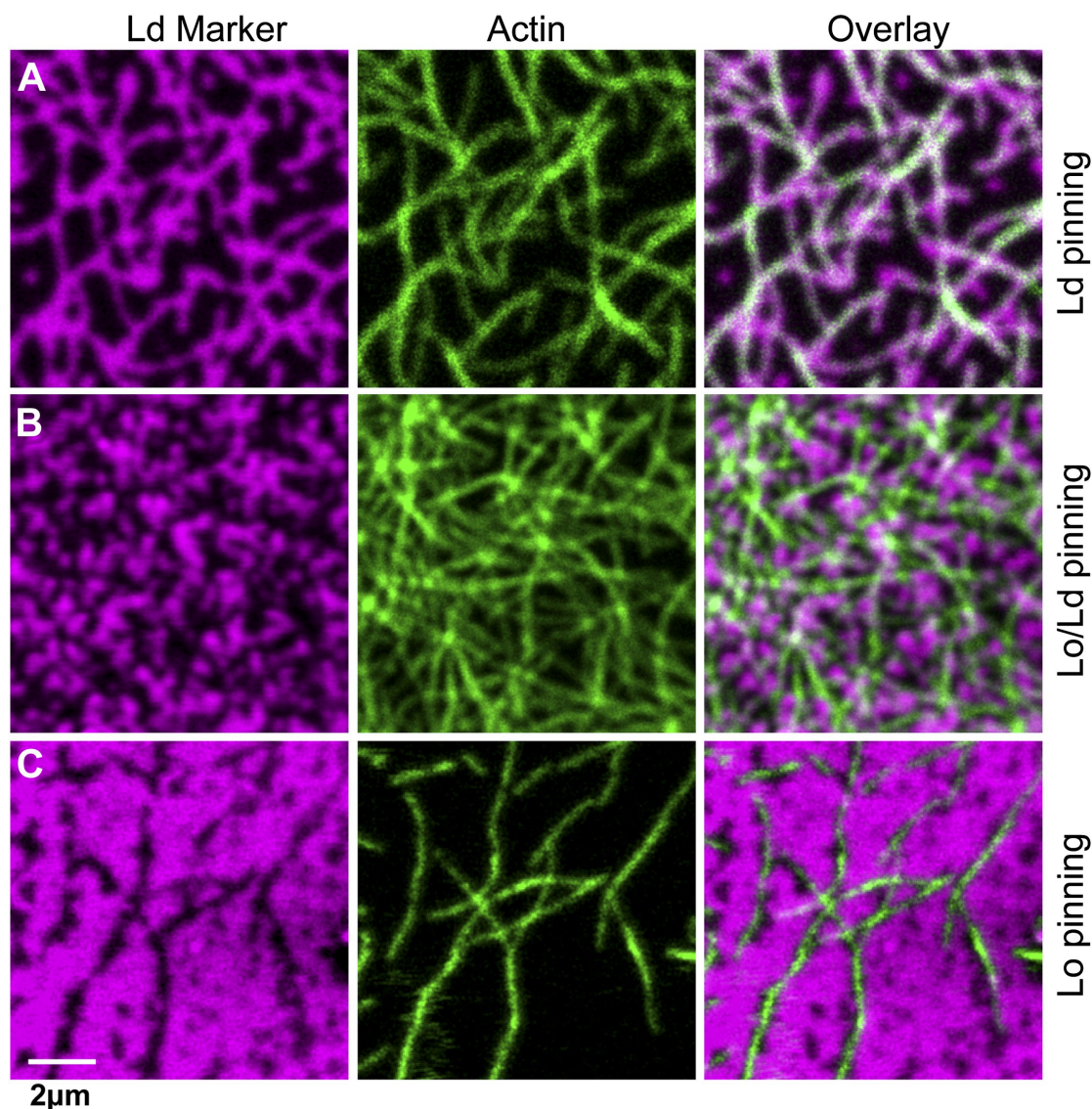


**Figure 5.3:** The type of pinning site used to bind actin to the membrane strongly affects the domain structure. The Ld phase (left column, magenta) were stained with DSPE-KK114, while actin (middle column, green) was stained with phalloidin-488. The right column shows the overlay of both images. The membrane was imaged by confocal microscopy at  $T = 19^{\circ}\text{C}$ , using the same lipid composition as in Fig. 5.1. (A) Binding of actin to the Ld preferring lipid DOPE-biotin resulted in Ld domains along the actin fibers (as in Fig. 5.1B,  $\text{PCC} = 0.55 \pm 0.02$ ). (B) When actin was bound to DPPE-biotin, the correlation of domains with the actin fibers was significantly reduced, but remained detectable, with a slightly positive Pearson coefficient ( $\text{PCC} = 0.07 \pm 0.03$ ). (C) Binding of actin to the Lo preferring lipid DSPE-PEG-biotin resulted in correlated Lo domains along the actin fibers, that is the ‘inverse’ structure of (A). In this case, the Pearson coefficient was negative ( $\text{PCC} = -0.37 \pm 0.04$ ). For the lipid phase partitioning values of the biotinylated lipids used in this experiment see Fig. 5.3-supplement 1.



### 5.3 Simulation results

We simulated a phase separating membrane coupled to a picket-fence network resembling actin using a model similar to Machta et al. [2011] but extended to include membrane curvature. The energy contains three terms:  $\mathcal{H}_{\text{sim}} = \mathcal{H}_{\text{Helfrich}} + \mathcal{H}_{\text{Ising}} + \mathcal{H}_{\text{x}}$  ('Materials and methods'). The first term describes the membrane elastic properties using the Helfrich form [Helfrich, 1973], with bending rigidity  $\kappa$ , and surface tension  $\sigma$ ; the second term describes the phase separation using a conserved order parameter Ising model; the third term couples the phases to the local membrane curvature. The strength of the curvature coupling is proportional to the product of  $\kappa$  and the spontaneous curvature difference between Lo and Ld domains ('Materials and methods'). Since there is a substantial range in the experimentally reported values of  $\kappa$  and  $\sigma$ , a large uncertainty (about one order of magnitude) in the strength of the curvature coupling is implied [Schick, 2012]. For this reason, we allow the curvature coupling strength to be scaled by a (dimensionless) factor  $g$  in our analysis. The latter is defined such that, for  $g > 0$ , regions of positive curvature favor unsaturated lipids, that is Ld domains. For  $g = 0$  our model reduces to the one of Machta et al. [2011]. In situations where curvature coupling is known to occur, one should restrict  $g$  to finite positive values. The influence of the actin network is incorporated via (immobile) pinning sites, which are distributed randomly along the actin fibers (linear pinning density  $\rho_{\text{p}}$ ). At the pinning sites, there is a preferred energetic attraction to one of the lipid species (set by the Lo%). The pinning sites also locally fix the membrane height  $h$ , which we model by keeping  $h = 0$  at these locations (we assume the actin network to lie in a flat plane, providing the reference from which the membrane height is measured). Additionally, there is a steric repulsion between the membrane and the actin: directly underneath the actin fibers, the membrane height is restricted to negative values  $h < 0$ .

We first consider DPPE-biotin pinning sites that slightly prefer Lo domains (Lo% =  $59 \pm 5$ ). Interestingly, the corresponding experiment (Fig. 5.3B) revealed a positive PCC, implying a weak alignment of Ld domains along the actin fibers instead. This contradiction can be rationalized, however, when one considers the membrane curvature. In Fig. 5.4G, we show how the simulated PCC varies with the curvature coupling parameter  $g$ , using pinning density  $\rho_{\text{p}} = 0.1/\text{nm}$ , corresponding to 20% of the total actin network being pinned. The key observation is that, at  $g \approx 20$ , the PCC changes sign and crosses the experimental value. We emphasize that the simulation data were

not corrected for the optical point spread function (PSF) of the experiment; by artificially broadening the simulation images, lower values  $g \sim 10$  were obtained, precluding a precise determination. In addition, the value of  $g$ , where the PCC changes sign also depends on the pinning density: by increasing  $\rho_p$ , also  $g$  must increase to result in a positive PCC. In qualitative terms, the change of sign in the PCC reflects a competition between two effects: an energetic attraction between DPPE-biotin and saturated lipids, favoring alignment of Lo domains, vs a curvature-induced repulsion of these lipids away from the actin fibers. Due to the steric repulsion between the membrane and the actin fibers, the preferred curvature around the fibers is positive on average, thereby favoring Ld domains. At large  $g$ , the latter effect dominates, yielding a positive Pearson coefficient. In Fig. 5.4E, we show a typical snapshot corresponding to  $g = 20$  and  $\rho_p = 0.1/\text{nm}$ . In agreement with the experiment of Fig. 5.3B, we observe a structure of small domains. In contrast, by using  $g = 0$ , the domains grow to be much larger (Fig. 5.4B), contradicting the experimental observations.

Our model also predicts that, in the presence of curvature coupling, the pinning density required to induce domain alignment along the actin fibers can be much smaller. Previous simulations corresponding to  $g = 0$  [Machta et al., 2011; Ehrig et al., 2011a] required rather large pinning densities,  $\rho_p \sim 0.2 - 1.25/\text{nm}$ , in order to achieve this. In Fig. 5.4A, we show a typical domain structure using DOPE-biotin pinning sites ( $\text{Lo}\% = 11 \pm 2$ ) at pinning density  $\rho_p = 0.1/\text{nm}$  in the absence of coupling to curvature ( $g = 0$ ). Fig. 5.4D shows the corresponding snapshot in the presence of curvature coupling, using  $g = 20$ , which is the value of Fig. 5.4G where the PCC changed sign. To reproduce the experimentally observed domain structure (Fig. 5.3A) at low pinning densities, curvature coupling is thus essential. In Fig. 5.4D, the average Ld domain size  $R_{\text{sim}} \approx 40 \text{ nm}$ , which is somewhat below  $R_{\text{exp}} \approx 90 \text{ nm}$  of the experiment (Fig. 5.1D). Note, however, that the experimental value likely presents an upper-bound, due to broadening by the PSF. The case of DSPE-PEG-biotin pinning sites ( $\text{Lo}\% = 78 \pm 7$ ) is considered in Fig. 5.4C,F. Again, curvature coupling is required to reproduce the (now inverted) domain structure of the experiment (Fig. 5.3C). In the presence of curvature coupling, the length scale over which the effect of a pinning site propagates is thus enhanced dramatically. This is due to the elastic properties of the membrane: the bending rigidity and the surface tension define a length  $\xi_h = (\kappa/\sigma)^{1/2}$  [Schick, 2012], which sets the scale over which the membrane height deformations propagate (for our model parameters  $\xi_h \sim 100 \text{ nm}$ ). When  $g > 0$ , this scale couples to the composition, in which case a reduced pinning density already suffices to induce domain alignment. We emphasize that  $\xi_h$  is essentially

independent of temperature, and so it is not necessary for the membrane to be close to a critical point.

Also included in Fig. 5.4 are typical membrane height profiles for the snapshots with curvature coupling (D,E,F) scanned along a horizontal line through the center of each image. These profiles qualitatively illustrate the curvature coupling effect: Ld domains (magenta) reveal positive curvature on average, while for Lo domains (black) the curvature is on average negative. In the absence of coupling to actin and  $g = 0$ , the typical root-mean-square height fluctuation is  $h \approx 3.6$  nm. In the presence of actin and curvature coupling, these fluctuations are significantly reduced to  $h \approx 2$  nm, which is very close to the value reported by [Speck et al. \[2010\]](#).

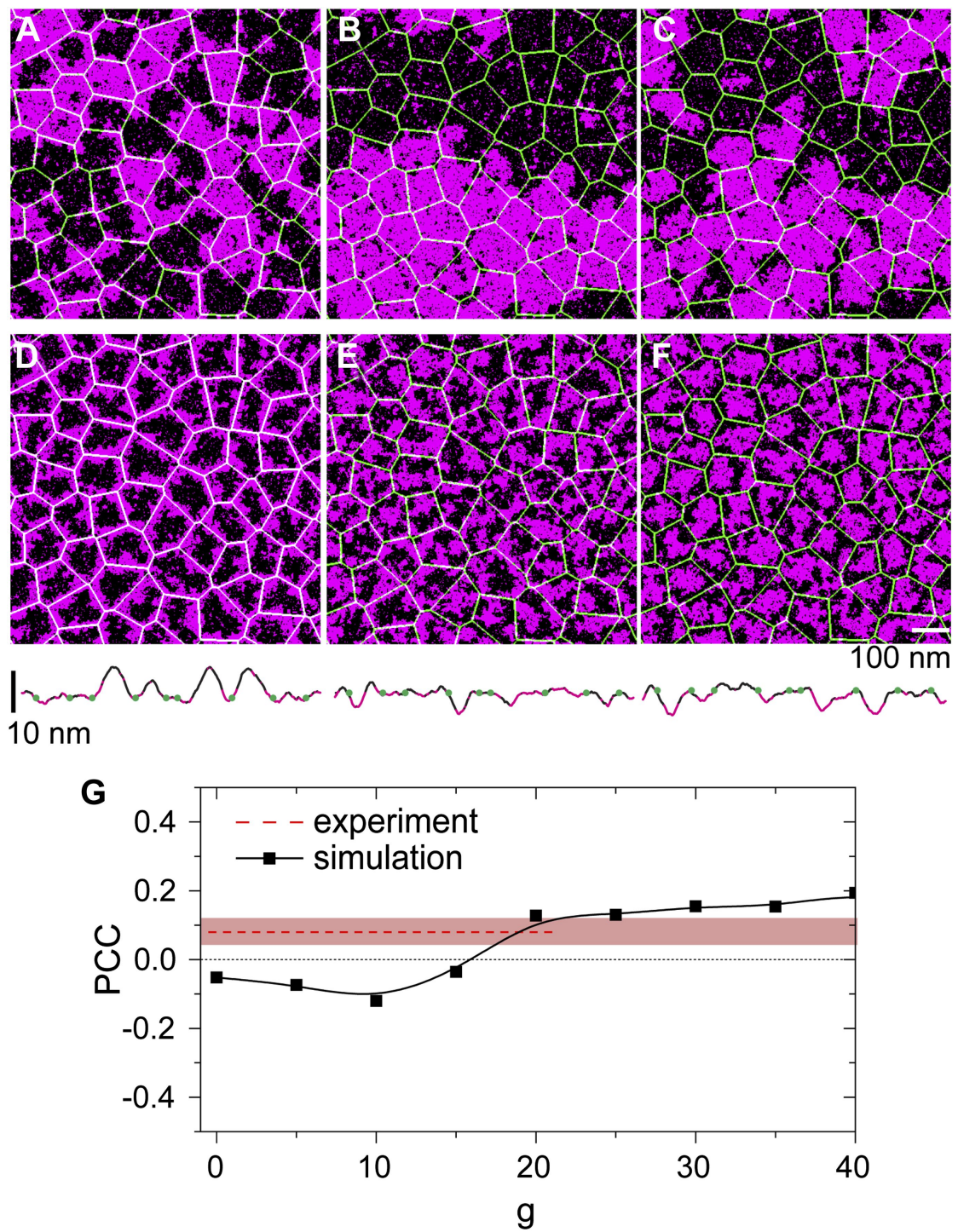


Figure 5.4: (Continued on the following page.)

**Figure 5.4:** Simulation analysis of the influence of pinning and curvature coupling on lipid phase organization. All data refer to  $T = 19^\circ\text{C}$ . The Ld lipids are shown as magenta, the Lo lipids as black, and the actin network is shown in green as an overlay. The pinning density  $\rho_p = 0.1/\text{nm}$ . **(A–C)** Simulation snapshots obtained without coupling to curvature ( $g = 0$ ) for the three species of pinning sites used in the experiments: Lo% =  $11 \pm 2$  (A), Lo% =  $59 \pm 5$  (B), and Lo% =  $78 \pm 7$  (C). No significant influence of the actin network is apparent. **(D–F)** Same as (A–C) but in the presence of curvature coupling ( $g = 20$ ). For snapshots (D) and (F), the lipid domains strongly correlate to the actin network, with Ld domains favoring actin in (D), and the inverse pattern in (F). The lower panels show height profiles of the images (D–F) scanned horizontally along the center of the image; the green dots indicate the positions of the actin fibers. **(G)** Pearson correlation coefficient PCC vs the curvature coupling  $g$  for the pinning species with Lo% =  $59 \pm 5$ . For weak curvature coupling, the PCC is negative indicating alignment of Lo domains along actin. By increasing the curvature coupling, the PCC becomes positive and ‘meets’ the experimentally observed value (conform Fig. 5.4B).

## 5.4 Discussion

We have presented an experimental model system in which the response of membrane organization to a bound actin network can be accurately probed using superresolution STED microscopy and FCS. The application of our model system to a single component liquid-disordered membrane shows that actin has only a minor influence on the lateral distribution and dynamics of lipids (Fig. 5.1-supplement 2, as well as Fig. 5.2A,B). In contrast, under the same conditions using a ternary membrane, the effects are dramatic. In particular, by binding actin using pinning sites that attract the Ld phase, earlier simulation predictions [Fischer and Vink, 2011; Machta et al., 2011; Ehrig et al., 2011a] could finally be put to a stringent test. In agreement with these simulations, our experiments confirm the absence of macroscopic phase separation in the presence of actin. Additionally, our experiments revealed the alignment of Ld domains along the actin fibers, leading to a channel-like domain structure very similar to structures observed in simulations [Fischer and Vink, 2011; Machta et al., 2011; Ehrig et al., 2011a]. Finally, in agreement with the simulations of Machta et al. [2011], the enhanced diffusion of unsaturated lipids along the Ld channels, and the hindered diffusion of these lipids in directions perpendicular, was confirmed. These findings demonstrate that relatively simple simulation models are capable to capture key essentials of lateral membrane organization and dynamics.

However, by using pinning sites that weakly attract the Lo phase, our experiments also uncover phenomena that cannot be explained using these simulation models. The paradox is that, for the latter type of pinning site, one still observes alignment of Ld domains along the actin fibers, albeit weak. This indicates that there must be additional mechanisms at play—beyond the level of the pinning-lipid energetic interaction—playing a role in the lateral organization of the membrane. As possible candidate for such a mechanism, we considered the local membrane curvature, and a coupling of the latter to the lipid composition [Schick, 2012]. A simulation model that incorporates these ingredients is able to reproduce the experimentally observed alignment of Ld domains, even when the pinning sites themselves energetically favor the Lo phase. The physical explanation is that the actin network locally induces regions with non-zero average curvature. The coupling of the curvature to the composition then causes these regions to prefer certain types of lipids. Provided the coupling is strong enough, it can overcome the pinning-lipid energetic interaction, which is how we interpret the experimental result. An additional finding is that, in the presence of curvature coupling, the effect of a pinning site extends

over a much greater distance (set by the elastic properties of the membrane). Hence, the pinning density can be much lower compared to models where such a coupling is absent. We emphasize once more that curvature coupling is not the only conceivable mechanism that could account for our experimental findings. However, a recent experimental study [Kaizuka and Groves, 2010] of membrane phase separation using intermembrane junctions did uncover a very pronounced curvature coupling, making this a likely candidate.

There are interesting implications of our results concerning the *in vivo* organization of the plasma membrane. Our experiments show that the type of lipid domain selected to be stabilized depends sensitively on the properties of the pinning species. A similar phenomenon, albeit on a larger scale, was observed by crosslinking GM1 with cholera toxin B [Hammond et al., 2005; Lingwood et al., 2008]. Since the stabilized phase is determined by the properties of the pinning species, cells could locally sort their membrane components in this way. Moreover, this sorting mechanism persists to physiological temperatures, that is above the temperature of phase separation. At the same time, the pinning sites would naturally prevent the plasma membrane from phase separating at low temperatures. In the presence of curvature coupling, these effects are enhanced. We note that the proposed curvature effect in our experiments was likely limited by the Mica support. However, since the energy cost of lipid extraction far exceeds that of membrane de-adhesion from the support [Helm et al., 1991; Lipowsky and Seifert, 1991], we still expect some effect. In free-standing membranes, or in cell membranes, the curvature-coupling is anticipated to be stronger. The recent findings of Kaizuka and Groves [2010] seem to support this view.

## 5.5 Materials and methods

### 5.5.1 Preparation of Mica supported membranes

Mica (Muscovite, Pelco, Ted Pella, Inc., Redding, CA) was cleaved into thin layers ( $\sim 10 \mu\text{m}$ ) and glued (optical UV adhesive No. 88, Norland Products Inc., Cranbury, NJ) onto clean glass cover slides. Immediately before spin-coating the lipid solution, the Mica on top of the glass was cleaved again to yield a thin ( $\sim 1 \mu\text{m}$ ) and clean layer. Next, 30  $\mu\text{l}$  of 2 g/l lipid solution in Methanol/Chloroform (1:1) were spin-coated (2000 rpm, for 30 s) on top of the Mica. To remove residual solvent, the cover slide was put under vacuum for 20 min. The supported lipid bilayer was hydrated with warm (50°C) buffer (150 mM NaCl Tris pH 7.5) for 10 min and then rinsed several times to remove

excess membranes until a single clean bilayer remained on the surface. All lipids were purchased from Avanti Polar Lipids, Inc., AL USA. The Ld phase was stained with far-red fluorescent DPPE-KK114 [Kolmakov et al., 2010] or green fluorescent DPPE-OregonGreen-488 (Invitrogen, Darmstadt, Germany). The Lo phase was stained with DSPE-PEG(2000)-KK114 or DSPE-PEG(2000)-Cromeo-488 [Honigmann et al., 2013]. For imaging experiments, the concentration of fluorescent lipids was  $\sim 0.1$  mol%; for FCS experiments  $\sim 0.01$  mol% was used.

### 5.5.2 Actin binding to supported membranes

Supported lipid bilayers were doped with biotinylated lipids (1,2-dioleoyl-sn-glycero-3-phosphoethanolamine-N-(cap biotinyl) (DOPE-biotin), 1,2-dipalmitoyl-sn-glycero-3-phosphoethanolamine-N-(cap biotinyl) (DPPE-biotin), 1,2-distearoyl-sn-glycero-3-phosphoethanolamine-N-[biotinyl(polyethylene glycol)-2000] (DSPE-PEG-biotin), also purchased from Avanti) that were used to bind actin fibers to the membrane. The following procedure was performed at  $37^\circ\text{C}$  to keep the membrane in the one-phase region: The bilayer was incubated with  $200\ \mu\text{l}$  of  $0.1\ \text{g/l}$  streptavidin for 10 min and then rinsed several times to remove unbound streptavidin. Next, the membrane was incubated with  $200\ \mu\text{l}$  of  $1\ \mu\text{M}$  biotinylated phalloidin (Sigma-Aldrich, Steinheim, Germany) for 10 min and then rinsed several times to remove unbound phalloidin. Pre-polymerized actin fibers ( $500\ \mu\text{l}$  with  $7\ \mu\text{g/ml}$  actin; Cytoskeleton Inc., Denver, USA) were then incubated with the membrane for 20 min and then rinsed several times to remove unbound actin. In case actin fibers were imaged, the actin was stained with green fluorescent phalloidin (Cytoskeleton Inc.). The membrane bound actin network was stable for at least 24 hr. The density of the actin network was controlled by the amount of biotinylated lipids in the membrane (Fig. 5.1-supplement 2).

### 5.5.3 Simulation model

The local membrane height  $h(x, y)$  is a function of the lateral coordinates  $x$  and  $y$ , which are discretized on the sites of a  $L \times L$  periodic lattice,  $L = 400a$ , with lattice constant  $a = 2\ \text{nm}$ . The membrane elastic energy  $\mathcal{H}_{\text{Helfrich}} = \sum a^2 (\kappa(\nabla^2 h)^2 + \sigma(\nabla h)^2) / 2$ , with the sum over all lattice sites, and  $\nabla$  the gradient operator [Helfrich, 1973]. The first term is the bending energy; the second term reflects the cost of area deformations. We use typical values,  $\kappa \sim 2.7 \times 10^{-19}\ \text{Nm}$  and  $\sigma \sim 2 \times 10^{-5}\ \text{N/m}$ , at the same time emphasizing that there is a considerable spread in the reported values of these quantities [Schick,



2012]. This holds especially true for  $\sigma$ , whose value near a support may well be different. This, in turn, implies a large spread in the coupling to curvature strength [Schick, 2012]. As stated before, we adopt the approach keeping  $\kappa$  and  $\sigma$  fixed, while allowing the curvature coupling strength to vary. To describe phase separation, we introduce the local composition  $s(x, y)$ , which reflects the lipid composition at site  $(x, y)$ . Experiments indicate that phase separation in membranes (without actin) is compatible with the universality class of the Ising model [Magde et al., 1972; Honerkamp-Smith et al., 2009]. We therefore use a two-state description,  $s(x, y) = \pm 1$ , where the positive (negative) sign indicates that the site is occupied by a saturated (unsaturated) lipid, leading to  $\mathcal{H}_{\text{Ising}} = -J \sum s(x, y)s(x', y')$ , with the sum over all pairs of nearest-neighboring sites, and coupling constant  $J > 0$ . To match the phase transition temperature of the Ising model to the experiment [Machta et al., 2011], we choose  $J = 0.44k_{\text{B}}T_{\text{c}}$ , with  $T_{\text{c}} = (273 + 28)$  K the transition temperature of the membrane without actin, and  $k_{\text{B}}$  the Boltzmann constant. It has also been shown experimentally that the membrane height and composition are coupled via the local curvature [Baumgart et al., 2003; Yoon et al., 2006; Parthasarathy et al., 2006; Parthasarathy and Groves, 2007; Kaizuka and Groves, 2010]. This motivates the term  $\mathcal{H}_{\text{x}} = g \kappa \delta C a^2 \sum s \nabla^2 h$ , with the sum over all lattice sites,  $\delta C \sim 10^6 \text{ m}^{-1}$  the difference in the spontaneous curvature between Lo and Ld domains [Leibler and Andelman, 1987; Liu et al., 2005; Schick, 2012], and  $g > 0$  the dimensionless parameter introduced previously to reflect the fact that the model parameters are not known very precisely.

To include actin, a network of line segments (line thickness  $a$ ) was superimposed on the lattice, with a typical compartment size  $\sim 100$  nm, close to the experimental value (Fig. 5.1-supplement 2F). This network was the Voronoi tessellation of a random set of points [Machta et al., 2011; Ehrig et al., 2011a]. The network was fixed to the membrane via pinning sites, which were immobile, and distributed randomly along the fibers. The actin network and the pinning sites couple to both the composition and the membrane height. To realize the former, we replaced the composition variable at each pinning site by a fixed value  $s(x, y) = \text{Lo}\%/50 - 1$ , where Lo% is the partitioning fraction of the pinning lipid derived experimentally (Fig. 5.3-supplement 1). To couple the pinning sites to the membrane height, we imposed  $h(x, y) = 0$  at the pinning sites [Speck and Vink, 2012]. Additionally, we included a steric repulsion between the membrane and the actin fibers: lattice sites underneath an actin fiber have their corresponding height variable restricted to negative values.

#### 5.5.4 Monte Carlo simulation procedure

The model  $\mathcal{H}_{\text{sim}}$  was simulated using the Monte Carlo method. To compute the gradient and Laplace operators, standard finite-difference expressions were used. The simulations were performed at conserved order parameter, using equal numbers of saturated and unsaturated lipids. Two types of Monte Carlo move were used. The first was a Kawasaki move [Newman and Barkema, 1999], whereby two sites of different composition were chosen randomly, and then ‘swapped’. This move was accepted conform the Metropolis probability,  $P_{\text{acc}} = \min[1, e^{-\Delta\mathcal{H}_{\text{sim}}/k_{\text{B}}T}]$ , with  $\Delta\mathcal{H}_{\text{sim}}$  the energy difference,  $k_{\text{B}}$  the Boltzmann constant, and  $T$  the temperature. The second move was a height move, whereby a new height was proposed for a randomly selected site; this height was optimally selected from a Gaussian distribution, as explained by Speck and Vink [2012]. We emphasize that the moves were not applied to pinning sites. In addition, there is the steric repulsion constraint at sites that overlap with the actin network: for these sites, height moves proposing a positive value were rejected. Kawasaki and height moves were attempted with equal a priori probability, with production runs typically lasting  $2.10^6$  sweeps, prior of which the system was equilibrated for  $4.10^5$  sweeps (one sweep is defined as  $L^2$  attempted moves).

#### 5.5.5 Temperature control of the membrane

The temperature of the membrane and the surrounding buffer was controlled by a water cooled Peltier heat and cooling stage which was mounted on the microscope (Warner Instruments, Hamden, CT, USA). The achievable temperature range with this configuration was between 7 and 45°C, with a precision of 0.3°C. The actual temperature directly over the membrane was measured by a small thermo-sensor (P605, Pt100, Dostmann electronic GmbH, Wertheim-Reicholzheim, Germany).

#### 5.5.6 Microscopy

All experiments were performed on a confocal custom-built STED microscope whose main features are depicted in Fig. 5.1-supplement 4. The confocal unit of the STED nanoscope consisted of an excitation and detection beam path. Two fiber-coupled pulsed laser diode operating at  $\lambda_{\text{exc}} = 635$  nm and  $\lambda_{\text{exc}} = 485$  nm with a pulse length of 80 ps (LDH-P-635; PicoQuant, Berlin, Germany) were used for excitation of the green and far-red fluorescence, respectively. After leaving the fiber, the excitation beams were

expanded and focused into the sample using an oil immersion objective (HCXPLAPO 100x, NA = 1.4, Leica Microsystems). The fluorescence emitted by the sample was collected by the same objective lens and separated from the excitation light by a custom-designed dichroic mirror (AHF Analysentechnik, Tuebingen, Germany). In the following, the fluorescence was focused onto a multi-mode fiber splitter (Fiber Optic Network Technology, Surrey, Canada). The aperture of the fiber acted as a confocal pinhole of 0.78 of the diameter of the back-projected Airy disk. In addition, the fiber 50:50 split the fluorescence signal, which was then detected by two single-photon counting modules (APD, SPCM-AQR-13-FC, Perkin Elmer Optoelectronics, Fremont, CA). The detector signals were acquired by a single-photon-counting PC card (SPC 830, Becker&Hickl, Berlin, Germany). The confocal setup was extended by integrating a STED laser beam. A modelocked Titanium:Sapphire laser (Ti:Sa, MaiTai, Spectra-Physics, Mountain View, USA) acted as the STED laser emitting sub-picosecond pulses around  $\lambda_{\text{STED}} = 780$  nm with a repetition rate of 80 MHz. The pulses of the STED laser were stretched to 250 – 350 ps by dispersion in a SF6 glass rod of 50 cm length and a 120 m long polarization maintaining single-mode fiber (PMS, OZ Optics, Ontario, CA). After the fiber, the STED beam passed through a polymeric phase plate (RPC Photonics, Rochester, NY), which introduced a linear helical phase ramp  $0 \leq \Phi \leq 2\pi$  across the beam diameter. This wavefront modification gave rise to the doughnut-shaped focal intensity distribution featuring a central intensity zero. The temporal synchronization of the excitation and STED pulses was achieved by triggering the pulses of the excitation laser using the trigger signal from an internal photodiode inside the STED laser and a home-built electronic delay unit, which allowed a manual adjustment of the delay with a temporal resolution of 25 ps. The circular polarization of the STED and excitation laser light in the focal plane was maintained by a combination of a  $\lambda/2$  and  $\lambda/4$  retardation plates in both beam paths (B Halle, Berlin, Germany). Integration of a fast scanning unit enabled rapid scanning of the excitation and STED beam across the sample plane. A digital galvanometric two mirror-scanning unit (Yanus digital scan head; TILL Photonics, Gräfeling, Germany) was used for this purpose. The combination of an achromatic scan lens and a tube lens in a 4f-configuration ( $f = 50$  mm and  $f = 240$  mm, Leica, Wetzlar, Germany) realized a stationary beam position in the back aperture of the objective, preventing peripheral darkening within the focal plane at large scan ranges, such as vignetting. The maximal frequency of the Yanus scanner depended on the scan amplitude and varied between 2 and 6 kHz for scan amplitudes up to 150  $\mu\text{m}$ , respectively. The hardware and data acquisition was controlled by the software package ImSpector (<http://www.imspector.de/>).

### 5.5.7 Image analysis

To analyze the temperature-driven phase separation of the membrane (Fig. 5.1C), we calculated the cumulant  $U_1 = [x^2]/[|x|]^2$ , where the square brackets  $[\cdot]$  denote an average over all pixel values  $x$  in the image. The latter were normalized beforehand such that the mean  $[x] = 0$  and the standard deviation  $[x^2] - [x]^2 = 1$ . The average domain size  $R$  (Fig. 5.1D) was extracted from the radial distribution function  $g(r)$  of the lipid intensity image, which represents the intensity correlations between two points of distance  $r$ . We observed that  $g(r)$  was largest at  $r = 0$ , and decayed for  $r > 0$ . As a measure of the domain size  $R$ , we used the criterion  $g(R) = 0.5 \times g(0)$ . The Pearson correlation coefficient (PCC) between the actin and the lipid channels (Fig. 5.1E) was calculated as the covariance of both channels divided by the product of the standard deviations of both channels. For each temperature up to 5 images from different parts of the sample were analyzed. Vesicles on top of the supported bilayer (which were visible in the lipid channel as round bright structures) were excluded from the analysis.

### 5.5.8 Scanning FCS and pair-correlation analysis

For the analysis of Fig. 5.2, circular orbits 0.5 – 1.2  $\mu\text{m}$  in diameter were scanned, at scanning frequency 4 kHz. The scanning orbit was subdivided into 64 pixels. For each pixel  $i$ , the fluorescence intensity  $F_i(t)$  was recorded as a function of time  $t$  for a duration of 30 – 60s. The correlation between two pixels,  $i$  and  $j$ , was computed via the pair-correlation function (PCF)  $G_{ij}(\tau) = \langle F_i(t)F_j(t + \tau) \rangle / \langle F_i(t) \rangle \langle F_j(t) \rangle - 1$ , where  $\langle \cdot \rangle$  denotes a time average. Fig. 5.2A,C shows the autocorrelation ( $i = j$ ) of each pixel along the orbit, whereas Fig. 5.2B,D shows the correlation between pairs of pixels  $i$  and  $j$  separated by a rotation of 180°. The maximum of the PCF yields an estimate of how long the fluorescent probes on average need to diffuse from  $i$  to  $j$  [Digman and Gratton, 2009]. To avoid crosstalk between the two excitation spots, the distance between pairs (i.e., the diameter of the scanning orbit) was at least twice the size of the observation spot. In case of free Brownian diffusion, the PCF is homogenous around the scan orbit. In case the diffusion is hindered by obstacles, the maximum of the PCF is shifted to longer times, and its amplitude is decreased.

## **Acknowledgments**

We thank Vladimir Belov and Gyuzel Mitronova (MPI Göttingen) for the synthesis of the fluorescent lipid analogous, and Marcus Müller (Institute of Theoretical Physics, University of Göttingen) for stimulating discussions.

## **5.6 Appendix: Supplementary Figures**

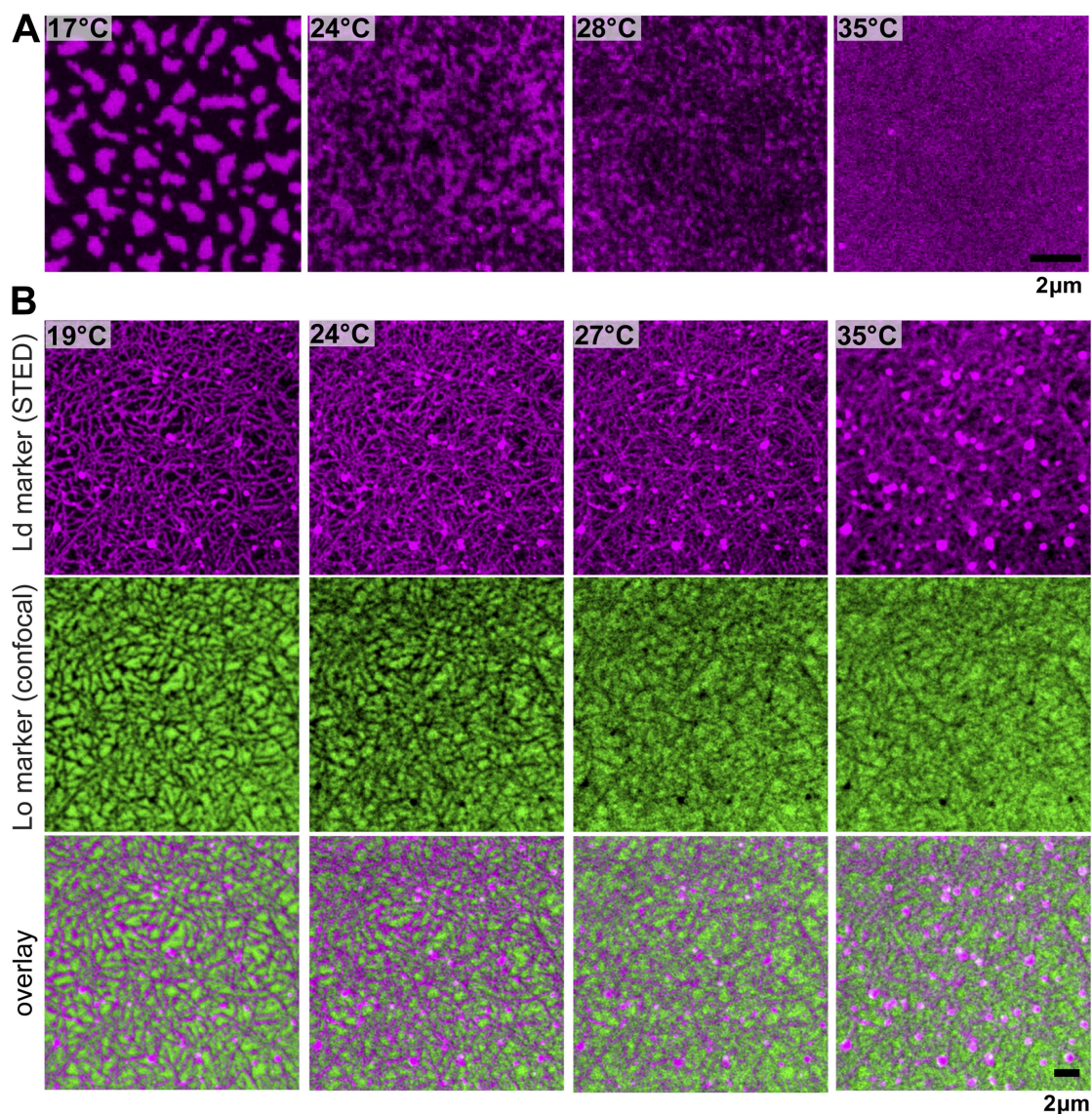


**Figure 5.1-supplement 1:** Phase organization by the actin network. Simultaneous confocal and STED images of a fluorescent lipid preferring the Lo (DSPE-PEG-Chromeo488, green, Lo-marker) and Ld phase (DPPE-KK114, red, Ld-marker), respectively. The membrane has the same composition as in Fig. 5.1 without staining the actin network, confirming a negligible influence of the green fluorescent phalloidin actin-marker. (A) Without actin, the Ld-marker reveals the typical phase separating behavior: below  $T_c$  domains coarsen, while above  $T_c$  the membrane is homogenous ( $T_c \approx 28^\circ\text{C}$ ). (B) After actin binding to DOPE-biotin, Ld domains form a meshwork-like structure, similar to Fig. 5.1B. The Lo domains form an inverse pattern, that is compartments separated by the Ld meshwork. As in Fig. 5.1, the mosaic pattern persists above the phase transition temperature  $T_c$  of the membrane without actin.

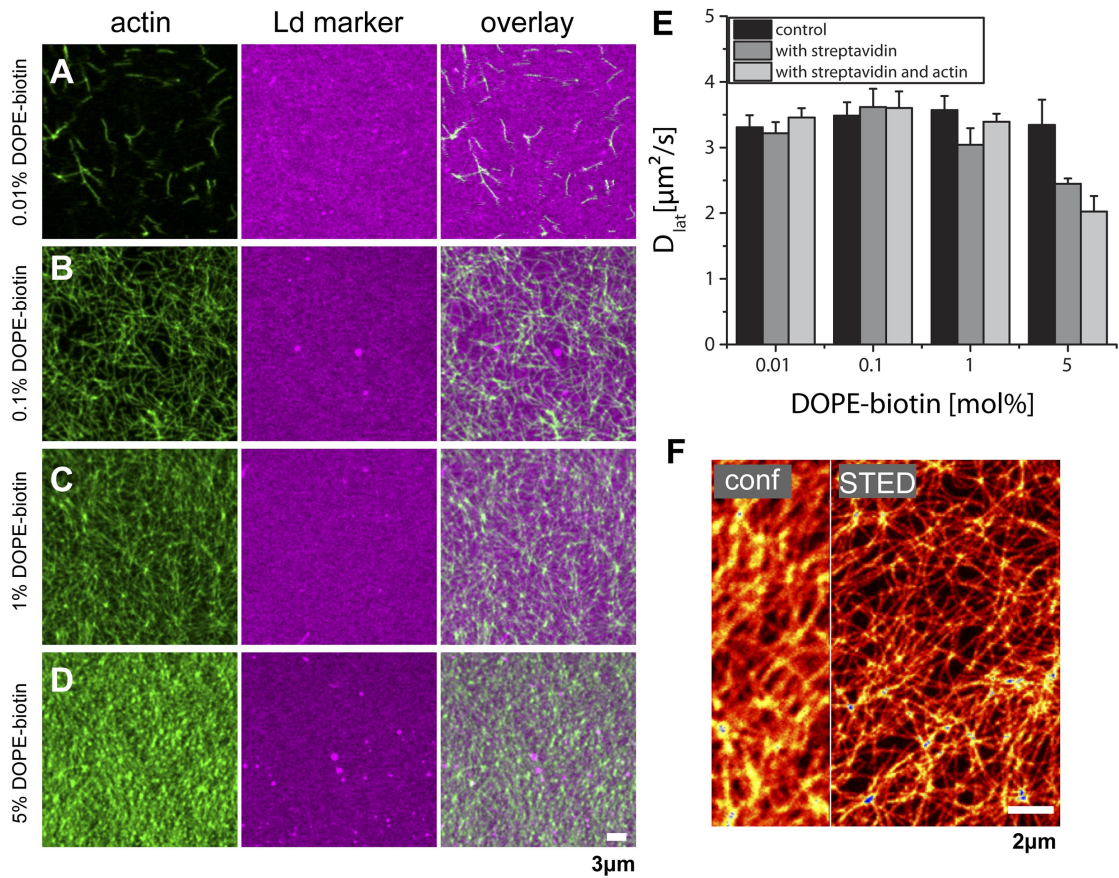


**Figure 5.1-supplement 2:** Actin network density and lipid diffusion dependence on the concentration of biotinylated lipids. The data refer to a single lipid species (DOPC) supported bilayer at  $T = 22^\circ\text{C}$ . (**A–D**) Images of actin binding for increasing concentrations of DOPE-biotin (as marked on the left) using fluorescence markers phalloidin-488 for actin and DPPE-KK114 for the Ld phase. As expected, the actin network density increases with the number of binding sites in the membrane. In contrast to ternary membranes (Fig. 5.1), the Ld-marker distribution remains homogeneous. (**E**) Measurements of the lateral diffusion constant  $D$  of DPPE-KK114 (Ld-marker) determined with FCS. For increasing concentrations of DOPE-biotin, the diffusion constant was determined before the addition of streptavidin (control), after the addition of streptavidin (with streptavidin), and after the subsequent addition of actin (i.e., with streptavidin and actin). No change in diffusion was detected after actin binding for DOPE-biotin concentrations up to 1 mol%. Only for very high concentrations (5 mol%) could a decrease ( $\sim 30\%$ ) in lateral diffusion be detected. (**F**) STED image of the actin network at a binding site concentration of 1 mol% DOPE-biotin (actin was stained with Alexa633-phalloidin). The network can be clearly resolved by STED. Compartment sizes are between 60 nm and 500 nm with a peak at 120 nm.

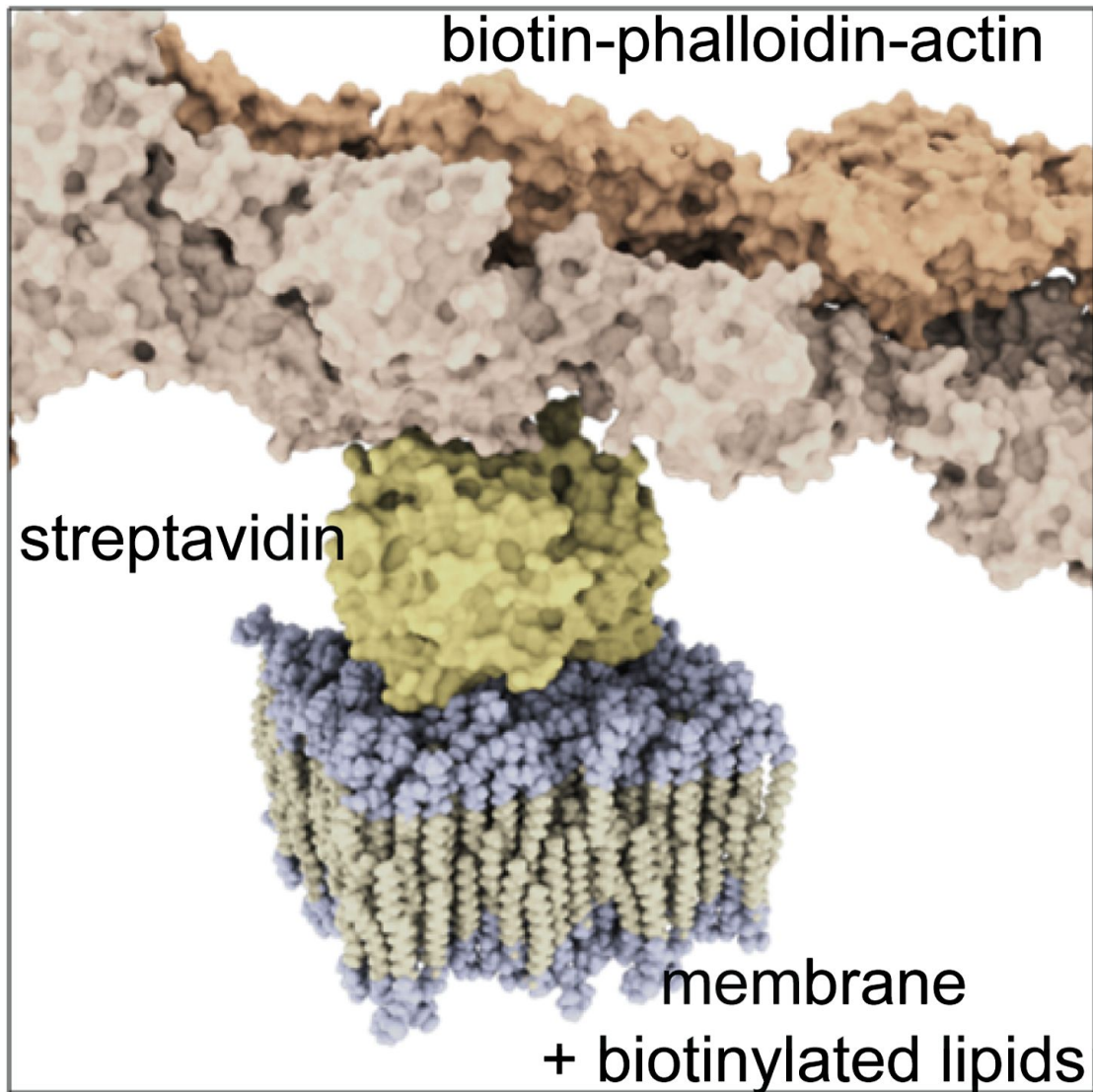


**Figure 5.1-supplement 3:** Molecular sketch of the assembled components in our model system.



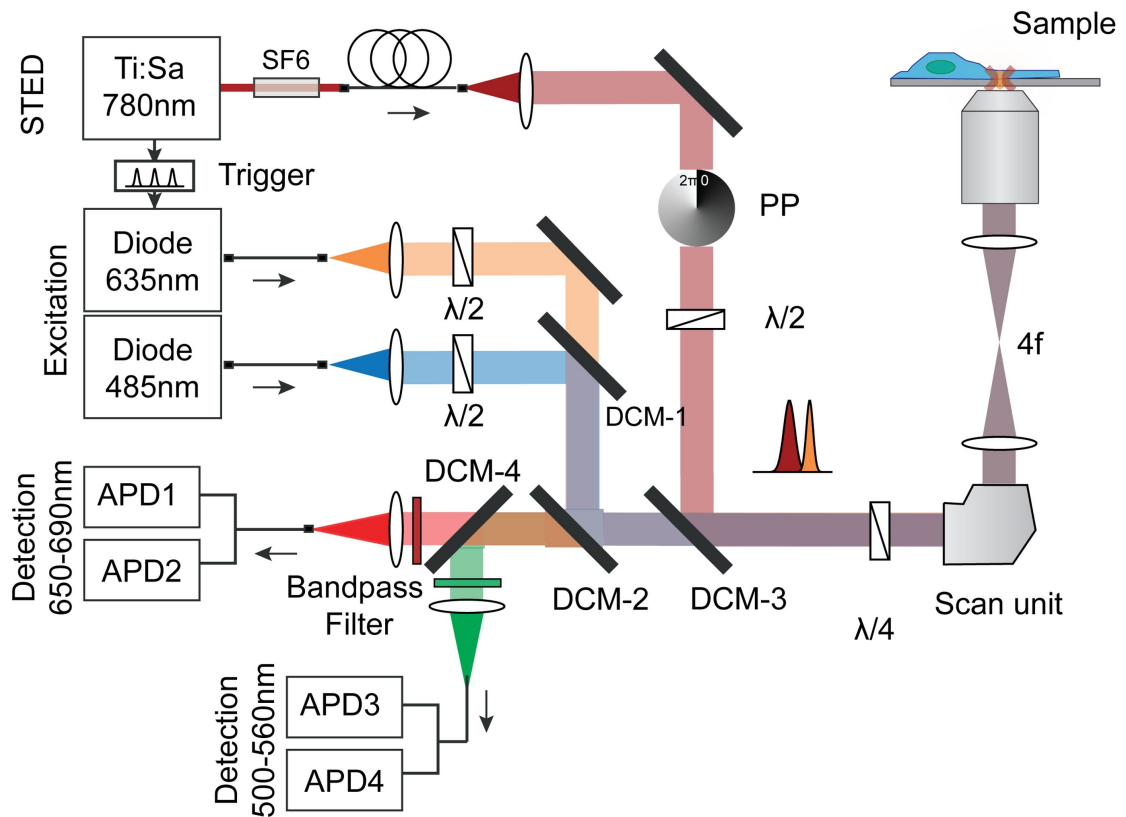


**Figure 5.1-supplement 4:** Optical setup for STED imaging and scanning FCS with pulsed excitation and pulsed STED laser and according beam paths (excitation orange/blue and STED dark red). The repetition rates of the three lasers were synchronized using an electronic trigger box. The laser beams were overlaid using three dichroic mirrors and focused into the sample. The emitted fluorescence (red/green) from the sample was split with a dichroic mirror and cleaned using bandpass filters and detected using four fiber-coupled avalanche photon detectors (APD). Each fluorescence channel was imaged onto the input of a 50:50 splitting fiber, serving as the confocal pinhole. The polymeric phase plate (PP) induced a clockwise  $2\pi$ -phase shift across the STED beam, which generated the doughnut shaped intensity distribution in the focal plane. Note, that the circular polarization of all laser beams is maintained by a combination of  $\lambda/2$  and  $\lambda/4$  waveplates. The STED laser was further sent through SF6 glass rods (SF6) and a 120 m long polarization maintaining single-mode fiber (PMS) for stretching of the pulses and mode cleaning.

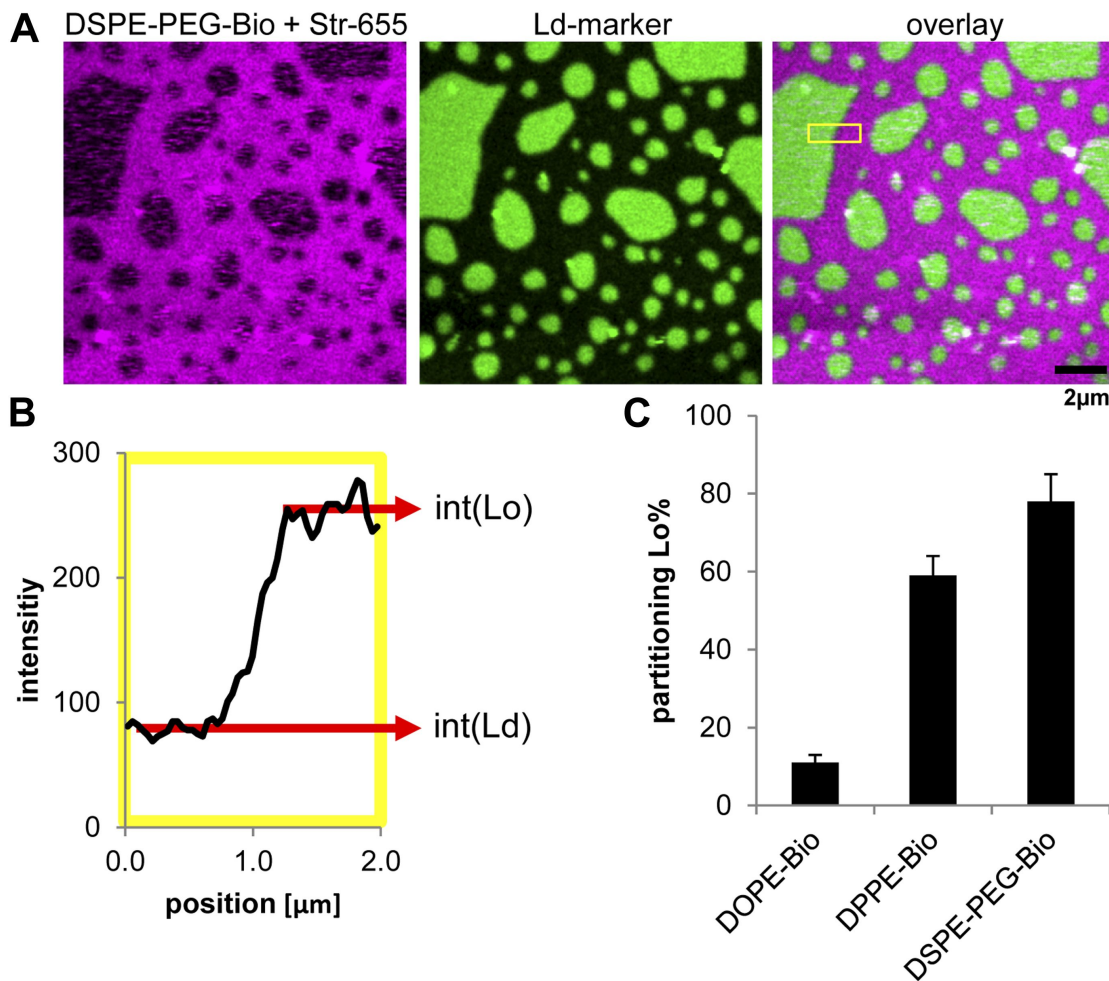


**Figure 5.3-supplement 1:** Lipid phase partitioning of biotinylated lipid-streptavidin complexes without actin. **(A)** Exemplary image of a phase separated membrane (DOPC, DPPC, Cholesterol) containing 1 mol% DSPE-PEG-biotin, and the green fluorescent Ld-marker (DOPE-fluorescein; Avanti polar lipids Inc.). The biotinylated lipid was labeled by streptavidin stained with red fluorescent Atto655 (Atto-Tec GmbH, Germany). **(B)** The partitioning of the biotinylated lipid-streptavidin complex was calculated by determining the intensity of red fluorescence in the Lo phase (int[Lo]) and in the Ld phase (int[Ld]) across a domain boundary. The scan in **(B)** corresponds to the yellow box in the overlay image. The partitioning is defined as  $\text{Lo}\% = 100\% \times \text{int}[\text{Lo}] / (\text{int}[\text{Lo}] + \text{int}[\text{Ld}])$ . **(C)** The resulting Lo% partitioning values for the biotinylated lipids used in this study with standard variation from three independent preparations. The partitioning values serve as input parameters for our simulation model.

## Chapter 6

# Membrane sorting via the extracellular matrix

Sina Sadeghi and Richard L. C. Vink (2014),  
BBA Biomembrane, 1848(2):527.

Published 8 November 2014.

DOI: [10.1016/j.bbamem.2014.10.035](https://doi.org/10.1016/j.bbamem.2014.10.035)

The manuscript describes a study of pattern formation in lipid membranes due to extracellular components. The study was designed by Richard Vink and me. I performed all simulations (including from-scratch code writing), data acquisition, and data analysis. The manuscript was written by me with revisions from Richard Vink.

## Abstract

We consider the coupling between a membrane and the extracellular matrix. Computer simulations demonstrate that the latter coupling is able to sort lipids. It is assumed that membranes are elastic manifolds, and that this manifold is disrupted by the extracellular matrix. For a solid-supported membrane with an actin network on top, regions of positive curvature are induced below the actin fibers. A similar mechanism is conceivable by assuming that the proteins which connect the cytoskeleton to the membrane induce local membrane curvature. The regions of non-zero curvature exist irrespective of any phase transition the lipids themselves may undergo. For lipids that prefer certain curvature, the extracellular matrix thus provides a spatial template for the resulting lateral domain structure of the membrane.

## 6.1 Introduction

Ever since the lipid raft hypothesis [Simons and Ikonen, 1997], the lateral organization of membranes has been intensely studied. Much has been learned from model membranes, in which the number of lipid species is strongly reduced compared to their biological counterparts, enabling detailed and systematic investigations [Dietrich et al., 2001; Simons and Vaz, 2004]. The hope is that a good understanding of the model system will also provide valuable insight into biological membranes.

Investigations of model membranes have established one fact beyond any doubt, namely the occurrence of phase transitions in these systems. For example, ternary membrane mixtures containing saturated lipids, unsaturated lipids, and cholesterol, demix into two fluid phases upon lowering the temperature [Veatch and Keller, 2002]. Furthermore, in single component membranes, there exists the main transition, between a phase where the lipid tails are ordered, and one where the tails are disordered [Nagle, 1980; Charrier and Thibaudau, 2005]. Consequently, it is tempting to assume that phase transitions play a key role in biological membranes as well [Veatch and Keller, 2005; Levental et al., 2009]. Of course, a minimal condition for this hypothesis is that all biological membranes operate at conditions that are close to phase transitions. Given the enormous diversity in membrane compositions between cells, different “body” temperatures between species, coupling of the membrane to active processes in the cell cortex [Mayor and Rao, 2004], an intriguing mechanism must have evolved to keep the membrane “tuned” to the vicinity

of a phase transition. While such a mechanism may well exist, its details remain elusive to this day.

The purpose of this paper is to highlight that phase transitions are not the only means to bring about lateral organization in biological membranes. In our view, a key difference between biological and model membranes is the presence of an extracellular matrix in the former: A biological membrane is not free, but instead intricately connected to its environment, for example, to the cytoskeleton network. As we will show for a very simple model, the mere connection to the environment is already sufficient to induce lateral organization. Our model is inspired by a recent experiment of a (model) membrane “sandwiched” between a substrate and an actin network [Honigmann et al., 2014]. This experiment revealed a lateral domain structure in the membrane that was strongly correlated to the actin fibers. We will show here how the interplay between the substrate, the actin network, and the membrane elastic properties already provides a “template” for this structure, i.e., completely independent of any phase transition the lipids may exhibit. Next, we consider how such a mechanism could manifest itself in situations where a substrate is absent, but where the proteins that connect the cytoskeleton to the membrane induce local membrane curvature. Our proposed mechanisms are in line with recent studies that also indicate the importance of the cytoskeleton in bringing about lateral organization, such as the formation of protein-lipid complexes [Gómez-Llobregat et al., 2013], and GPI-anchored protein clusters [Goswami et al., 2008]. In addition, the coupling to the cytoskeleton induces spatial confinement, which affects the spectrum of membrane height fluctuations [Gov and Safran, 2004; Farago, 2008, 2011], as well as protein diffusion [Kusumi et al., 2005; Lin and Brown, 2005].

## 6.2 Model and method

Our membrane model is defined on a two-dimensional (2D)  $L \times L$  periodic square lattice. To describe the out-of-plane height deformations, each lattice site  $i$  is given a real number  $h_i$  to denote the local membrane height (Monge representation). We consider a membrane that strongly interacts with its environment. This interaction, for instance with the solid substrate or the cytoskeleton network, will typically constrain the membrane height fluctuations. In general, the free energy of the system is given by

$$\mathcal{H} = \frac{\kappa a^2}{2} \sum_i (\nabla^2 h_i)^2 + \mathcal{H}_{\text{env}} \quad , \quad (6.1)$$

where  $a$  is the lattice spacing, and the sum is over all lattice sites. The first term in Eq. (6.1) is the elastic energy of the membrane, given in lowest order of the Helfrich expansion with  $\kappa$  the bending modulus [Helfrich, 1973]. On the lattice, the Laplacian is expressed using the standard finite-difference expression [Weikl et al., 2002]. The second term  $\mathcal{H}_{\text{env}}$  describes the membrane-environment interaction, and needs to be defined explicitly for the case of interest.

We perform Monte Carlo (MC) to simulate Eq. (6.1). The MC move is to update the height of a randomly selected lattice site. To this end, we propose a new height for the chosen site and accept it with the Metropolis probability,  $P_{\text{acc}} = \min[1, e^{-\beta\Delta\mathcal{H}}]$ , where  $\beta = 1/k_{\text{B}}T$  with  $k_{\text{B}}$  as the Boltzmann constant,  $T$  as the temperature, and  $\Delta\mathcal{H}$  as the free energy difference computed according to Eq. (6.1). For a free energy  $\mathcal{H}$  that is quadratic in the height,  $\sim \sum_i (A_i h_i^2 + B_i h_i)$ , one can optimally propose the new height to the chosen site  $i$  from a Gaussian distribution with mean  $-B_i/2A_i$  and variance  $k_{\text{B}}T/2A_i$  [Speck and Vink, 2012], which is how the present simulations are performed.

## 6.3 Results

### 6.3.1 Membrane “sandwiched” between a solid substrate and an actin network

We first consider a solid-supported membrane bound to an actin network, which resembles the situation addressed experimentally by Honigsmann et al. [2014]. In this case, the interaction potential in Eq. (6.1) is given by

$$\mathcal{H}_{\text{env}} = \mathcal{H}_{\text{sub}} + \mathcal{H}_{\text{act}} \quad , \quad (6.2)$$

where the first term describes the interaction of the membrane with the solid support, and the second term describes the influence of the actin network.

Solid-supported membranes are separated from the substrate by an ultra-thin hydration layer typically 1 nm thick. Consequently, the membrane-substrate interaction is a strong one [Lipowsky, 1995; Sackmann, 1996; Seifert, 1997; Salditt, 2005]. It can be expressed as a superposition of repulsive hydration (steric) and attractive van der Waals forces [Rädler et al., 1995]. This typically results in a membrane-substrate interaction featuring a minimum some distance above the support. We expand up to quadratic order around

the minimum, leading to

$$\mathcal{H}_{\text{sub}} = \frac{\alpha a^2}{2} \sum_i h_i^2 \quad , \quad (6.3)$$

where  $\alpha$  is the strength of the harmonic potential [Speck et al., 2010; Reister et al., 2011]. For simplicity, the minimum of the harmonic potential is set to  $h = 0$ , which we take as the reference from which the membrane height variables  $h_i$  are measured. We emphasize that by using a harmonic potential, the free energy Eq. (6.1) remains quadratic in  $h_i$  and so we can use the Gaussian distribution method of Speck and Vink [2012] to optimally propose new height variables during the MC simulations.

Next, we describe the effect of the actin term  $\mathcal{H}_{\text{act}}$ . In the experiment of Honigmann et al. [2014], an actin network is deposited on top of the supported membrane, i.e., the membrane is “sandwiched” between the substrate and the actin network. In experiments [Machta et al., 2011; Honigmann et al., 2014], actin is bound to the membrane via cross-linker molecules, such as streptavidin, referred to as *pinning sites* in what follows. The pinning sites are immobilized obstacles randomly distributed along the actin fibers. In line with previous simulations [Machta et al., 2011; Ehrig et al., 2011a; Honigmann et al., 2014], we represent the actin network by a Voronoi diagram obtained from a set of random points. The thickness of the actin fibers is one lattice site, the typical compartment size is chosen to be  $\sim 100$  nm. The resulting Voronoi diagram is then superimposed on the lattice of height variables. Next, we place the pinning sites, at randomly selected points along the edges of the Voronoi diagram. Once put in place, the pinning sites remain fixed, i.e., they cannot diffuse along the actin fibers. We assume that the effect of a pinning site is to locally push the membrane down, i.e., away from the reference height  $h = 0$  toward negative values. We incorporate this effect into our simulations by fixing the height variable at each pinning site to a negative value  $h_P < 0$  (for simplicity, the same value  $h_P$  is used for all the pinning sites). During the simulations, MC moves are thus *not* applied to pinning sites. Since Eq. (6.3) is a quadratic expansion, our analysis is restricted to small values of  $h_P$ . An extreme upper bound is the thickness of the hydration layer  $\sim 10$  Å, which is the maximum distance the membrane can be pushed down, and where Eq. (6.3) certainly breaks down. For this reason, in the analysis to be presented, we restrict  $h_P$  to several Å at most.

We simulate a system of size  $L = 400$  with lattice spacing  $a = 2$  nm. For the presented results, we use a typical value  $\beta\kappa = 70$  for the bending rigidity [Speck et al., 2010; Schick, 2012]. At room temperature,  $T = 300$  K, this corresponds to  $\kappa = 2.9 \times 10^{-19}$  Nm, which is close to the value used by Honigmann et al. [2014]. Fig. 6.1 shows a snapshot of the

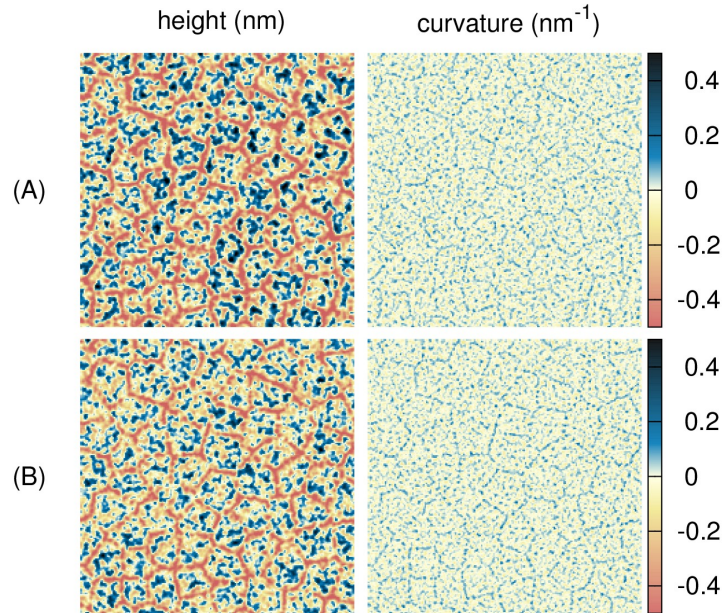


**Figure 6.1:** Typical snapshots of the thermally averaged height and curvature profiles of the solid-supported membrane bound to an actin network, in units of nm and  $\text{nm}^{-1}$ , respectively. The strength of harmonic potential is given  $\beta\alpha a^4 = 2$  and 4 for (A) and (B), respectively. In both cases, the pinning fraction is 25% of entire actin network and the pinning deviation height  $h_P = -6 \text{ \AA}$ .

membrane, color-coded according to the thermally averaged height (left) and curvature (right). In both cases 25% of the actin network is covered by pinning sites. Results are presented for two values of the strength of the harmonic potential,  $\beta\alpha a^4 = 2$  (A) and  $\beta\alpha a^4 = 4$  (B). The reported values of  $\alpha$  in literature cover quite a wide range [Speck et al., 2010; Reister et al., 2011; Speck and Vink, 2012]. Our results use values comparable to  $k_B T$  [Speck and Vink, 2012]. The deviation from the reference height at the pinning sites is set as  $h_P = -6 \text{ \AA}$ . The simulations ran for  $4 \times 10^6$  sweeps, after having been equilibrated for  $4 \times 10^5$  sweeps (each sweep is  $L^2$  attempted MC moves).

As can be seen from height and curvature profiles, the actin pattern is clearly “pressed” onto the membrane. In particular, in the curvature snapshots, one can see that along the actin fibers an on-average positive curvature has been induced. This effect persists even at low fractions of pinning sites. To quantify this, we measured the cross correlation between the curvature snapshot  $\mathbf{c}$  and the actin network  $\mathbf{a}$  using the Pearson correlation coefficient (PCC). The advantage of using this quantity is that it can also be measured in experiments via fluorescence spectroscopy [Honigmann et al., 2014]. The PCC is defined



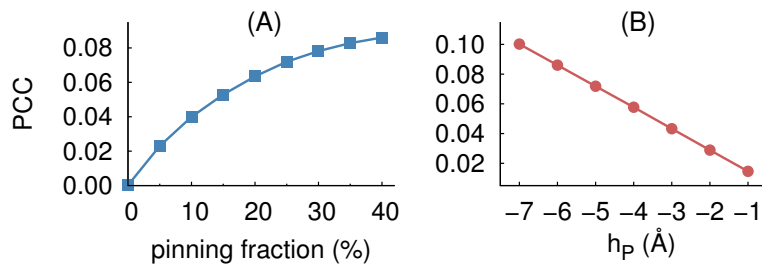


**Figure 6.2:** (A) The variation of the Pearson correlation coefficient (PCC) with the pinning fraction for  $h_P = -6$  Å. (B) PCC versus  $h_P$  for pinning fraction of 40%. In both plots, the strength of the harmonic potential  $\beta\alpha a^4 = 4$ .

as

$$\text{PCC} = \frac{\sum_i (c_i - \bar{c})(a_i - \bar{a})}{\sqrt{\sum_i (c_i - \bar{c})^2} \sqrt{\sum_i (a_i - \bar{a})^2}}, \quad (6.4)$$

where  $\bar{c}$  and  $\bar{a}$  are the mean “pixel” values of the curvature and actin images, and the sum over all lattice sites (for the actin image,  $\mathbf{a}_i$  is zero everywhere except at sites that intersect with an edge of the Voronoi network, for which  $\mathbf{a}_i = 1$ ). A positive (negative) value of PCC means that the curvature is positive (negative) on average underneath the actin fibers, while a value of zero means there is no correlation.

Fig. 6.2A shows how PCC varies with the pinning fraction, using  $h_P = -6$  Å. The PCC initially increases linearly from zero with the pinning fraction. In the linear regime, the pinning sites are isolated from each other. Each pinning site thus contributes to the PCC by the same amount, which explains the linear increase. At larger pinning fractions, the pinning sites are no longer isolated, i.e., their “regions of influence” begin to overlap, which explains the downward curvature in the data. The effect of the pinning height  $h_P$  is shown in Fig. 6.2B for a pinning fraction of 40%: By pushing the membrane further down, PCC increases.

For a solid-supported membrane with an actin network “on-top”, these results suggest a mechanism for lateral domain formation in membranes that does not require any phase separation between lipids. The pinning sites along the actin fibers locally push the membrane down, leading to non-zero average curvature below the fibers. Consider now a lipid mixture, with one of the lipid species preferring regions of, say, positive curvature (the coupling between membrane composition and curvature is an established fact [Leibler and Andelman, 1987; Liu et al., 2005; Parthasarathy et al., 2006; Parthasarathy and Groves, 2007; Schick, 2012; Shlomovitz and Schick, 2013]). In the upper membrane leaflet, these lipids would then preferentially collect underneath the actin fibers, since

there the curvature has the correct sign. In contrast, in the lower leaflet where the curvature sign is reversed, these lipids would be repelled from the fibers. Hence, a domain pattern (in this case anti-correlated between the two leaflets) can be induced purely by the coupling between the local membrane curvature and the curvature preferred by a single lipid species. This pattern is independent of the energetic interaction between the lipids, i.e., it does not require the lipid mixture to be close to any demixing phase transition. We emphasize that the formation of anti-correlated domains requires the composition to be the same in both leaflets [Schick, 2012]. In case this condition is not met, the coupling between the leaflets is more complex, and also correlated domains are possible [Shlomovitz and Schick, 2013].

### 6.3.2 Pinning sites that induce local membrane curvature

We now argue that a similar mechanism as proposed above for a solid-supported membrane could persist in the absence of a substrate also. This mechanism is based on the observation that proteins associated with actin can be curved, owing to their geometry (examples include IMD [Mattila et al., 2007] and IRSp53 [Scita et al., 2008] proteins). In our model, this effect can be incorporated by assuming that the pinning sites induce a non-zero local membrane curvature, say, of value  $C_p$ . Within this framework, the Helfrich bending energy reads as

$$\mathcal{H}_{\text{bend}} = \frac{\kappa a^2}{2} \sum_i (\nabla^2 h_i - C_p \delta_i)^2 \quad , \quad (6.5)$$

where  $\delta_i = 1$  in case lattice site  $i$  is a pinning site, and zero otherwise. Expanding the square (and dropping an irrelevant constant), one obtains Eq. (6.1) with

$$\mathcal{H}_{\text{env}} = -\kappa C_p a^2 \sum_i (\nabla^2 h_i) \delta_i \quad , \quad (6.6)$$

which describes the effect of the pinning sites [Leibler and Andelman, 1987]. In the previous model for the solid-supported membrane, the pinning sites were assumed to locally push the membrane down. In the present model, they are assumed to induce local membrane curvature. The model, as before, is readily simulated using our MC procedure. We emphasize that since the free energy remains quadratic, one can still use the Gaussian distribution to optimally propose new height values [Speck and Vink, 2012]. In contrast to the solid-supported membrane, the MC moves in the present model are applied to all lattice sites.

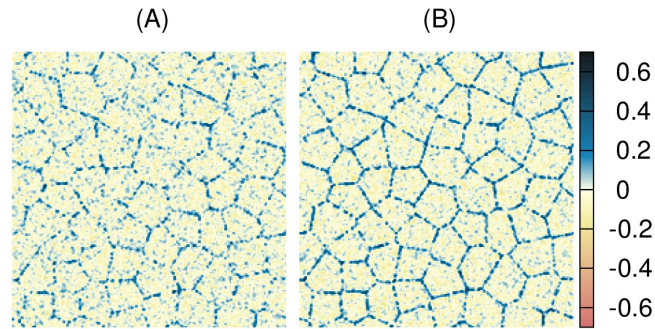


**Figure 6.3:** Typical snapshots of the thermally averaged curvature profile for the membrane model of Eq. (6.5), where the pinning sites induce local membrane curvature. The pinning fractions are 25% (**A**) and 40% (**B**) of the entire actin network. The curvature radius of the pinning sites is set as  $C_P^{-1} = 2$  nm in both cases.

Fig. 6.3 shows typical snapshots of the thermally averaged curvature values obtained for the model of Eq. (6.5). The curvature radius of the pinning sites is set as  $C_P^{-1} = 2$  nm in both cases [Zimmerberg and Kozlov, 2005; Sorre et al., 2012]. The snapshots correspond to pinning fraction 25% and 40% of the entire actin network, for (A) and (B), respectively. The correlation between the positively curved regions and the actin fibers increases as the pinning fraction increases. This is manifested by the PCC, shown in Fig. 6.4A. Note that the PCC values significantly exceed those of Fig. 6.2A. As might be expected, pinning sites that directly impose local membrane curvature are more efficient at imprinting a curvature pattern than pinning sites that couple to the membrane height. We also measured the PCC as a function of the curvature radius of the pinning sites  $C_P^{-1}$ , see Fig. 6.4B. As can be seen, by increasing the curvature radius of the pinning sites, the PCC decreases. This is to be expected since the limit  $C_P \rightarrow 0$  describes pinning sites that prefer the membrane to be locally flat.

Hence, also in this case, a lateral domain pattern may already be “imprinted” via the coupling of the membrane to the actin network. The preferred local membrane curvature “stamped” onto the membrane sheet by the pinning sites induces regions that are favorable for lipids of matching spontaneous curvature. As in the case of the solid-supported membrane, this provides a mechanism of sorting lipids via curvature, and which does not require the lipids to be near a demixing transition.

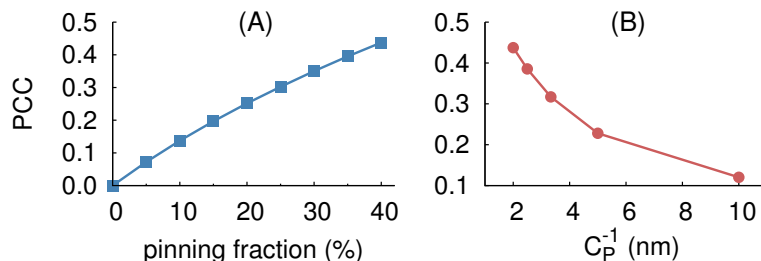


**Figure 6.4:** Pearson correlation coefficient (PCC) for the membrane model of Eq. (6.5). (A) PCC vs. pinning fraction for  $C_p^{-1} = 2$  nm. (B) PCC vs. the curvature radius of the pinning sites at pinning fraction of 40%.

## 6.4 Discussion

In this paper, we have proposed an alternative mechanism able to sort lipids in membranes. The mechanism is based on the fact that membranes are elastic manifolds, and that this manifold is disrupted by the presence of the extracellular matrix. In the case of a solid-supported membrane with an actin network “on-top”, MC simulations reveal that regions of positive curvature are induced underneath the actin fibers. A similar mechanism is conceivable by assuming that the proteins which connect the cytoskeleton to the membrane, induce local non-zero curvature. The regions of non-zero curvature exist irrespective of any phase transition the lipids themselves may undergo. Hence, even for a lipid mixture at high temperature, i.e., above the temperature of phase separation, lipid sorting can still take place provided that the lipid species have different affinities to curvature. In the presented models, lipids that prefer positive curvature would collect underneath the actin strands.

In realistic situations, there will be an interplay between the proposed curvature mechanism and other mechanisms. For example, it could be that the pinning sites also energetically attract certain lipid species, for instance, via electrostatic interactions. The species that is attracted energetically need not be the same as the species preferred by curvature. In this case, the resulting lipid domain structure is determined by the relative strength of each source of attraction. Recent experiments suggest that such an interplay indeed occurs [Honigmann et al., 2014]. In this experiment, a ternary membrane mixture containing saturated/unsaturated lipids and cholesterol was used. The membrane was connected to an actin network via pinning sites, and the energetic attraction of the pinning sites could be controlled. For pinning sites that weakly attract saturated lipids, nevertheless a small excess of unsaturated lipids along the actin fibers

was observed. This result shows that other mechanisms, beyond the energetic attraction between lipids and pinning sites, are at work that determine the lateral domain structure. Computer simulations in which the energetic and curvature attractions are both included are indeed able to reproduce the experimental results [Honigmann et al., 2014].

In view of raft formation, the coupling between membrane lipid composition and local curvature is currently attracting much attention [Schick, 2012; Shlomovitz and Schick, 2013; Meinhardt et al., 2013]. It has been shown that such a coupling is able to induce composition fluctuations on a length scale of 10 – 100 nm, which is compatible with the size of rafts. In combination with the coupling to the extracellular matrix presented in this paper, this mechanism can be extended, providing cells with a means to control the spatial location where rafts are formed (for instance, underneath actin strands). A further interesting extension would be to include the role of active processes in the cell cortex, such that the positions of the pinning sites become time-dependent. In this situation, there can even be a feedback between the local membrane curvature due to curved proteins that are associated with the actin, and the recruitment of actin [Gov and Gopinathan, 2006; Veksler and Gov, 2007].

## Acknowledgments

This work was supported by the *Deutsche Forschungsgemeinschaft* within the collaborative research center SFB-937 *Collective Behavior of Soft and Biological Matter* (project A6), and the Emmy Noether program (VI 483).

# Chapter 7

## Summary

In this thesis, we studied phase transitions and domain formation in lipid membranes. The lateral heterogeneity in the plasma membranes of eukaryotic cells is an important factor for regulating many biological functions. Ever since the postulation of the lipid raft hypothesis, understanding the lateral structure of lipid bilayer membranes has received an enormous interest. As opposed to plasma membranes, model membranes (either artificially prepared membranes, or membranes extracted from living cells) typically phase separate. To address this paradox, we presented a detailed investigation of phase behaviour of model membranes via computer simulations. To this end, we probed the phase behaviour of membrane models that undergo macroscopic phase separation at low temperature. We furthermore considered the effect of quenched disorder on the phase separation in model membranes in order to answer why those small domains do not coalesce. Additionally, we studied the effect of curvature on the phase behaviour of lipid membranes, considering a curvature-composition coupling.

In the first attempt, we performed Monte Carlo simulations of the multi-state single-component Pink model to address a variety of problems for the phase behaviour of lipid mono- and bilayers. To this end, we employed a careful finite-size scaling method and calculated the critical temperatures for three different lipid species. This enabled us to point out that the 10-state Pink model is in the universality class of the 2D Ising model. It also nicely resolved the problem found in previous studies in which no phase transition had been reported for this model. The significance of this work is to emphasize the importance of finite-size scaling in the analysis of the phase transition. The systematic investigation of the finite-size effects on the phase behaviour of the biological systems is not yet standard in biophysics. Hence, this work provided an

extremely useful step toward further investigation of the phase behaviour of membrane models. Moreover, as an example we studied the effect of quenched disorder (pinning sites) on the phase separation of a solid-supported membrane. The pinning sites may be present in the membrane due to the surface roughness of the substrate. We concluded that the introduction of the pinning sites results in removing the phase transition and creating a multi-domain state. In fact, the presence of quenched disorder alters the phase behaviour of the membrane and changes it toward the one of the 2D random Ising model which has no phase transition in thermodynamic limit. The biological relevance is that quenched disorder in plasma membranes can prevent macroscopic phase separation, thus offering a possible explanation for the *in vivo* and *in vitro* paradox.

In another work, we developed a lattice based model to study domain structures in two-component membranes under tension. The model is simply a 2D Ising model coupled to a discrete version of the Helfrich Hamiltonian for membranes in the linearized Monge representation in order to incorporate height deformations. Similar models have been studied numerous times within mean-field theory. However, computer simulations allow us to assess the influence of fluctuations, which are known to be important in phase transitions between disordered and modulated phases. The essential aspect of the model is the coupling of the local composition to the local membrane curvature, that corresponds to the two lipid components having different spontaneous curvatures. The main result of the simulations was that there is a region in the parameter space of the lipid-lipid interaction and the curvature-composition coupling, in which domains with a preferred finite-size appear, yet where the domains are not arranged in a structure with long-range order. This manifested microemulsion region is identified as the region where lipid rafts can form. Phase transitions between the disordered phase and the macroscopic phase separation have been studied in detail. The results numerically confirmed the theoretical hypothesis of [Schick \[2012\]](#), who related lipid rafts to a microemulsion-type structure in such systems as a result of membrane curvature. The interesting biological relevance is that those microemulsion-stabilized domains survive even at high temperature. Hence, it is not necessary for membranes to be tuned close to any phase transition. Another aspect of our result concerned the nature of the phase transition from the fluid phase to liquid-ordered/liquid-disordered phase coexistence. This transition is continuous and as is obvious belongs to the 2D Ising model universality class, in absence of a curvature-composition coupling. It actually remains the same for a weak coupling, yet becomes first-order as the coupling increases beyond a certain value. The importance of this result is its contradictions with the assumption that phase separation in membranes is

always continuous and of the 2D Ising universality.

In collaboration with experimental partners at Max Planck Institute for Biophysical Chemistry (Eggeling and Honigmann), we studied the effect of extracellular complements on the phase separation in lipid membranes. The lipid membrane is intricately in contact with its environment, via the cytoskeleton network in the plasma membranes or solid substrates in supported model membranes. To this end, a solid-supported membrane was cross-linked to an actin network via cross-linker molecules (pinning sites). In the theoretical part, we performed computer simulations of a lattice model describing the above. The model was developed to incorporate the interaction of the lipid membrane with its surrounding environment, as well as the lipid-lipid/pinning interaction, and a curvature-composition coupling.

Previous simulations of a flat membrane model (without height deformation) suggested that the actin network could be a key player in preventing macroscopic lipid phase separation, even at low temperature [Machta et al., 2011]. At the same time, these simulations predicted the presence of stable nanodomains along the actin fibers, even at high temperature. Using superresolution STED microscopy operating on the nanoscale and fluorescence correlation spectroscopy, simulation predictions have largely been confirmed experimentally. In addition to confirmation, experiments also revealed that previously used simulation models, namely the 2D Ising model, need to be refined in order to capture all observations. The essential ingredient of the improved model is a coupling between the local membrane composition and the local membrane curvature. To complement the experiments, we therefore presented a new body of simulation results, in which the latter coupling is explicitly included. Computer simulations that incorporate the local curvature were able to reproduce all experimentally observed domain structures. Our findings explained some of the apparent contradictions between pure lipid model membranes and intact cell membranes. In contrast to model membranes, the latter do not reveal a transition temperature below which the lipids macroscopically phase separate. We showed that this transition is effectively eliminated once an actin network is present. We also showed that the type of pinning sites, used to bind the actin network to the membrane, dramatically influences the properties of the nanodomains that become stabilized along the actin fibers. The explanation is that there exist an extra curvature-induced lipid-pinning interaction, which can compete with the energetic lipid-pinning interaction. This mechanism may be exploited by the cell to locally sort membrane constituents, as suggested by the lipid raft hypothesis.



---

As an extension to previous work, we furthermore demonstrated that the coupling between the membrane elastic properties and the extracellular matrix is already able to induce patterns on the membrane surface. For a solid-supported membrane bound to an actin network on top, regions of positive curvature are induced below the actin fibers (upper layer in a bilayer membrane). In addition, a similar effect has been observed in simulations of a membrane model where the proteins which connect the cytoskeleton to the membrane induce local non-zero curvature. The significance of these results is that the imprinted pattern occurs irrespective of any phase transition the lipids themselves may undergo. This complements existing views in which the occurrence of such transitions is considered to be crucial.

# Acknowledgments

I had a wonderful time during the course of my studies at the Institute of Theoretical Physics at the University of Göttingen. I would like to take this opportunity to thank all the people who accompanied and contributed to the success of this thesis.

Most importantly, I would like to thank my thesis advisor Richard Vink for his excellent supervision. I sincerely appreciate all his support, encouragement and great guidance throughout my PhD.

I am also grateful to Alf Honigmann and Christian Eggeling who contributed to the experimental part of the project, and similarly to Marcus Müller for his sincere help and thoughtful suggestions. I also thank Timo Fischer for his help and fruitful discussions. Moreover, I thank Annette Zippelius for her support and reviewing the dissertation.

Finally, I would like to express my deepest gratitude to all my friends and my family for their great company, and my special thanks to Dena without whom I would not have such an opportunity to make this.

# Bibliography

- Aizenman, M. and Wehr, J. (1989). Rounding of first-order phase transitions in systems with quenched disorder. *Physical Review Letters*, 62(21):2503–2506.
- Alberts, B., Johnson, A., Lewis, J., Raff, M., Roberts, K., and Walter, P. (2008). *Molecular Biology of the Cell*. Garland Science, 5 edition.
- Andelman, D., Kawakatsu, T., and Kawasaki, K. (1992). Equilibrium shape of two-component unilamellar membranes and vesicles. *EPL (Europhysics Letters)*, 19(1):57.
- Angelis, Jones, D. H., Grant, C. V., Park, S. H., Mesleh, M. F., and Opella, S. J. (2005). NMR Experiments on Aligned Samples of Membrane Proteins. In James, T. L., editor, *Nuclear Magnetic Resonance of Biological Macromolecules*, volume 394 of *Methods in Enzymology*, pages 350–382. Academic Press.
- Anisimov, M. A., Kostko, A. F., Sengers, J. V., and Yudin, I. K. (2005). Competition of mesoscales and crossover to theta-point tricriticality in near-critical polymer solutions. *The Journal of Chemical Physics*, 123(16):164901.
- Baumgart, T., Hammond, A. T., Sengupta, P., Hess, S. T., Holowka, D. A., Baird, B. A., and Webb, W. W. (2007). Large-scale fluid/fluid phase separation of proteins and lipids in giant plasma membrane vesicles. *PNAS, Proceedings of the National Academy of Sciences of the United States of America*, 104(9):3165–3170.
- Baumgart, T., Hess, S. T., and Webb, W. W. (2003). Imaging coexisting fluid domains in biomembrane models coupling curvature and line tension. *Nature*, 425(6960):821–824.
- Billoire, A., Lacaze, R., and Morel, A. (1992). A numerical study of finite-size scaling for first-order phase transitions. *Nuclear Physics B*, 370(3):773–796.

- Billoire, A., Neuhaus, T., and Berg, B. A. (1994). A determination of interface free energies. *Nuclear Physics B*, 413(3):795–812.
- Binder, K. (1981a). Critical properties from Monte Carlo coarse graining and renormalization. *Physical Review Letters*, 47(9):693–696.
- Binder, K. (1981b). Finite size scaling analysis of Ising model block distribution functions. *Zeitschrift für Physik B Condensed Matter*, 43(2):119–140.
- Binder, K. (1982). Monte Carlo calculation of the surface tension for two- and three-dimensional lattice-gas models. *Physical Review A*, 25(3):1699–1709.
- Binder, K. (1987). Theory of first-order phase transitions. *Reports on Progress in Physics*, 50(7):783–859.
- Binder, K. (1997). Applications of Monte Carlo methods to statistical physics. *Reports on Progress in Physics*, 60(5):487–559.
- Binder, K. and Heermann, D. W. (2010). *Monte Carlo Simulation in Statistical Physics: An Introduction*. Springer-Verlag, Berlin, Heidelberg, 5th edition.
- Binder, K. and Landau, D. P. (1984). Finite-size scaling at first-order phase transitions. *Physical Review B*, 30(3):1477–1485.
- Binder, W. H., Barragan, V., and Menger, F. M. (2003). Domains and rafts in lipid membranes. *Angewandte Chemie International Edition*, 42(47):5802–5827.
- Blöte, H. W. J., Guo, W., and Hilhorst, H. J. (2002). Phase transition in a two-dimensional Heisenberg model. *Physical Review Letters*, 88(4):047203.
- Borgs, C. and Kappler, S. (1992). Equal weight versus equal height: a numerical study of an asymmetric first-order transition. *Physics Letters A*, 171(1–2):37–42.
- Brewster, R., Pincus, P. A., and Safran, S. A. (2009). Hybrid lipids as a biological surface-active component. *Biophysical Journal*, 97(4):1087–1094.
- Bricmont, J. and Kupiainen, A. (1987). Lower critical dimension for the random-field Ising model. *Physical Review Letters*, 59(16):1829–1832.
- Brown, D. A. and London, E. (1998). Functions of lipid rafts in biological membranes. *Annual Review of Cell and Developmental Biology*, 14(1):111–136.

- Caillé, A., Pink, D., Verteuil, F. D., and Zuckermann, M. J. (1980). Theoretical models for quasi-two-dimensional mesomorphic monolayers and membrane bilayers. *Canadian Journal of Physics*, 58(5):581–611.
- Cardarelli, F., Lanzano, L., and Gratton, E. (2012). Capturing directed molecular motion in the nuclear pore complex of live cells. *PNAS, Proceedings of the National Academy of Sciences of the United States of America*, 109(25):9863–9868.
- Charrier, A. and Thibaudau, F. (2005). Main phase transitions in supported lipid single-bilayer. *Biophysical Journal*, 89(2):1094–1101.
- Connell, S. D., Heath, G., Olmsted, P. D., and Kisil, A. (2013). Critical point fluctuations in supported lipid membranes. *Faraday Discussions*, 161(0):91–111.
- Corvera, E., Laradji, M., and Zuckermann, M. J. (1993). Application of finite-size scaling to the Pink model for lipid bilayers. *Physical Review E*, 47(1):696–703.
- Danielli, J. F. and Davson, H. (1935). A contribution to the theory of permeability of thin films. *Journal of Cellular and Comparative Physiology*, 5(4):495–508.
- de Pablo, J. J. (2011). Coarse-grained simulations of macromolecules: From DNA to nanocomposites. *Annual Review of Physical Chemistry*, 62(1):555–574.
- Dietrich, C., Bagatolli, L. A., Volovyk, Z. N., Thompson, N. L., Levi, M., Jacobson, K., and Gratton, E. (2001). Lipid rafts reconstituted in model membranes. *Biophysical Journal*, 80(3):1417–1428.
- Digman, M. A., Brown, C. M., Sengupta, P., Wiseman, P. W., Horwitz, A. R., and Gratton, E. (2005). Measuring fast dynamics in solutions and cells with a laser scanning microscope. *Biophysical Journal*, 89(2):1317–1327.
- Digman, M. A. and Gratton, E. (2009). Imaging barriers to diffusion by pair correlation functions. *Biophysical Journal*, 97(2):665–673.
- Dimova, R., Aranda, S., Bezlyepkina, N., Nikolov, V., Riske, K. A., and Lipowsky, R. (2006). A practical guide to giant vesicles. probing the membrane nanoregime via optical microscopy. *Journal of Physics: Condensed Matter*, 18(28):S1151–S1176.
- Doniach, S. (1978). Thermodynamic fluctuations in phospholipid bilayers. *The Journal of Chemical Physics*, 68(11):4912–4916.
- Edidin, M. (2003). The state of lipid rafts: from model membranes to cells. *Annual Review of Biophysics and Biomolecular Structure*, 32(1):257–283.

- Eggeling, C., Ringemann, C., Medda, R., Schwarzmann, G., Sandhoff, K., Polyakova, S., Belov, V. N., Hein, B., von Middendorff, C., Schonle, A., and Hell, S. W. (2009). Direct observation of the nanoscale dynamics of membrane lipids in a living cell. *Nature*, 457(7233):1159–1162.
- Eggeling, C., Willig, K. I., and Barrantes, F. J. (2013). STED microscopy of living cells – new frontiers in membrane and neurobiology. *Journal of Neurochemistry*, 126(2):203–212.
- Ehrig, J., Petrov, E. P., and Schwille, P. (2011a). Near-critical fluctuations and cytoskeleton-assisted phase separation lead to subdiffusion in cell membranes. *Biophysical Journal*, 100(1):80–89.
- Ehrig, J., Petrov, E. P., and Schwille, P. (2011b). Phase separation and near-critical fluctuations in two-component lipid membranes: Monte Carlo simulations on experimentally relevant scales. *New Journal of Physics*, 13(4):045019.
- Engelman, D. M. (2005). Membranes are more mosaic than fluid. *Nature*, 438(7068):578–580.
- Farago, O. (2008). Membrane fluctuations near a plane rigid surface. *Physical Review E*, 78(5):051919.
- Farago, O. (2011). *Statistical Thermodynamics of Adhesion Points in Supported Membranes*, volume 14, pages 129–155. Elsevier.
- Ferrenberg, A. M. and Swendsen, R. H. (1988). New Monte Carlo technique for studying phase transitions. *Physical Review Letters*, 61(23):2635–2638.
- Ferrenberg, A. M. and Swendsen, R. H. (1989). Optimized Monte Carlo data analysis. *Physical Review Letters*, 63(12):1195–1198.
- Fischer, T., Risselada, H. J., and Vink, R. L. C. (2012). Membrane lateral structure: The influence of immobilized particles on domain size. *Physical Chemistry Chemical Physics*, 14(42):14500–14508.
- Fischer, T. and Vink, R. L. C. (2009). Restricted orientation "liquid crystal" in two dimensions: Isotropic-nematic transition or liquid-gas one(?). *EPL (Europhysics Letters)*, 85(5):56003.
- Fischer, T. and Vink, R. L. C. (2010). The Widom-Rowlinson mixture on a sphere: elimination of exponential slowing down at first-order phase transitions. *Journal of Physics: Condensed Matter*, 22(10):104123.

- Fischer, T. and Vink, R. L. C. (2011). Domain formation in membranes with quenched protein obstacles: Lateral heterogeneity and the connection to universality classes. *The Journal of Chemical Physics*, 134(5):055106.
- Fish, J. M. and Vink, R. L. C. (2009). Finite-size effects at first-order isotropic-to-nematic transitions. *Physical Review B*, 80(1):014107.
- Fisher, M. and Barber, M. (1972). Scaling theory for finite-size effects in the critical region. *Physical Review Letters*, 28(23):1516–1519.
- Frederix, P. L. T. M., Bosshart, P. D., and Engel, A. (2009). Atomic force microscopy of biological membranes. *Biophysical Journal*, 96(2):329–338.
- Goldenfeld, N. (1992). *Lectures On Phase Transitions And The Renormalization Group (Frontiers in Physics, 85)*. Westview Press, illustrated edition edition.
- Gómez, J., Sagués, F., and Reigada, R. (2010). Effect of integral proteins in the phase stability of a lipid bilayer: Application to raft formation in cell membranes. *The Journal of Chemical Physics*, 132(13):135104.
- Gómez-Llobregat, J., Buceta, J., and Reigada, R. (2013). Interplay of cytoskeletal activity and lipid phase stability in dynamic protein recruitment and clustering. *Scientific Reports*, 3:2608.
- Gompper, G. and Schick, M. (1990). Lattice model of microemulsions: The effect of fluctuations in one and two dimensions. *Physical Review A*, 42(4):2137.
- Goswami, D., Gowrishankar, K., Bilgrami, S., Ghosh, S., Raghupathy, R., Chadda, R., Vishwakarma, R., Rao, M., and Mayor, S. (2008). Nanoclusters of GPI-anchored proteins are formed by cortical actin-driven activity. *Cell*, 135(6):1085.
- Gov, N. and Safran, S. (2004). Pinning of fluid membranes by periodic harmonic potentials. *Physical Review E*, 69(1):011101.
- Gov, N. S. and Gopinathan, A. (2006). Dynamics of membranes driven by actin polymerization. *Biophysical Journal*, 90(2):454.
- Gozdz, W. T. and Gompper, G. (2001). Shape transformations of two-component membranes under weak tension. *EPL (Europhysics Letters)*, 55(4):587.
- Hammond, A. T., Heberle, F. A., Baumgart, T., Holowka, D., Baird, B., and Feigenson, G. W. (2005). Crosslinking a lipid raft component triggers liquid ordered-liquid disordered phase separation in model plasma membranes. *PNAS*,

- Proceedings of the National Academy of Sciences of the United States of America*, 102(18):6320–6325.
- Hancock, J. F. (2006). Lipid rafts: contentious only from simplistic standpoints. *Nature Reviews Molecular Cell Biology*, 7(6):456–462.
- Hansen, P., Miao, L., and Ipsen, J. (1998). Fluid lipid bilayers: Intermonolayer coupling and its thermodynamic manifestations. *Physical Review E*, 58(2):2311.
- Harden, J. L., MacKintosh, F. C., and Olmsted, P. D. (2005). Budding and domain shape transformations in mixed lipid films and bilayer membranes. *Physical Review E*, 72(1):011903.
- Heberle, F. A. and Feigenson, G. W. (2011). Phase separation in lipid membranes. *Cold Spring Harbor Perspectives in Biology*, 3(4):a004697.
- Heinemann, F., Vogel, S. K., and Schwille, P. (2013). Lateral membrane diffusion modulated by a minimal actin cortex. *Biophysical Journal*, 104(7):1465–1475.
- Helfrich, W. (1973). Elastic properties of lipid bilayers: Theory and possible experiments. *Zeitschrift für Naturforschung C*, 28(11):693–703.
- Hell, S. W. (2007). Far-field optical nanoscopy. *Science*, 316(5828):1153–1158.
- Hell, S. W. and Wichmann, J. (1994). Breaking the diffraction resolution limit by stimulated emission: stimulated-emission-depletion fluorescence microscopy. *Optics Letters*, 19(11):780–782.
- Helm, C., Knoll, W., and Israelachvili, J. (1991). Measurement of ligand-receptor interactions. *PNAS, Proceedings of the National Academy of Sciences of the United States of America*, 88(18):8169–8173.
- Hömberg, M. and Müller, M. (2010). Main phase transition in lipid bilayers: Phase coexistence and line tension in a soft, solvent-free, coarse-grained model. *The Journal of Chemical Physics*, 132(15):155104.
- Honerkamp-Smith, A., Veatch, S., and Keller, S. (2009). An introduction to critical points for biophysicists; observations of compositional heterogeneity in lipid membranes. *Biochimica et Biophysica Acta (BBA) - Biomembranes*, 1788(1):53–63.
- Honerkamp-Smith, A. R., Cicuta, P., Collins, M. D., Veatch, S. L., den Nijs, M., Schick, M., and Keller, S. L. (2008). Line tensions, correlation lengths, and critical



- exponents in lipid membranes near critical points. *Biophysical Journal*, 95(1):236–246.
- Honigmann, A., Mueller, V., Hell, S. W., and Eggeling, C. (2013). STED microscopy detects and quantifies liquid phase separation in lipid membranes using a new far-red emitting fluorescent phosphoglycerolipid analogue. *Faraday Discussions*, 161(0):77–89.
- Honigmann, A., Sadeghi, S., Keller, J., Hell, S. W., Eggeling, C., and Vink, R. L. C. (2014). A lipid bound actin meshwork organizes liquid phase separation in model membranes. *eLife*, 3:e01671.
- Honigmann, A., Walter, C., Erdmann, F., Eggeling, C., and Wagner, R. (2010). Characterization of horizontal lipid bilayers as a model system to study lipid phase separation. *Biophysical Journal*, 98(12):2886–2894.
- Hsieh, W.-T., Hsu, C.-J., Capraro, B. R., Wu, T., Chen, C.-M., Yang, S., and Baumgart, T. (2012). Curvature sorting of peripheral proteins on solid-supported wavy membranes. *Langmuir*, 28(35):12838–12843.
- Imbrie, J. Z. (1984). Lower critical dimension of the random-field Ising model. *Physical Review Letters*, 53(18):1747–1750.
- Imry, Y. and Ma, S.-K. (1975). Random-field instability of the ordered state of continuous symmetry. *Physical Review Letters*, 35(21):1399–1401.
- Ipsen, J. H., Jørgensen, K., and Mouritsen, O. G. (1990). Density fluctuations in saturated phospholipid bilayers increase as the acyl-chain length decreases. *Biophysical Journal*, 58(5):1099–1107.
- Ipsen, J. H., Karlstrom, G., Mouritsen, O., Wennerstrom, H., and Zuckermann, M. (1987). Phase equilibria in the phosphatidylcholine-cholesterol system. *Biochimica et Biophysica Acta (BBA) - Biomembranes*, 905(1):162–172.
- Jacobson, K., Mouritsen, O. G., and Anderson, R. G. W. (2007). Lipid rafts: at a crossroad between cell biology and physics. *Nature Cell Biology*, 9(1):7–14.
- Janmey, P. A. (1998). The cytoskeleton and cell signaling: Component localization and mechanical coupling. *Physiological Reviews*, 78(3):763–781.
- Janmey, P. A. and Lindberg, U. (2004). Cytoskeletal regulation: rich in lipids. *Nature Reviews Molecular Cell Biology*, 5(8):658–666.

- Jensen, M. H., Morris, E. J., and Simonsen, A. C. (2007). Domain shapes, coarsening, and random patterns in ternary membranes. *Langmuir*, 23(15):8135–8141.
- Kaizuka, Y. and Groves, J. T. (2010). Bending-mediated superstructural organizations in phase-separated lipid membranes. *New Journal of Physics*, 12(9):095001.
- Karatekin, E., Sandre, O., Guitouni, H., Borghi, N., Puech, P.-H., and Brochard-Wyart, F. (2003). Cascades of transient pores in giant vesicles: Line tension and transport. *Biophysical Journal*, 84(3):1734–1749.
- Keller, D., Larsen, N. B., Møller, I. M., and Mouritsen, O. G. (2005). Decoupled phase transitions and Grain-Boundary melting in supported phospholipid bilayers. *Physical Review Letters*, 94(2):025701.
- Kim, S. A., Heinze, K. G., and Schwille, P. (2007). Fluorescence correlation spectroscopy in living cells. *Nature Methods*, 4(11):963–973.
- Kolmakov, K., Belov, V., Bierwagen, J., Ringemann, C., Müller, V., Eggeling, C., and Hell, S. (2010). Red-emitting rhodamine dyes for fluorescence microscopy and nanoscopy. *Chemistry – A European Journal*, 16(1):158–166.
- Komura, S. and Andelman, D. (2014). Physical aspects of heterogeneities in multi-component lipid membranes. *Advances in Colloid and Interface Science*, 208(0):34–46.
- Kranenburg, M. and Smit, B. (2005). Phase behavior of model lipid bilayers. *The Journal of Physical Chemistry B*, 109(14):6553–6563.
- Kumar, P. B. S., Gompper, G., and Lipowsky, R. (1999). Modulated phases in multicomponent fluid membranes. *Physical Review E*, 60(4):4610–4618.
- Kusumi, A., Nakada, C., Ritchie, K., Murase, K., Suzuki, K., Murakoshi, H., Kasai, R. S., Kondo, J., and Fujiwara, T. (2005). Paradigm shift of the plasma membrane concept from the two-dimensional continuum fluid to the partitioned fluid: High-speed single-molecule tracking of membrane molecules. *Annual Review of Biophysics and Biomolecular Structure*, 34(1):351–378.
- Landau, D. P. and Binder, K. (2005). *A Guide to Monte Carlo Simulations in Statistical Physics*. Cambridge University Press.
- Lee, J. and Kosterlitz, J. M. (1991). Finite-size scaling and Monte Carlo simulations of first-order phase transitions. *Physical Review B*, 43(4):3265–3277.

- Leibler, S. and Andelman, D. (1987). Ordered and curved meso-structures in membranes and amphiphilic films. *Journal de Physique*, 48(11):2013–2018.
- Lenne, P.-F. and Nicolas, A. (2009). Physics puzzles on membrane domains posed by cell biology. *Soft Matter*, 5(15):2841–2848.
- Levental, I., Byfield, F. J., Chowdhury, P., Gai, F., Baumgart, T., and Janmey, P. A. (2009). Cholesterol-dependent phase separation in cell-derived giant plasma-membrane vesicles. *The Biochemical Journal*, 424(2):163–167.
- Lin, L. and Brown, F. (2005). Dynamic simulations of membranes with cytoskeletal interactions. *Physical Review E*, 72(1):011910.
- Lin, L. C. L. and Brown, F. L. H. (2004). Brownian dynamics in fourier space: Membrane simulations over long length and time scales. *Physical Review Letters*, 93(25):256001.
- Lingwood, D., Ries, J., Schwille, P., and Simons, K. (2008). Plasma membranes are poised for activation of raft phase coalescence at physiological temperature. *PNAS, Proceedings of the National Academy of Sciences of the United States of America*, 105(29):10005–10010.
- Lingwood, D. and Simons, K. (2010). Lipid rafts as a membrane-organizing principle. *Science*, 327(5961):46–50.
- Lipowsky, R. (1995). *Generic Interactions of Flexible Membranes*, chapter Ch. 11, page 521. Elsevier.
- Lipowsky, R. and Sackmann, E. (1995). *Structure and Dynamics of Membranes (Handbook of Biological Physics) (Vol 1)*. North Holland, 1 edition.
- Lipowsky, R. and Seifert, U. (1991). Adhesion of vesicles and membranes. *Molecular Crystals and Liquid Crystals*, 202(1):17–25.
- Lipowsky, R. and Zielinska, B. (1989). Binding and unbinding of lipid membranes: A Monte Carlo study. *Physical Review Letters*, 62(13):1572–1575.
- Liu, A. P. and Fletcher, D. A. (2006). Actin polymerization serves as a membrane domain switch in model lipid bilayers. *Biophysical Journal*, 91(11):4064–4070.
- Liu, J., Qi, S., Groves, J. T., and Chakraborty, A. K. (2005). Phase segregation on different length scales in a model cell membrane system. *The Journal of Physical Chemistry B*, 109(42):19960–19969.

- London, E. and Brown, D. A. (2000). Insolubility of lipids in triton X-100: physical origin and relationship to sphingolipid/cholesterol membrane domains (rafts). *Biochimica et Biophysica Acta (BBA) - Biomembranes*, 1508(1-2):182–195.
- Machta, B. B., Papanikolaou, S., Sethna, J. P., and Veatch, S. L. (2011). Minimal model of plasma membrane heterogeneity requires coupling cortical actin to criticality. *Biophysical Journal*, 100(7):1668–1677.
- MacKintosh, F. (1994). Mixed fluid bilayers: Effects of confinement. *Physical Review E*, 50(4):2891.
- Magde, D., Elson, E., and Webb, W. W. (1972). Thermodynamic fluctuations in a reacting system—Measurement by fluorescence correlation spectroscopy. *Physical Review Letters*, 29(11):705–708.
- Mangeat, P., Roy, C., and Martin, M. (1999). {ERM} proteins in cell adhesion and membrane dynamics. *Trends in Cell Biology*, 9(5):187–192.
- Marrink, S. J., Risselada, J., and Mark, A. E. (2005). Simulation of gel phase formation and melting in lipid bilayers using a coarse grained model. *Chemistry and Physics of Lipids*, 135(2):223–244.
- Marčelja, S. (1973). Molecular model for phase transition in biological membranes. *Nature*, 241(5390):451–453.
- Marčelja, S. (1974). Chain ordering in liquid crystals: Ii. structure of bilayer membranes. *Biochimica et Biophysica Acta (BBA) - Biomembranes*, 367(2):165–176.
- Mattila, P. K., Pykalainen, A., Saarikangas, J., Paavilainen, V. O., Vihinen, H., Jokitalo, E., and Lappalainen, P. (2007). Missing-in-metastasis and IRSp53 deform PI(4,5)P2-rich membranes by an inverse BAR domain-like mechanism. *The Journal of Cell Biology*, 176(7):953.
- Mayor, S. and Rao, M. (2004). Rafts: Scale-dependent, active lipid organization at the cell surface. *Traffic*, 5(4):231.
- McMahon, H. T. and Gallop, J. L. (2005). Membrane curvature and mechanisms of dynamic cell membrane remodelling. *Nature*, 438(7068):590–596.
- McMullen, T. P., Lewis, R., and McElhaney, R. N. (2004). Cholesterol–phospholipid interactions, the liquid-ordered phase and lipid rafts in model and biological membranes. *Current Opinion in Colloid & Interface Science*, 8(6):459–468.

- Meinhardt, S., Vink, R. L. C., and Schmid, F. (2013). Monolayer curvature stabilizes nanoscale raft domains in mixed lipid bilayers. *PNAS, Proceedings of the National Academy of Sciences of the United States of America*, 110(12):4476–4481.
- Michonova-Alexova, E. I. and Sugár, I. P. (2002). Component and state separation in DMPC/DSPC lipid bilayers: a monte carlo simulation study. *Biophysical Journal*, 83(4):1820–1833.
- Mitchell, M. (2009). *Complexity: A Guided Tour*. Oxford University Press, USA.
- Mouritsen, O. G. (1983). Studies on the lack of cooperativity in the melting of lipid bilayers. *Biochimica et Biophysica Acta (BBA) - Biomembranes*, 731(2):217–221.
- Mouritsen, O. G. (1984). *Computer Studies of Phase Transitions and Critical Phenomena*. Springer-Verlag, Berlin.
- Mouritsen, O. G. (1987). Physics of biological membranes. In Baeriswyl, D., Droz, M., Malaspina, A., and Martinoli, P., editors, *Physics in Living Matter*, volume 284 of *Lecture Notes in Physics*, chapter 8, pages 76–109. Springer, Berlin/Heidelberg.
- Mouritsen, O. G. (1991). Theoretical models of phospholipid phase transitions. *Chemistry and Physics of Lipids*, 57(2-3):179–194.
- Mouritsen, O. G. (2004). *Life - As a Matter of Fat*. Springer, 1 edition.
- Mouritsen, O. G. (2011). Lipidology and lipidomics—quo vadis? a new era for the physical chemistry of lipids. *Physical Chemistry Chemical Physics*, 13(43):19195–19205.
- Mouritsen, O. G., Boothroyd, A., Harris, R., Jan, N., Lookman, T., MacDonald, L., Pink, D. A., and Zuckermann, M. J. (1983). Computer simulation of the main gel–fluid phase transition of lipid bilayers. *The Journal of Chemical Physics*, 79(4):2027–2041.
- Müller, M. and Binder, K. (2001). Interface localization-delocalization transition in a symmetric polymer blend: A finite-size scaling Monte Carlo study. *Physical Review E*, 63(2):021602.
- Müller, M. and de Pablo, J. (2006). Simulation Techniques for Calculating Free Energies. In Ferrario, M., Ciccotti, G., and Binder, K., editors, *Computer Simulations in Condensed Matter Systems: From Materials to Chemical Biology Volume 1*, volume 703 of *Lecture Notes in Physics*, pages 67–126. Springer-Verlag, Berlin, Heidelberg.

- Müller, M., Katsov, K., and Schick, M. (2003). Coarse-grained models and collective phenomena in membranes: Computer simulation of membrane fusion. *Journal of Polymer Science Part B: Polymer Physics*, 41(13):1441–1450.
- Müller, M., Katsov, K., and Schick, M. (2006). Biological and synthetic membranes: What can be learned from a coarse-grained description? *Physics Reports*, 434(5-6):113–176.
- Munro, S. (2003). Lipid rafts: Elusive or illusive? *Cell*, 115(4):377–388.
- Murtola, T., Róg, T., Falck, E., Karttunen, M., and Vattulainen, I. (2006). Transient ordered domains in single-component phospholipid bilayers. *Physical Review Letters*, 97(23):238102.
- Nagle, J. F. (1980). Theory of the main lipid bilayer phase transition. *Annual Review of Physical Chemistry*, 31(1):157–196.
- Neuhaus, T. and Hager, J. S. (2003). 2D crystal shapes, droplet condensation, and exponential slowing down in simulations of first-order phase transitions. *Journal of Statistical Physics*, 113(1):47–83.
- Newman, M. E. J. and Barkema, G. T. (1999). *Monte Carlo Methods in Statistical Physics*. Clarendon Press.
- Nichols, B. (2005). Cell biology without a raft. *Nature*, 436(7051):638–639.
- Orkoulas, G., Fisher, M. E., and Panagiotopoulos, A. Z. (2001). Precise simulation of criticality in asymmetric fluids. *Physical Review E*, 63(5):051507.
- Orkoulas, G., Panagiotopoulos, A. Z., and Fisher, M. E. (2000). Criticality and crossover in accessible regimes. *Physical Review E*, 61(5):5930–5939.
- Orsi, M., Michel, J., and Essex, J. W. (2010). Coarse-grain modelling of DMPC and DOPC lipid bilayers. *Journal of Physics: Condensed Matter*, 22(15):155106.
- Palmieri, B. and Safran, S. A. (2013). Hybrid lipids increase the probability of fluctuating nanodomains in mixed membranes. *Langmuir*, 29(17):5246–5261.
- Parthasarathy, R. and Groves, J. T. (2007). Curvature and spatial organization in biological membranes. *Soft Matter*, 3(1):24–33.
- Parthasarathy, R., Yu, C.-h., and Groves, J. T. (2006). Curvature-modulated phase separation in lipid bilayer membranes. *Langmuir*, 22(11):5095–5099.

- Phillips, R., Kondev, J., Theriot, J., and Garcia, H. (2012). *Physical Biology of the Cell*. Garland Science, 2 edition.
- Pike, L. J. (2009). The challenge of lipid rafts. *Journal of Lipid Research*, 50(Supplement):S323–S328.
- Pink, D. A., Georgallas, A., and Zuckermann, M. J. (1980a). Phase transitions and critical indices of a phospholipid bilayer model. *Zeitschrift für Physik B Condensed Matter*, 40(1):103–110.
- Pink, D. A., Green, T. J., and Chapman, D. (1980b). Raman scattering in bilayers of saturated phosphatidylcholines. experiment and theory. *Biochemistry*, 19(2):349–356.
- Rädler, J. O., Feder, T. J., Strey, H. H., and Sackmann, E. (1995). Fluctuation analysis of tension-controlled undulation forces between giant vesicles and solid substrates. *Physical Review E*, 51(5):4526–4536.
- Reister, E., Bihl, T., Seifert, U., and Smith, A.-S. (2011). Two intertwined facets of adherent membranes: membrane roughness and correlations between ligand–receptors bonds. *New Journal of Physics*, 13(2):025003.
- Ries, J. and Schwille, P. (2006). Studying slow membrane dynamics with continuous wave scanning fluorescence correlation spectroscopy. *Biophysical Journal*, 91(5):1915–1924.
- Risbo, J., Sperotto, M. M., and Mouritsen, O. G. (1995). Theory of phase equilibria and critical mixing points in binary lipid bilayers. *The Journal of Chemical Physics*, 103(9):3643–3656.
- Ritchie, K., Iino, R., Fujiwara, T., Murase, K., and Kusumi, A. (2003). The fence and picket structure of the plasma membrane of live cells as revealed by single molecule techniques (review). *Molecular Membrane Biology*, 20(1):13–18.
- Saarikangas, J., Zhao, H., and Lappalainen, P. (2010). Regulation of the actin cytoskeleton-plasma membrane interplay by phosphoinositides. *Physiological Reviews*, 90(1):259–289.
- Sackmann, E. (1996). Supported membranes: Scientific and practical applications. *Science*, 271(5245):43–48.
- Sadeghi, S., Müller, M., and Vink, R. L. C. (2014). Raft formation in lipid bilayers coupled to curvature. *Biophysical Journal*, 107(7):5864.

- Sadeghi, S. and Vink, R. L. C. (2012). Main transition in the pink membrane model: Finite-size scaling and the influence of surface roughness. *Physical Review E*, 85(6):061912.
- Sadeghi, S. and Vink, R. L. C. (2014). Membrane sorting via the extracellular matrix. *Biochimica et Biophysica Acta (BBA) - Biomembranes*, 1848(2):527–531.
- Salditt, T. (2005). Thermal fluctuations and stability of solid-supported lipid membranes. *Journal of Physics: Condensed Matter*, 17(6):R287.
- Saunders, M. G. and Voth, G. A. (2013). Coarse-graining methods for computational biology. *Annual Review of Biophysics*, 42(1):73–93.
- Schick, M. (2012). Membrane heterogeneity: Manifestation of a curvature-induced microemulsion. *Physical Review E*, 85(3):031902.
- Scita, G., Confalonieri, S., Lappalainen, P., and Suetsugu, S. (2008). IRSp53: crossing the road of membrane and actin dynamics in the formation of membrane protrusions. *Trends in Cell Biology*, 18(2):52.
- Scoville-Simonds, M. and Schick, M. (2003). Theory of the effect of unsaturation on the main-chain transition. *Physical Review E*, 67(1):011911.
- Seeger, H. M., Cerbo, A. D., Alessandrini, A., and Facci, P. (2010). Supported lipid bilayers on Mica and Silicon Oxide: Comparison of the main phase transition behavior. *The Journal of Physical Chemistry B*, 114(27):8926–8933.
- Seifert, U. (1997). Configurations of fluid membranes and vesicles. *Advances in Physics*, 46(1):13–137.
- Semrau, S. and Schmidt, T. (2009). Membrane heterogeneity – from lipid domains to curvature effects. *Soft Matter*, 5(17):3174–3186.
- Sezgin, E., Kaiser, H.-J., Baumgart, T., Schwille, P., Simons, K., and Levental, I. (2012). Elucidating membrane structure and protein behavior using giant plasma membrane vesicles. *Nature Protocols*, 7(6):1042–1051.
- Shlomovitz, R., Maibaum, L., and Schick, M. (2014). Macroscopic phase separation, modulated phases, and microemulsions: A unified picture of rafts. *Biophysical Journal*, 106(9):1979.
- Shlomovitz, R. and Schick, M. (2013). Model of a raft in both leaves of an asymmetric lipid bilayer. *Biophysical Journal*, 105(6):1406–1413.



- Simons, K. and Ehehalt, R. (2002). Cholesterol, lipid rafts, and disease. *The Journal of Clinical Investigation*, 110(5):597–603.
- Simons, K. and Ikonen, E. (1997). Functional rafts in cell membranes. *Nature*, 387(6633):569–572.
- Simons, K. and Sampaio, J. L. (2011). Membrane organization and lipid rafts. *Cold Spring Harbor Perspectives in Biology*, 3(10):a004697.
- Simons, K. and Toomre, D. (2000). Lipid rafts and signal transduction. *Nature Reviews Molecular Cell Biology*, 1(1):31–39.
- Simons, K. and van Meer, G. (1988). Lipid sorting in epithelial cells. *Biochemistry*, 27(17):6197–6202.
- Simons, K. and Vaz, W. L. (2004). Model systems, lipid rafts, and cell membranes. *Annual Review of Biophysics and Biomolecular Structure*, 33(1):269–295.
- Singer, S. J. and Nicolson, G. L. (1972). The fluid mosaic model of the structure of cell membranes. *Science*, 175(4023):720–731.
- Sorre, B., Callan-Jones, A., Manzi, J., Goud, B., Prost, J., Bassereau, P., and Roux, A. (2012). Nature of curvature coupling of amphiphysin with membranes depends on its bound density. *PNAS, Proceedings of the National Academy of Sciences of the United States of America*, 109(1):173–178.
- Speck, T., Reister, E., and Seifert, U. (2010). Specific adhesion of membranes: Mapping to an effective bond lattice gas. *Physical Review E*, 82(2):021923.
- Speck, T. and Vink, R. L. C. (2012). Random pinning limits the size of membrane adhesion domains. *Physical Review E*, 86(3):031923.
- Spira, F., Mueller, N. S., Beck, G., von Olshausen, P., Beig, J., and Wedlich-Söldner, R. (2012). Patchwork organization of the yeast plasma membrane into numerous coexisting domains. *Nature Cell Biology*, 14(6):640.
- Stanley, H. E. (1987). *Introduction to Phase Transitions and Critical Phenomena*. Oxford University Press, USA.
- Subramaniam, A. B., Guidotti, G., Manoharan, V. N., and Stone, H. A. (2013). Glycans pattern the phase behaviour of lipid membranes. *Nature Materials*, 12(2):128–133.

- Surovtsev, N. V. and Dzuba, S. A. (2009). Conformational changes of lipids in bilayers at the dynamical transition near 200 K seen by raman scattering. *The Journal of Physical Chemistry B*, 113(47):15558–15562.
- Tokumasu, F., Jin, A. J., Feigenson, G. W., and Dvorak, J. A. (2003). Atomic force microscopy of nanometric liposome adsorption and nanoscopic membrane domain formation. *Ultramicroscopy*, 97(1-4):217–227.
- Toner, J. and Nelson, D. (1981). Smectic, cholesteric, and Rayleigh-Benard order in two dimensions. *Physical Review B*, 23(1):316.
- Toulmay, A. and Prinz, W. A. (2013). Direct imaging reveals stable, micrometer-scale lipid domains that segregate proteins in live cells. *The Journal of Cell Biology*, 202(1):35.
- Tröster, A. (2007). Coarse grained free energies with gradient corrections from Monte Carlo simulations in Fourier space. *Physical Review B*, 76(1):012402.
- van Enter, A. C. D. and Shlosman, S. B. (2002). First-order transitions for n-Vector models in two and more dimensions: Rigorous proof. *Physical Review Letters*, 89(28):285702.
- van Meer, G. and Simons, K. (1988). Lipid polarity and sorting in epithelial cells. *Journal of Cellular Biochemistry*, 36(1):51–58.
- Veatch, S. and Keller, S. (2005). Seeing spots: Complex phase behavior in simple membranes. *Biochimica et Biophysica Acta (BBA) - Molecular Cell Research*, 1746(3):172–185.
- Veatch, S., Polozov, I., Gawrisch, K., and Keller, S. (2004). Liquid domains in vesicles investigated by NMR and fluorescence microscopy. *Biophysical Journal*, 86(5):2910–2922.
- Veatch, S. L., Cicuta, P., Sengupta, P., Honerkamp-Smith, A., Holowka, D., and Baird, B. (2008). Critical fluctuations in plasma membrane vesicles. *ACS Chemical Biology*, 3(5):287–293.
- Veatch, S. L. and Keller, S. L. (2002). Organization in lipid membranes containing cholesterol. *Physical Review Letters*, 89(26):268101.
- Veatch, S. L. and Keller, S. L. (2003). Separation of liquid phases in giant vesicles of ternary mixtures of phospholipids and cholesterol. *Biophysical Journal*, 85(5):3074–3083.

- Veatch, S. L., Soubias, O., Keller, S. L., and Gawrisch, K. (2007). Critical fluctuations in domain-forming lipid mixtures. *PNAS, Proceedings of the National Academy of Sciences of the United States of America*, 104(45):17650–17655.
- Veksler, A. and Gov, N. S. (2007). Phase transitions of the coupled membrane-cytoskeleton modify cellular shape. *Biophysical Journal*, 93(11):3798.
- Vink, R. L. C. (2014). A finite-temperature Monte Carlo algorithm for network forming materials. *The Journal of Chemical Physics*, 140(10):104509.
- Vink, R. L. C. and Speck, T. (2013). Application of classical nucleation theory to the formation of adhesion domains. *Soft Matter*, 9(47):11197–11203.
- Virnau, P. and Müller, M. (2004). Calculation of free energy through successive umbrella sampling. *The Journal of Chemical Physics*, 120(23):10925–10930.
- Vogel, S. K., Petrasek, Z., Heinemann, F., and Schwille, P. (2013). Myosin motors fragment and compact membrane-bound actin filaments. *eLife*, 2:e00116.
- Vollmayr, K., Reger, J. D., Scheucher, M., and Binder, K. (1993). Finite size effects at thermally-driven first order phase transitions: A phenomenological theory of the order parameter distribution. *Zeitschrift für Physik B Condensed Matter*, 91(1):113–125.
- Wang, F. and Landau, D. P. (2001). Efficient, multiple-range random walk algorithm to calculate the density of states. *Physical Review Letters*, 86(10):2050–2053.
- Wang, T.-Y. and Silviu, J. R. (2001). Cholesterol does not induce segregation of liquid-ordered domains in bilayers modeling the inner leaflet of the plasma membrane. *Biophysical Journal*, 81(5):2762–2773.
- Weikl, T. R., Andelman, D., Komura, S., and Lipowsky, R. (2002). Adhesion of membranes with competing specific and generic interactions. *The European Physical Journal E: Soft Matter and Biological Physics*, 8(1):59–66.
- Wilding, N. B. and Nielaba, P. (1996). Tricritical universality in a two-dimensional spin fluid. *Physical Review E*, 53(1):926–934.
- Xie, A. F., Yamada, R., Gewirth, A. A., and Granick, S. (2002). Materials science of the gel to fluid phase transition in a supported phospholipid bilayer. *Physical Review Letters*, 89(24):246103.

- Yamamoto, T. and Safran, S. A. (2011). Line tension between domains in multicomponent membranes is sensitive to degree of unsaturation of hybrid lipids. *Soft Matter*, 7(15):7021–7033.
- Yang, J. and Appleyard, J. (2000). The main phase transition of Mica-supported phosphatidylcholine membranes. *The Journal of Physical Chemistry B*, 104(34):8097–8100.
- Yethiraj, A. and Weisshaar, J. C. (2007). Why are lipid rafts not observed in vivo? *Biophysical Journal*, 93(9):3113–3119.
- Yoon, T.-Y., Jeong, C., Lee, S.-W., Kim, J. H., Choi, M. C., Kim, S.-J., Kim, M. W., and Lee, S.-D. (2006). Topographic control of lipid-raft reconstitution in model membranes. *Nature Materials*, 5(4):281–285.
- Zimmerberg, J. and Kozlov, M. M. (2005). How proteins produce cellular membrane curvature. *Nature Reviews Molecular Cell Biology*, 7(1):9–19.

# Curriculum Vitae

## Personal information

Name: Sina Sadeghi  
Address: Friedrich-Hund-Platz 1, 37077 Göttingen  
Date of birth: 21 June 1978 (Ahwaz, Iran)  
Nationality: Iranian

## Education

2011–2014 (expected) PhD in Physics, Georg-August-Universität Göttingen, Göttingen, Germany.  
2008–2010 MSc in Complex Adaptive Systems, Chalmers University of Technology, Gothenburg, Sweden.  
2000–2002 MSc in Physics, Iran University of Science and Technology, Tehran, Iran.  
1996–2000 BSc in Physics, Shahid Beheshti University, Tehran, Iran.

## Publications

1. Sina Sadeghi and Richard Vink, Membrane sorting via the extracellular matrix, *Biochimica et Biophysica Acta (BBA) - Biomembranes*, 1848(2):527 (2014).
2. Sina Sadeghi, Marcus Müller, and Richard Vink, Raft formation in lipid bilayers coupled to curvature, *Biophysical Journal*, 107(7):1591 (2014).
3. Alf Honigsmann, Sina Sadeghi, Jan Keller, Stefan W. Hell, Christian Eggeling, and Richard Vink, A lipid bound actin meshwork organizes liquid phase separation in model membranes, *eLife* 3:e01671 (2014).
4. Sina Sadeghi and Richard Vink, The main transition in the Pink membrane model: finite-size scaling and the influence of surface roughness, *Physical Review E* 85(6):061912 (2012).